

THESIS FOR THE DEGREE OF DOCTOR OF PHILOSOPHY

Nanomechanical Phenomena in Low-Dimensional Structures

ANTON VIKSTRÖM



CHALMERS

Department of Physics
CHALMERS UNIVERSITY OF TECHNOLOGY
Göteborg, Sweden 2017

Nanomechanical Phenomena in Low-Dimensional Structures
ANTON VIKSTRÖM
ISBN 978-91-7597-581-8

© Anton Vikström, 2017

Doktorsavhandlingar vid Chalmers tekniska högskola
Ny serie nr 4262
ISSN 0346-718X

Department of Physics
Chalmers University of Technology
SE-412 96 Göteborg
Sweden
Telephone +46-(0)31-772100

Typeset in L^AT_EX.
Figures created using MATLAB, MATHEMATICA and INKSCAPE.

Printed by Chalmers reproservice
Göteborg, Sweden 2017

Nanomechanical Phenomena in Low-Dimensional Structures

ANTON VIKSTRÖM

Department of Physics

Chalmers University of Technology

ABSTRACT

This is a compilation thesis which investigates various mechanical phenomena in different low-dimensional nanoscale systems.

In the first part, we consider a purely mechanical phenomenon: the sensitivity of the dispersion of a Love-type surface acoustic wave (SAW) to geometry and material parameters. We model a SAW sensor as a three-layer system with elastic, viscous, or viscoelastic layers. We find that viscoelasticity can remove the support for Love waves. We also derive analytic expressions for the wave velocity and attenuation in the limit of a thin middle layer.

In the second part, we consider the interaction of SAWs with an electronic subsystem. We model a flat semi-infinite graphene sheet using 2D elasticity theory and consider Rayleigh-type SAWs. We investigate the resonant interaction of such SAWs with electronic edge states induced by a transverse magnetic field. When electronic relaxation is much faster than phonon absorption, we find that the SAWs attenuate. In the opposite limit, we show that nonlinear effects can lead to the formation of hypersonic solitons.

In the third part, we demonstrate how interaction with an electronic subsystem can actuate nanomechanical vibrations. We study two different systems composed of a movable quantum dot (QD) in position dependent tunneling contact with two leads. In the first system, the leads are held at different temperatures and a spin-valve effect prevents electron exchange between them. We show that electron-electron interaction can mediate a heat flow which can actuate the QD position via a capacitive coupling. In the second system, both the leads and the QD are superconducting and the system has mirror symmetry. We find that an applied ac field can induce charge oscillations in the QD and parametrically excite vibrations of its position. The automatic synchronization of the oscillations in charge and position generates a supercurrent, the direction of which is a result of spontaneous symmetry breaking.

KEYWORDS: surface acoustic waves, acoustic sensors, viscoelasticity, electronic edge states, solitons, NEMS, heat flow, superconductivity.

LIST OF PUBLICATIONS

This thesis consists of an introductory text and the scientific papers listed below. My contributions are listed in *italics*.

I Soft-film dynamics of SH-SAW sensors in viscous and viscoelastic fluids

A. Vikström and M. V. Voinova

Sensing and Bio-Sensing Research, **11**, 78 (2016)

I did the numerical calculations, checked the analytical calculations, and wrote the paper.

II Propagation of acoustic edge waves in graphene under quantum Hall effect

A. Vikström

Low Temperature Physics **41**, 381 (2015)

I did all of the calculations and wrote the paper.

III Hypersonic edge solitons in graphene under quantum Hall effect

A. Vikström and L. Gorelik

Europhysics Letters, **112**, 44004 (2015)

I did all of the calculations and was the main author.

IV Nanoelectromechanical Heat Engine Based on Electron-Electron Interaction

A. Vikström, A. M. Eriksson, S. I. Kulinich, and L. Y. Gorelik

Physical Review Letters, **117**, 247701 (2016)

I did most of the calculations and was the main author.

V Zero-Phase-Difference Josephson Current Based on Spontaneous Symmetry Breaking via Parametric Excitation of a Movable Superconducting Dot

A. M. Eriksson and A. Vikström

Accepted for publication in Physical Review Letters

I contributed to the calculations and co-authored the paper.

Other publications which are not included in this thesis:

- (VI) **Theory of QCM and SAW devices in sensors and biosensors applications**
M. Voinova and A. Vikström
Proceedings, Fourth Scientific Meeting EuNetAir (June 2015)
- (VII) **Theoretical Modeling of QCM-D Sensors in Environmental Applications**
M. Voinova and A. Vikström
Proceedings, Sixth Scientific Meeting EuNetAir (October 2016)
- (VIII) **The dynamics of viscoelastic layered systems studied by surface acoustic wave (SAW) sensors operated in a liquid phase**
A. Vikström
Extended abstract, World Congress on Biosensors 2016
Accepted for publication in Procedia Technology

Contents

1	Introduction	1
1.1	Outline of the Thesis	2
1.2	Reading Guide	3
2	Surface Wave Propagation in Viscoelastic Structures	5
2.1	Background: Acoustic Sensors	5
2.2	Acoustic Waves in Solids	7
2.3	Love Waves	9
2.4	SAW Sensors in Viscous Liquids	13
2.5	Viscoelastic Materials	18
2.6	Summary of Paper I	20
2.6.1	Results: Thin-film Expressions	20
2.6.2	Results: Vanishing Love-wave Support	21
2.6.3	Discussion & Outlook	21
3	Edge Electroacoustics	23
3.1	Background: Graphene	23
3.2	A System Overview	25
3.3	The Mechanical Subsystem	27
3.3.1	Rayleigh Waves	27
3.3.2	A Quantized Acoustic Hamiltonian	30
3.3.3	Eigenwaves & Phonons	31
3.4	The Electronic Subsystem	32
3.4.1	The Graphene Low-Energy Hamiltonian	32
3.4.2	The Zigzag Edge	38
3.4.3	Magnetically Induced Edge States	39
3.5	Electron-Strain Interaction	43
3.6	Summary of Papers II & III	45

3.6.1	Results: Rayleigh Wave Attenuation	47
3.6.2	Results: Electroacoustic Solitons	50
3.6.3	Discussion & Outlook	54
4	Nanoelectromechanical Actuation	57
4.1	Background: NEMS	57
4.2	Example: Resonant Actuation	59
4.2.1	Capacitive Coupling	60
4.2.2	Direct Resonance	61
4.2.3	Parametric Resonance	61
4.3	Example: The Shuttle Instability	63
4.3.1	A Quantum Dot	64
4.3.2	Tunneling Coupling	65
4.3.3	Electron Reservoirs	66
4.3.4	Electronic Rate Equation	67
4.3.5	Static QD & Tunneling Current	67
4.3.6	Actuation & Shuttle Current	68
4.4	Summary of Paper IV	69
4.4.1	Results: Actuation by a Heat Flow	72
4.4.2	Discussion & Outlook	76
4.5	Background: Superconductivity	76
4.6	The Josephson Effect	79
4.7	The Cooper-Pair Box	81
4.8	Summary of Paper V	82
4.8.1	Results: Actuation & Supercurrent	83
4.8.2	Results: Noise-Induced Supercurrent Reversal	85
4.8.3	Discussion & Outlook	85
5	Concluding Words	87

Chapter 1

Introduction

As you read this sentence, vibrations in the electromagnetic field reach your retinae, carrying the encoded information that is this sentence itself. Now, if you read this sentence *out loud*, vibrations of another type are created: *mechanical vibrations*. Your vocal cords vibrate, hitting air particles¹ which in turn hit other air particles and so on. This way, you produce mechanical waves with frequencies in the range of 85 to 255 Hz. The vibrations exit your mouth, bounce around for a bit and eventually reach your eardrums, making them vibrate; your brain registers this as “sound”. If the vibrations have a comparatively low frequency, you register your voice as “deep”. However, what you perceive is different from what others do. The reason? *The voice in your head*. Actually, when you speak, your vocal cords also create mechanical waves inside your head—you make the bones, cartilage, etc. vibrate—these waves propagate from your throat to your eardrums, and because of the structure and composition of your head, the low-frequency components of these waves dominate. Therefore, when you hear your own speech, you perceive it as deeper than others do, since they only detect the mechanical waves in the air, and (presumably) not the bass voice in your head. In all likelihood, you probably overestimate how deep your voice is, and if you experience discomfort while listening to recordings of yourself talking, this is probably why.

Waves of mechanical motion—semi-arbitrarily called “*sound waves*”—are all around us. Sometimes they are desirable, e.g., a soothing melody or an exhilarating rock song; other times they are simply noise, e.g., construc-

¹The author highly recommends reading this thesis in an air-filled environment. It has not been test read in other fluids but, if you manage, the gist of the paragraph still applies.

tion work or hip hop. The destructive waves of an earthquake are usually not considered “sound waves” since humans, rather than just hearing them, tend to perceive them by (mildly speaking) different means. Nevertheless, they are mechanical waves. Ultrasound is (by definition) inaudible to humans, but for many of our pets, scientists, and engineers, it is just “sound”. The physics is roughly the same. Therefore, sensors of the type we will consider in chapter 2 are said to be using “sound waves”, even though no one can actually hear them.

Mechanical vibrations are a common theme of this thesis. As the title suggests, we will not be considering earthquakes or boomboxes, but *nano*-mechanics—vibrations in very small systems. However, the theoretical treatment is often pretty much the same as on the macroscale. When we reach chapter 3, I will introduce electron-sound interaction; this then carries over to chapter 4, where we look at quantum mechanical phenomena such as tunneling and superpositions, with dynamics resolved on the single-electron level. This kind of mixing of quantum mechanical few-particle phenomena with larger (but usually microscopic) objects which can be treated with “macroscopic techniques” (often named after Victorian-era Englishmen) places the major part of this thesis in the field of *mesoscopic physics*. “Meso” means “intermediate” and refers to the regime between the macroscale, where classical physics apply, and the nanoscale, where we need quantum mechanics. In mesoscopic physics, as you will see, we often use a little bit of both.

1.1 Outline of the Thesis

In chapter 2, I introduce a mathematical description of sound waves and then use it to derive a simple model for a category of acoustic sensors, i.e., the topic of paper I. Acoustic sensors are widely used in, e.g., industry, air quality monitoring, and biological research. The interplay of soft materials and liquids drastically affects sound waves and therefore sensor readout. The reliability of sensors therefore requires detailed knowledge of this interplay; this issue is what we address in paper I.

Chapter 3 introduces the underlying theory of papers II and III, in which we consider the interaction between sound waves and electrons on the edge of a graphene sheet. Graphene is a unique material that was discovered in 2004 and may—in the not too distant future—have a big role to play in technological applications. Papers II and III consider two (almost comple-

mentary) limiting cases of electron-sound interaction and make predictions for how electrons affect sound-wave propagation along a graphene edge.

Chapter 4 introduces the wider field of “nanoelectromechanical systems” and the concept of mechanical actuation, i.e., the topic of papers IV and V. Paper IV proposes a means of converting a heat flow to vibrations, while paper V demonstrates how a supercurrent—a current flowing without resistance—can be driven nanoelectromechanically. I give a short introduction to superconductivity because of its relevance to paper V.

1.2 Reading Guide

Sections called “Background: ...” are there to introduce a field, often from a more historical or general perspective. Sections called “Summary of Paper(s) ...” aim to give the reader a physical understanding of the phenomena studied in the appended papers without getting bogged down in calculations². The other sections are theoretically oriented introductions to concepts and techniques which are vital to an understanding of the papers, e.g., an introduction to elasticity theory, an analogous calculation in a simpler system, a derivation of an employed model, or an example system with similar components. These sections are mainly directed to researchers in other fields or to junior researchers who are just starting out. A reader who is already familiar with the relevant field should be able to skip directly to the sections called “Summary of Paper(s) ...”.

²Readers wishing to get bogged down in calculations are referred to the papers and their supplemental material.

Chapter 2

Surface Wave Propagation in Viscoelastic Structures

This chapter is an introduction to paper I, which is on the topic of acoustic sensors and viscoelastic materials. I will begin by giving a brief background to the rich field of acoustic sensors. I then present a simple model of an acoustic sensor to establish the basics, to which I gradually introduce the required components and methodology of paper I. Finally, I conclude by summarizing and discussing the results of paper I.

2.1 Background: Acoustic Sensors

An acoustic sensor is a sensor that uses acoustic (sound) waves to probe its environment [1]. The quintessential example is the *quartz crystal microbalance*¹ (QCM) [2]. A flat disc of quartz is made to vibrate at resonance through the inverse piezoelectric effect (fig. 2.1a). The disc is cut along a particular crystal plane such that the generated vibrations are parallel to the disc surface; they are *pure shear* [1]. As was first demonstrated by Günter Sauerbrey in 1959 [3], the adsorption of particles onto the disc surface leads to a resonance-frequency shift which is proportional to the surface mass density of the adsorbate. By tracking the resonance-frequency shift, it is possible to measure the amount of adsorbed mass to great precision: less than 1 ng/cm^2 [4]. QCMs are therefore widely used for precise weighing [5] and for monitoring the growth rate of thin-film deposits [6]. However, by

¹Sometimes referred to as a thickness-shear mode resonator (TSM) [1].

2.1. BACKGROUND: ACOUSTIC SENSORS

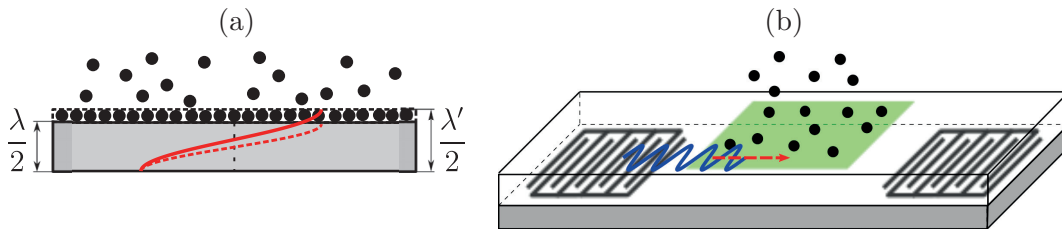


Figure 2.1: (a) A quartz crystal microbalance (QCM). A standing wave (red) is generated piezoelectrically in the quartz disc. Adsorbates (black circles) change the effective thickness of the disc and thus the resonant wavelength λ to λ' , equivalent to changing the resonance frequency. (b) A surface-acoustic-wave (SAW) sensor. An input IDT (left) generates a SAW (blue) which propagates (red arrow) across a sensing surface (green) and is finally registered by an output IDT (right). Adsorbates (black circles) on the sensing surface can be detected since they modify the propagation of the wave. (Note: pictures not to scale.)

relating the amount of particles adsorbed onto the surface to the concentration of particles in the surrounding environment, a QCM can also be used as a gas sensor [2, 7]. In addition, by chemically modifying the QCM surface so that target molecules attach to it, the QCM can be used for the detection of specific substances [8, 9] and chemical affinity measurements [10]. In 1985, Kanazawa and Gordon [11] found that submerging a QCM in a liquid introduces an additional resonance-frequency shift which depends on the properties of the liquid. Naturally, this implies that a QCM can be used to characterize liquids [12]. The frequency shift of a QCM covered by an adsorbed layer *and* submerged in a liquid contains contributions from both the adsorbates and the liquid. However, the contributions can be distinguished since the liquid also introduces dissipation. The dissipation can be measured using, e.g., ring-down: switch off the source of vibrations and measure their rate of attenuation [2, 4].

The QCM is the most well-known example of an acoustic sensor, and arguably the most conceptually simple. However, a different but related class of sensors are those that use *surface acoustic waves* (SAWs)—SAW sensors [1, 13, 14]. SAWs are a category of acoustic waves which are localized to a surface along which they propagate. In the case of SAW sensors, the SAWs are localized to the very surface onto which particles are adsorbed—the sensing surface. The SAWs respond to the adsorbed surface mass similarly to the shear vibrations in a QCM—with a phase-velocity shift (analogous to the frequency shift in QCM) and, in the case of a liquid environment, with wave attenuation [14, 15]. Therefore, the applications of SAW sensors largely overlap with those of the QCM. SAWs are usually both generated and

read out using *interdigital transducers* (IDTs) [1, 13, 16], comb-like metallic electrodes with multiple, equally spaced “fingers”² which are attached to a piezoelectric substrate. By applying an ac voltage to an input IDT, a SAW is created in the piezoelectric substrate. The distance between the IDT fingers determines the wavelength of the generated SAW [17–19], and, e.g., the cut of the substrate crystal determines which type of SAW is generated [19]. In this chapter, we will exclusively be discussing a type of *shear-horizontally polarized* (SH-) SAWs. SH-SAWs consists entirely of vibrations which are in the surface plane and are also perpendicular to the direction of propagation [19], i.e., they are pure shear, just as the bulk oscillations of a QCM. The generated SAW leaves the input IDT, propagates across the sensing surface, and then reaches an output IDT which registers the signal through the piezoelectric effect (fig. 2.1b) [1]. Since an electric signal is converted to a much slower acoustic signal and then back again, resulting in a signal delay, such a configuration is sometimes referred to as a “delay line”. The phase velocity and attenuation rate of the SAW can be determined by measuring the phase delay and input-output amplitude ratio of the signal [19]. The main advantage of SAW sensors compared to QCMs is that IDTs make it easier to generate higher frequencies; this typically translates to higher sensitivities [13, 18]. Operating frequencies for SAW sensors are usually in the range of 25 – 500 MHz [14], with 100 MHz being a typical value [13]. In comparison, standard operating frequencies for QCMs are only 10 – 50 MHz [13].

Mass adsorption is often associated with a phase-velocity shift, and liquids with attenuation. However, this only applies when the adsorbate can be considered “rigid”; the picture is more complicated for a “soft” material. If the adsorbate is a soft material, such as a soft polymer or a layer of biological cells, there is an appreciable attenuation even in dry conditions (i.e., no liquid present). Furthermore, shifting to wet conditions (e.g., submerging the sensor in a liquid) can, in some cases, even *reduce* the attenuation [20]. For now, we will begin by considering the general theory of sound waves in solids.

2.2 Acoustic Waves in Solids

The theory describing the propagation of acoustic waves in solids is the *theory of elasticity* [21] which more generally describes deformations of continuous bodies of solid matter. Any solid continuous body is on the nanoscopic

²Note that “interdigital” means “between fingers” (*digitus*, lat. “finger”).

2.2. ACOUSTIC WAVES IN SOLIDS

level composed of a large number of atoms (or molecules) held together by interatomic (or intermolecular) forces. In the absence of external forces acting on the body, it has some specific shape corresponding to its equilibrium. By applying an external force, e.g., by compressing, stretching, pushing, pulling, or bending the body, its shape can be deformed. The deformation displaces infinitesimal pieces of material from their equilibrium positions. We describe this displacement by a *displacement field* \mathbf{u} , and then define a *strain tensor* u_{ij} in terms of it,

$$\mathbf{u}(\mathbf{r}; t) \equiv \mathbf{r}'(t) - \mathbf{r}, \quad u_{ij}(\mathbf{r}; t) \equiv \frac{1}{2} [\partial_i u_j(\mathbf{r}; t) + \partial_j u_i(\mathbf{r}; t)]. \quad (2.1)$$

Here, \mathbf{r} is the equilibrium position of an infinitesimal piece of material and $\mathbf{r}'(t)$ is the displaced position [21]. At each position in the body, the strain tensor gives the relative change in distances—the *strain*—due to the displacement. As strain constitutes a departure from equilibrium, it inevitably leads to restoring forces. These are described by a *stress tensor* σ_{ij} , the divergence of which is the force density F_i acting on the displacement field according to Newton’s second law [22],

$$\rho \partial_t^2 u_i = F_i = \partial_j \sigma_{ij} \quad (2.2)$$

where ρ is the mass density and summation over repeated indices is implied. If a body is subjected to too much strain, it can become irreversibly deformed, e.g., bent or broken. But if the strain is small enough, the restorative forces are able to pull it back to its equilibrium shape once the external force responsible for the deformation has disappeared [21]. The ability of an object to return to its original shape is known as *elasticity*. The example that likely springs³ to mind when hearing the word “elasticity” is a stretched piece of rubber. Stretch and release the rubber and you can watch it snap back to its original shape. Rubber may be one of the most obvious example of elasticity but actually, as long we only consider “small” (elastically reversible) amounts of strain, many solids behave similarly, albeit with vastly different parameters.

To see how the theory of elasticity can describe sound waves, we need to relate the stress tensor to the displacement field. For an isotropic material, the stress tensor in terms of the strain tensor is [21, 22]

$$\sigma_{ij}(\mathbf{r}; t) = (\mu - 2E)u_{kk}(\mathbf{r}; t)\delta_{ij} + 2\mu u_{ij}(\mathbf{r}; t), \quad (2.3)$$

³Pun noted but not intended.

where the parameters μ and E are the shear and compression moduli, respectively. By combining eqs. (2.2) and (2.3), we get a dynamic equation for the displacement field. The displacement field $\mathbf{u}(\mathbf{r}; t)$ can (like any vector field) be separated into the sum of a zero-curl field, $\mathbf{u}_l(\mathbf{r}; t)$, and a zero-divergence field, $\mathbf{u}_t(\mathbf{r}; t)$. Doing this and taking the curl and divergence of the dynamic equation, we arrive at two uncoupled wave equations [21] which describe the propagation of acoustic *longitudinal* ($i = l$) and *transverse* ($i = t$) waves,

$$\partial_t^2 \mathbf{u}_i(\mathbf{r}; t) = v_i^2 \nabla^2 \mathbf{u}_i(\mathbf{r}; t), \quad i = l, t. \quad (2.4)$$

“Longitudinal” (“transverse”) is here meant in the sense of having zero curl (divergence). In the case of an infinite medium, the two wave equations remain uncoupled and longitudinal and transverse waves propagate independently with speeds $v_l = \sqrt{E/\rho}$ and $v_t = \sqrt{\mu/\rho}$, respectively. However, the introduction of boundary conditions can couple the two fields so that only certain linear combinations of longitudinal and transverse motion are possible. This leads to the appearance of qualitatively different types of waves in the system. Surface acoustic waves (SAWs) are a category of waves which are localized near a surface, and shear-horizontal SAWs (SH-SAWs) are a subcategory of SAWs which have a displacement which is perpendicular to both the propagation direction and the surface normal. In the next section, we will consider a subtype of SH-SAWs propagating in a simple two-layer elastic system. This system will serve as a model of a SAW sensor.

2.3 Love Waves

Let us consider a simple model of a SAW sensor which uses a particular type of SH-SAWs: *Love waves*, named after A. E. H. Love, the mathematician who first predicted them in 1911 [23]. By definition, a SH-SAW has nonzero displacement only in the direction which is perpendicular to both the propagation direction and the surface normal. It is therefore a purely transverse wave with no longitudinal component, so the longitudinal wave equation, eq. (2.4) for $i = l$, is trivially satisfied everywhere; we need only consider the transverse wave equation, $i = t$. For reasons that will eventually become clear, the sensing surface of a Love-wave sensor is usually covered by a thin film of a material different from the substrate [13, 16]. We will therefore model the sensor as an isotropic elastic half-space filling the region $z \leq 0$,

2.3. LOVE WAVES

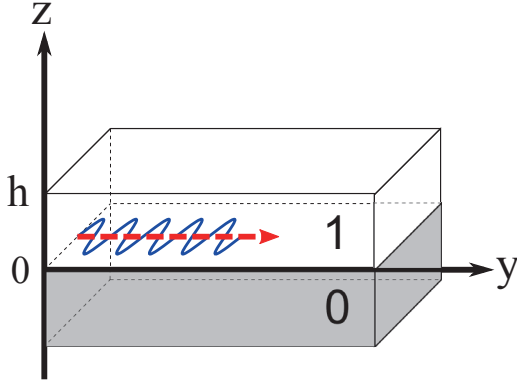


Figure 2.2: A model for a Love-wave sensor. An elastic substrate (0) is covered by an elastic layer (1) with thickness h , the “film”. We consider the propagation of a Love-type SH-SAW (blue) in the y -direction (indicated by the red arrow).

covered by an isotropic elastic layer of finite thickness h , which we will refer to as the “film” (fig. 2.2). The substrate (film) has shear modulus μ_0 (μ_1) and mass density ρ_0 (ρ_1), with derived speed of transverse sound waves $v_i = \sqrt{\mu_i/\rho_i}$. We consider the propagation of a SH-SAW in the y -direction, with displacement in the x -direction, and write down a separate transverse wave equation for each material layer i ,

$$\partial_t^2 u_i(y, z; t) = v_i^2 [\partial_y^2 + \partial_z^2] u_i(y, z; t), \quad i = 0, 1. \quad (2.5)$$

The equations are *scalar* since $\mathbf{u}_i = (u_i, 0, 0)^T$ and the x -independence follows from symmetry. The system is thus effectively 2D because of symmetry. Eq. (2.5) must be supplemented by suitable boundary conditions.

The top of the film, at $z = h$, is a *free surface*. The associated boundary condition is that the product of the stress tensor σ_{ij} [see eq. (2.3)] and the surface normal $\mathbf{n} = (0, 0, 1)^T$ (i.e., the normal component of the stress tensor) should be zero at the surface [21],

$$\sigma_{ij} n_j|_{z=h} = 0, \quad i = x, y, z. \quad (2.6)$$

For the interface between the film and the substrate, at $z = 0$, we will impose continuity of the displacement field and the normal component of the stress tensor [24]. In the limit $z \rightarrow -\infty$, we require that $u_0 \rightarrow 0$ as $z \rightarrow -\infty$ so that the displacement is localized to the surface.

Since the calculations involve only linear operations on the displacement, we will simplify them by considering *complex* displacement fields; the real

displacement fields are simply the real parts. We solve eqs. (2.5) with the given boundary conditions and find

$$\begin{aligned} u_1(y, z; t) &= A_0 e^{-iky+i\omega t} \cosh(\xi[h-z]) \operatorname{sech}(\xi h), \quad \xi = \sqrt{k^2 - (\omega_1/v_1)^2} \\ u_0(y, z; t) &= A_0 e^{-iky+i\omega t} e^{\varkappa z}, \quad \varkappa = \sqrt{k^2 - (\omega_0/v_0)^2}, \end{aligned} \quad (2.7)$$

where A_0 is an overall amplitude not specified by the theory. We can express the wave vector k as a function of \varkappa , the inverse decay length into the bulk substrate. The dispersion relation $\omega(k) = \omega(k[\varkappa])$ is then given by the solutions \varkappa to the transcendental equation

$$\mu_0 \varkappa = -\mu_1 \xi \tanh(\xi h), \quad \varkappa > 0, \quad (2.8)$$

which can be found using numerical techniques. Note that if $h \rightarrow 0$, i.e., the film disappears, then $\varkappa \rightarrow 0$, i.e., the wave delocalizes from the surface. We thus find that an isotropic elastic half-space cannot support Love waves⁴. This is the reason for applying a film to the sensing surface. As can be shown from eq. (2.8), the film must also fulfill another condition: the speed of sound (for transverse bulk waves) in the film must be lower than that in the substrate, $v_1 < v_0$ [16, 25, 26].

We are primarily interested in the phase velocity of the SH-SAW as a function of the film thickness h , since this is what is measured experimentally (see section 2.1). Numerically solving eq. (2.8) for \varkappa allows us to calculate the velocity as $v = \omega/k[\varkappa]$. In fig. 2.3, we plot v as a function of the film thickness h . We use quartz parameters [27] for the substrate ($\mu_0 = 58$ GPa, $\rho_0 = 2.6 \cdot 10^3$ kg/m³), PMMA⁵ parameters [28] for the film ($\mu_1 = 1.7$ GPa, $\rho_1 = 1.2 \cdot 10^3$ kg/m³) and an operating frequency of $\omega/[2\pi] = f = 100$ MHz. We see that for thin films, the velocity is close to that of bulk waves in the substrate, v_0 . As the thickness increases, the velocity drops, ultimately approaching that of bulk waves in the film, v_1 . In fig. 2.4, we plot the displacement field given in eq. (2.7) for three different film thicknesses (indicated in fig. 2.3). We see that increasing the film thickness localizes more of the displacement to the film, which gives us an understanding for why the velocity approaches v_1 . Since the film is used to concentrate the acoustic energy and “guide” the waves, it is sometimes referred to as a “waveguide (layer)” [14, 25, 26, 29]

⁴However, an isotropic elastic half-space can support Rayleigh waves, which we will cover in chapter 3.

⁵Polymethyl methacrylate, a common polymer.

2.3. LOVE WAVES

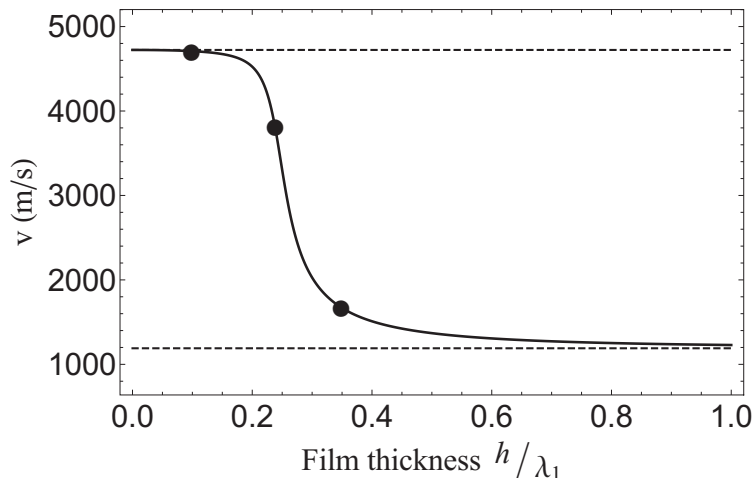


Figure 2.3: The phase velocity of a Love wave in the system depicted in fig. 2.2 as a function of film thickness h scaled by the wavelength in the film $\lambda_1 \approx 12 \mu\text{m}$. For thin films, the velocity is approximately equal to the speed of sound in the bulk substrate v_0 (upper dashed line). For thick films, the velocity approaches the speed of sound in the film v_1 (lower dashed line). The markers, left to right, correspond to the displacement fields plotted in figs. 2.4a–c.

or a “guiding layer” [15, 30, 31]. We can, as an approximation, model the adsorption of particles onto the film as a simple extension of the film thickness h . As seen from fig. 2.3, increasing the thickness lowers the phase velocity of the Love wave, thus rendering the adsorbed mass detectable.

Let us now consider an acoustically thin film, i.e., a film whose thickness is much smaller than the wavelength, $h \ll \lambda_1$. In this regime, we see that the phase velocity is very close to the substrate velocity v_0 (fig. 2.3) and that the wave is weakly localized, i.e., \varkappa is small (fig. 2.4). Therefore, we have a small parameter $\varkappa^2/[\omega/v_0]^2 \ll 1$. Writing $k[\varkappa] = \omega/[v_0 + \Delta v]$, where $\Delta v \ll v_0$, we expand to first order and find that $\Delta v/v_0 \approx -\varkappa^2/[2\omega/v_0]^2$. In order to find \varkappa in this regime, we expand eq. (2.8) to first order in the small parameters. To lowest nonvanishing order, we find [20, 32, 33]

$$\frac{\Delta v}{v_0} \approx -\frac{\omega^2 (v_0^2 - v_1^2)^2}{2v_0^4 \mu_0 \rho_0} [h\rho_1]^2 \quad (2.9)$$

and we see that for acoustically thin elastic films, the surface mass density $[h\rho_1]$ enters to second order.

In this chapter, we only consider Love waves. Other kinds of SH-SAWs require, e.g., an anisotropic or finite substrate [33], and are beyond the scope of this thesis. The above analytical derivation is straightforward to generalize

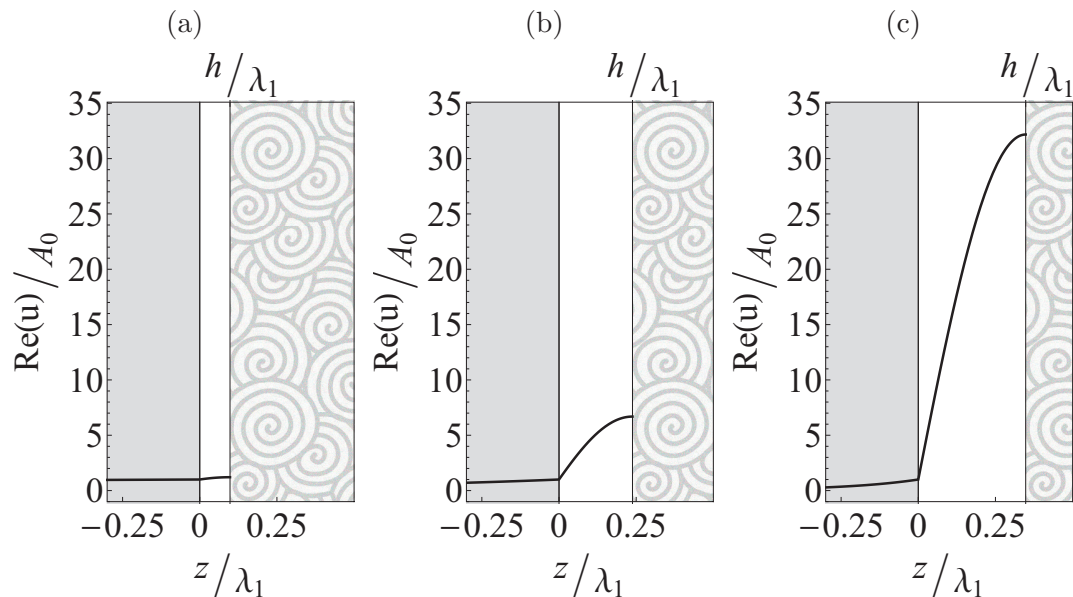


Figure 2.4: The shear displacement (solid black line) as a function of the z -coordinate, for the system depicted in fig. 2.2 and the cases indicated by the markers in fig. 2.3. The substrate (grey) occupies the region $z \leq 0$ and the film (white) $0 < z \leq h$. The free surface at $z = h$ is in contact with, e.g., vapors (spirals) from which particles can be adsorbed. The displacement decays into the substrate and has a vanishing derivative at the surface (zero stress). Increasing h increases the localization of displacement to the film.

to multiple stacked material layers. In the next section, we will do precisely that, but first we will discuss how the theory can be adapted to also allow for *liquid* layers.

2.4 SAW Sensors in Viscous Liquids

In contrast to a solid body, a liquid does not have an intrinsic equilibrium shape. Water in a bottle is bottle shaped, but pour it in a cup and it becomes cup shaped. The reason is that in a liquid, the atoms (or molecules) are not as strongly held together as in a solid; they can move relative to each other. Once a water molecule has been displaced far enough from its starting position, it has gone out of reach of the intermolecular forces that once connected it to its old neighbors. Since there is nothing to pull it back into place, the original configuration cannot be restored. However, as the water molecule flows away from its old neighbors and passes several other water molecules, it feels the intermolecular forces as a kind of friction, and

2.4. SAW SENSORS IN VISCOUS LIQUIDS

thereby loses energy, thus slowing down. Eventually, it has slowed down enough to be caught by some other water molecules. They keep it in place, and the liquid reaches a new equilibrium shape. The internal friction inside a liquid is called its *viscosity*, and it corresponds roughly to the “thickness” of a liquid, e.g., honey has larger viscosity than water. If a viscous liquid rests on top of a surface which vibrates in-plane, the molecular layer which is in contact with the surface is dragged along and made to vibrate. The molecular layer on top of that one is in turn dragged along, and so on. In this way, shear vibrations can propagate into a liquid [34]. However, due to viscous losses—energy losses in the friction between molecular layers—the vibrations decrease with distance and only a thin region of liquid on top of the surface vibrates appreciably. The viscous energy losses in this liquid region attenuates the shear vibrations of the surface. Let us now show how one can arrive at this picture mathematically.

The dynamics of an incompressible (mass density $\rho = \text{constant}$) viscous liquid is given in terms of its flow velocity $\mathbf{V}(\mathbf{r}; t)$ and pressure $p(\mathbf{r}; t)$ by the Navier-Stokes equation [34]

$$\rho \partial_t V_i(\mathbf{r}; t) = \partial_j \sigma_{ij}(\mathbf{r}; t) - \rho \partial_j V_i(\mathbf{r}; t) V_j(\mathbf{r}; t) + \rho \mathbf{g}, \quad i = x, y, z \quad (2.10)$$

where σ_{ij} denotes the *viscous* stress tensor [34],

$$\sigma_{ij}(\mathbf{r}; t) = -p(\mathbf{r}; t) \delta_{ij} + \eta [\partial_i V_j(\mathbf{r}; t) + \partial_j V_i(\mathbf{r}; t)], \quad (2.11)$$

and η is the (dynamic) viscosity of the liquid. The last term in eq. (2.10) is the downward acceleration due to gravity, $\mathbf{g} = (0, 0, -g)^T$, included for completeness. If the liquid rests on top of a surface which performs pure-shear oscillation in the x -direction, the so-called *no-slip condition* [34] equates the velocity of the surface to the velocity of the adjacent liquid and we find that $\mathbf{V} = (V(y, z; t), 0, 0)^T$. The independence of V and all other quantities on x follows from symmetry arguments, as in section 2.3. Inserting this into eq. (2.10), we see that the second term on the RHS, which describes momentum flux due to mass transfer (convection), vanishes, rendering the equations *linear*. We may therefore use complex fields, as we did in section 2.3. Since pure shear does not involve any compression, the pressure p and gravity \mathbf{g} decouple from the equations governing shear vibrations; we therefore exclude them from now on. If we introduce an artificial “liquid displacement field” u via $V = \partial_t u$ and note that, since the considered motion is oscillatory,

$\partial_t u = i\omega u$, we get

$$\partial_t^2 u(y, z; t) = \frac{[i\eta\omega]}{\rho} [\partial_y^2 + \partial_z^2] u(y, z; t), \quad V = \partial_t u. \quad (2.12)$$

This is identical to eq. (2.5), the equation of motion for the SH-SAW displacement in an elastic solid, with an effective *imaginary* shear modulus $\mu = i\eta\omega$. Let us now review the boundary conditions. The no-slip condition is automatically satisfied if we require continuity of the displacement field. In addition, we require continuity of the normal component of the stress tensor. By comparing the stress tensors (2.11) and (2.3) for the case of oscillatory pure shear, we see that the substitution $\mu \rightarrow i\eta\omega$ converts elastic stress to viscous stress. In conclusion, SH-SAW propagation in a viscous layer can be modeled in the same way as in an elastic layer, but with an *imaginary* shear modulus $i\eta\omega$ [30].

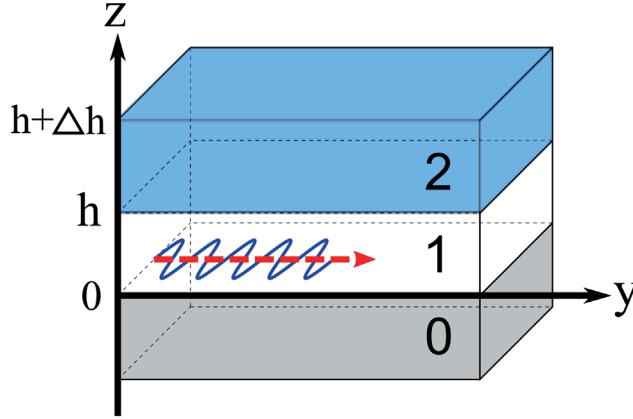


Figure 2.5: A model for a Love-wave sensor in a liquid. An elastic substrate (0) is covered by an elastic film (1) with thickness h . On top is a viscous liquid with depth Δh (which we will take to infinity). We consider the propagation of a Love wave (blue) in the y -direction (indicated by the red arrow).

We now return to our two-layer model of a Love-wave sensor from section 2.3, and add to it a third layer with thickness Δh , consisting of a viscous liquid. We will denote quantities in this layer with index 2 (fig. 2.5). We require continuity of the displacement and the normal component of the stress tensor at the layer interfaces and assume a free surface at $z = h + \Delta h$. We then derive the displacement field in each layer and find a transcendental equation for the dispersion. Finally, we take the limit $\Delta h \rightarrow \infty$ so that

2.4. SAW SENSORS IN VISCOUS LIQUIDS

the top liquid is semi-infinite⁶. The system now models a Love-wave sensor submerged in a viscous liquid. We find

$$\begin{aligned}
 u_2(y, z; t) &= A_0 e^{-iky+i\omega t} \frac{\mu_1 \xi_1 e^{\xi_2(h-x)}}{\mu_1 \xi_1 \cosh(\xi_1 h) + \mu_2 \xi_2 \sinh(\xi_1 h)}, \\
 u_1(y, z; t) &= A_0 e^{-iky+i\omega t} \frac{\mu_1 \xi_1 \cosh(\xi_1[h-x]) + \mu_2 \xi_2 \sinh(\xi_1[h-x])}{\mu_1 \xi_1 \cosh(\xi_1 h) + \mu_2 \xi_2 \sinh(\xi_1 h)}, \quad (2.13) \\
 u_0(y, z; t) &= A_0 e^{-iky+i\omega t} e^{\varkappa z}, \\
 k &= \sqrt{\varkappa^2 + (\omega/v_0)^2}, \quad \xi_1 = \sqrt{k^2 - (\omega/v_1)^2}, \quad \xi_2 = \sqrt{k^2 + (\omega^2 \rho_2 / [i\eta_2 \omega])}.
 \end{aligned}$$

The dispersion relation $\omega(k[\varkappa])$ is found from the *complex* equation

$$\mu_0 \varkappa = \mu_1 \xi_1 \frac{F_- - e^{2\xi_1 h} F_+}{F_- + e^{2\xi_1 h} F_+}, \quad F_{\pm} = \mu_1 \xi_1 \pm \mu_2 \xi_2, \quad \text{Re}(\varkappa) > 0. \quad (2.14)$$

The displacement field decays exponentially into the viscous liquid with a characteristic length of decay $\delta_2 = \sqrt{\omega \rho_2 / (2\eta_2)}$, known as the *depth of penetration* [34]. Due to viscous losses in the liquid, the waves attenuate during propagation. The attenuation coefficient is simply the imaginary part of the wave vector, $\Gamma = -\text{Im}[k]$. The velocity is found from the real part, analogously to section 2.3. Using the same parameters as in section 2.3 and assuming the top liquid to be water ($\eta_2 = 8.9 \cdot 10^{-4}$ Pa s, $\rho_2 = 10^3$ kg/m³), we plot the phase velocity and scaled attenuation coefficient $\Gamma/k \approx \Gamma/[\omega/v_0]$ vs film thickness in fig. 2.6. In fig. 2.7, we plot the displacement field in the three layers for three selected film thicknesses.

Acoustic sensors utilizing pure-shear vibrations are especially suited to liquid applications since the in-plane vibrations only penetrate a small distance into the liquid. In contrast, out-of-plane vibrations can create longitudinal waves which propagate into the liquid, resulting in impractically high viscous losses [13, 16, 35]. Additionally, thin-film sensors have increased sensitivity in wet conditions. To see this, let us (as in section 2.3) consider an acoustically thin film where $h \ll \lambda_1$. However, we now also assume that $k\delta_2 \ll 1$ (long-wavelength approximation). Note that only the real part of \varkappa^2 enters into the velocity shift $\Delta v/v_0$ while the imaginary part appears as the attenuation coefficient (here scaled by k):

$$\frac{\Delta v}{v_0} \approx -\text{Re} \left(\frac{\varkappa^2}{[\omega/v_0]^2} \right), \quad \frac{\Gamma}{k} \approx -\text{Im} \left(\frac{\varkappa^2}{[\omega/v_0]^2} \right). \quad (2.15)$$

⁶Of course, we could have assumed a semi-infinite top layer from the beginning. This approach was used to match that of paper I.

2.4. SAW SENSORS IN VISCOUS LIQUIDS

To lowest nonvanishing order, we get the velocity shift [20]

$$\frac{\Delta v}{v_0} \approx \frac{\omega^{3/2} v_0^2}{2\mu_0^2} \sqrt{2\eta_2 \rho_2} \left(1 - \frac{\omega \eta_2 \rho_2}{\mu_1 \rho_1} \right) [h \rho_1]. \quad (2.16)$$

We see that in the case of an acoustically thin elastic film loaded by a bulk (effectively semi-infinite) viscous liquid, the surface mass density $[h \rho_1]$ enters to *first* order. The attenuation coefficient is [20]

$$\frac{\Gamma}{k} \approx \frac{\omega v_0^2}{2\mu_0^2} \left(\eta_2 \rho_2 + [h \rho_1] \sqrt{2\omega \eta_2 \rho_2} \left\{ 1 + \frac{\omega \eta_2 \rho_2}{\mu_1 \rho_1} \right\} \right), \quad (2.17)$$

which contains a bulk contribution (first term) which is independent of the film thickness h , as well as a term linear in the surface mass density $[h \rho_1]$ (second term). Since the surface mass density now enters to first order rather than second [cf. eqs. (2.9) and (2.16)], we see that a thin film is more sensitive to changes in its thickness (mass adsorption) when loaded by a viscous liquid.

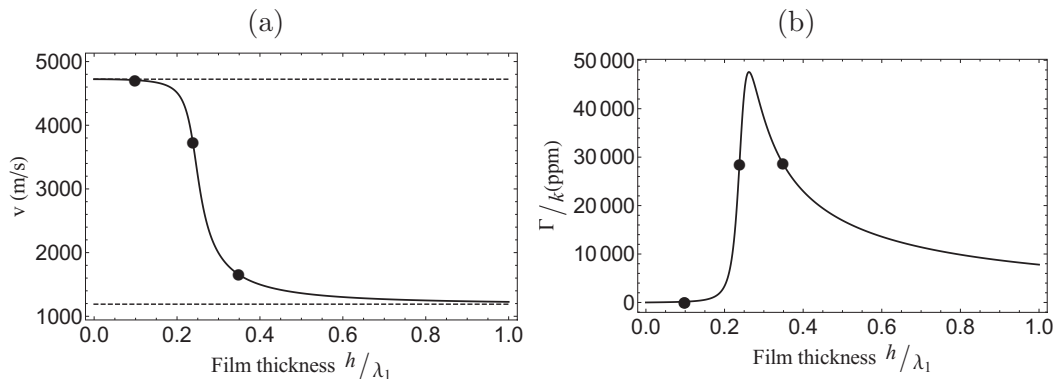


Figure 2.6: The phase velocity (a) and attenuation (b) of a Love wave, in the system depicted in fig. 2.5, as a function of film thickness h scaled by the wavelength in the film, $\lambda_1 \approx 12 \mu\text{m}$. In the velocity plot (a), the bulk velocity in the substrate (film) is indicated by the upper (lower) dashed line. The markers are at the same thicknesses as in the corresponding plot for an elastic film without a liquid (fig. 2.3). The markers, left to right, correspond to the displacement fields plotted in figs. 2.7a–c.

The liquids we have discussed so far have constant viscosity η , thereby making the viscous stress, eq. (2.11), linear in the frequency ω (the rate of shear deformation). This is *Newton's law of viscosity*; materials that obey it are called *Newtonian fluids*⁷, and those that do *not* are called *non-Newtonian*

⁷The word “fluid” refers to both liquids and gases.

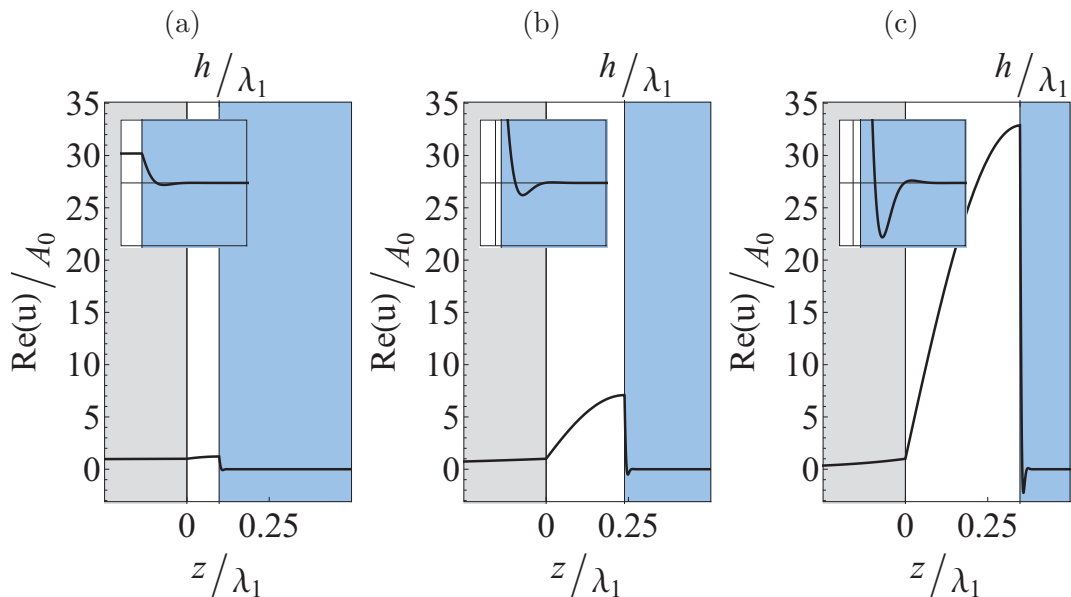


Figure 2.7: The shear displacement (solid black line) as a function of the z -coordinate, for the system depicted in fig. 2.5 and the cases indicated by the markers in fig. 2.6. Markers left to right correspond to figures (a) to (c). The substrate (grey) occupies the region $z \leq 0$ and the film (white) $0 < z \leq h$. At $z = h$, the film has a surface—the sensing surface—facing water (blue), into which the vibrations decays. The inset shows a magnification of the film-liquid interface (the plot range is 0.06 horizontally and $[-2, 2]$ vertically). Note that the “displacement” in the liquid should be understood as the time integral of the flow velocity.

fluids. In general, the viscosity is a function of the deformation rate ω , the local pressure and temperature, the duration of the deformation, etc. In the next section, we will extend the theory to include the frequency dependence; the remaining plethora of dependencies are beyond the scope of this thesis.

2.5 Viscoelastic Materials

Purely elastic solids and purely viscous liquids are useful abstractions, but real materials are not so simple and often display properties of both; they are *viscoelastic*. This is especially true for materials which we intuitively perceive as “soft”, e.g., chewing gum [36], dough [37], and almost anything one comes across in biology [38]. The modeling of viscoelastic layers is therefore of paramount importance in bio-sensing applications. Further, the viscoelasticity of polymers has proven to be an impediment to the commercialization of SAW sensors. Consider again fig. 2.3 showing the phase velocity as a func-

tion of the thickness of a rigid (purely elastic) film. The slope of the curve is the sensitivity to adsorption (increase in film thickness). For an optimal film thickness, yielding maximum sensitivity ($h \approx 0.25\lambda_1$), the adsorption of a few ng/mm^2 onto the sensing surface would yield a phase-velocity shift on the order of meters per second. In practice, however, the films tend to be much thinner than this because of the viscoelasticity of polymers. In order to maximize the sensitivity and to facilitate the generation of Love waves, it is desirable to use films wherein the speed of sound is as low as possible. The films (guiding layers) are usually polymeric for this reason, as well as due to the ease of fabrication⁸ [40]. However, polymers tend to be more or less viscoelastic⁹. As the thickness of the film increases, so do the viscous losses inside it, and the concentration of acoustic energy to the sensing surface is limited by a finite depth of penetration in the film. Therefore, the viscoelasticity of the film both limits the sensitivity and results in viscous losses [26, 30, 31, 41–44]. Understanding viscoelasticity is therefore crucial to the field of SAW sensors.

The mathematical extension of our theory for solids and liquids is straightforward. We have seen that the equations describing Love-wave propagation in elastic solids and viscous liquids are identical. For solids, the shear modulus μ is real, while for viscous liquids, it is imaginary, $\mu \rightarrow i\eta\omega$. By simply defining a *complex* shear modulus, we can incorporate aspects of both. We write¹⁰ $\mu^* = g' + ig''$, where g' is called the *storage modulus*, since it describes elastic storage of energy, and g'' the *loss modulus*, since it describes viscous energy losses [2].

As mentioned in section 2.4, the viscosities η , and thereby the loss moduli g'' , of liquids ($g'' \gg g'$) are in general dependent on the rate of deformation, in our case the oscillation frequency ω . As an illustrative example, consider ketchup [45]. Ketchup exhibits shear-thinning behavior—its viscosity decreases with the rate of deformation. If you simply hold a ketchup bottle upside down, the ketchup will be too thick to flow appreciably. It is not until you shake the bottle that the now seemingly “thinner” ketchup comes pouring out. The shaking decreases the apparent viscosity of the ketchup. In contrast, oobleck—a suspension of cornstarch in water—displays shear-

⁸Polymer films can be applied through spin coating [39].

⁹We neglected the viscous properties of PMMA, both in section 2.3 and in paper I, and treated it as an elastic solid.

¹⁰The asterisk (*) is simply an indicator that the shear modulus is complex and should not be confused with a complex conjugate.

thickening behavior. It can be slowly poured and stirred as a liquid, but with enough speed (and courage), you can actually run on top of it. However, if you slow down to walking speed, you sink. In general, both the storage and loss moduli are frequency dependent [2]: $\mu^*(\omega) = g'(\omega) + ig''(\omega)$. Silly putty [46] flows like a (very) viscous liquid if you let it be, but you can bounce it against the floor like an elastic ball of rubber. Obviously, the form of the functions $g'(\omega)$ and $g''(\omega)$ varies considerably from one material to another. Typically, one resorts to simplified models. In paper I, we employ two such models: the Voigt and Maxwell models [47].

We now have an understanding of how to model Love-wave propagation in layered structures composed of elastic, viscous, and viscoelastic materials, and from these models derive the phase velocity and attenuation coefficient of a Love wave. In the next section, we will simply state the problem tackled in paper I. The methodology is a straight-forward extension of our considerations thus far.

2.6 Summary of Paper I

In paper I, we consider a model with a substrate covered by two additional layers, just as in section 2.4, but allow both upper layers to be viscoelastic by assuming complex shear moduli, as described in section 2.5. Viscous and elastic layers can be recovered in the appropriate limits.

2.6.1 Results: Thin-film Expressions

In the limiting case of an acoustically thin middle layer in a bulk (semi-infinite) top layer, i.e., $|\xi_1 h| \ll 1$ (a generalization of h/λ_1) and $\Delta h \rightarrow \infty$, we find analytical expressions¹¹ for the Love-wave phase-velocity shift:

$$\frac{\Delta v}{v_0} \approx \frac{v_0^2}{2\mu_0^2} \left\{ \rho_2 G' + (G''^2 - G'^2) \frac{1}{v_0^2} + [h\rho_1] \rho_2 (G' K_1 - G'' K_2) \right\}, \quad (2.18)$$

and attenuation coefficient:

$$\frac{\Gamma}{k} \approx \frac{v_0^2 \rho_2}{2\mu_0^2} \left\{ G'' - \frac{2G'G''}{\rho_2 v_0^2} + [h\rho_1] (G'' K_1 + G' K_2) \right\}. \quad (2.19)$$

¹¹Within the long-wavelength approximation.

We have used the notation $\mu_1^* = g' + ig''$ and $\mu_2^* = G' + iG''$ for the viscoelastic moduli and defined

$$\begin{aligned} K_1 &= -\omega \sqrt{\frac{2}{\rho_2}} \left\{ \frac{G'\gamma_- - G''\gamma_+}{G'^2 + G''^2} + \frac{\rho_2 (g'G' + g''G'')\gamma_- - (g'G'' - g''G')\gamma_+}{\rho_1 (g'^2 + g''^2)\sqrt{G'^2 + G''^2}} \right\}, \\ K_2 &= \omega \sqrt{\frac{2}{\rho_2}} \left\{ \frac{G''\gamma_- + G'\gamma_+}{G'^2 + G''^2} - \frac{\rho_2 (g'G' + g''G'')\gamma_+ + (g'G'' - g''G')\gamma_-}{\rho_1 (g'^2 + g''^2)\sqrt{G'^2 + G''^2}} \right\}, \\ \gamma_{\pm} &= \sqrt{\sqrt{G'^2 + G''^2} \pm G'}. \end{aligned} \quad (2.20)$$

Both the phase-velocity shift and the attenuation coefficient contain a contribution from the viscoelasticity of the top layer which does not depend on the middle layer, a “bulk term”. The coefficient of the surface mass density $[h\rho_1]$ depends on the viscoelastic parameters of both overlayers in a complicated manner; increasing the viscosity of a layer does not necessarily imply increased attenuation.

2.6.2 Results: Vanishing Love-wave Support

For certain parameters and film thicknesses, we found that $\text{Re}[\kappa] \leq 0$, corresponding to a delocalization of the Love wave. In other words, the support for Love-wave-type solutions vanished. This occurs beyond a certain film thickness h_c which depends on a multitude of system parameters. For certain parameters, further increasing the film thickness periodically restored and removed Love-wave support.

2.6.3 Discussion & Outlook

The eqs. (2.18) and (2.19) relate the quantities measured by a Love-wave sensor, the phase velocity and attenuation, to the frequency, the film thickness, and material parameters. Analogous expressions have previously been derived in the case when the top layer was a viscous liquid [20]. The expressions are therefore a generalization of earlier results, and also include an additional term in the velocity shift which was neglected in earlier work as it tends to be small in most real applications (high frequencies, low viscosities). Our derived expressions demonstrate the need to consider the nonlinear coupling of the viscoelastic parameters of the layers.

The vanishing of Love-wave support is mathematically complicated to analyze since it arises out of a complex transcendental equation. It is known

2.6. SUMMARY OF PAPER I

that SH-SAWs/Love waves in viscoelastic media have a complicated behavior and that there are several different modes whose dispersion curves intersect [48]. There is also a connection between Love waves and shear horizontally polarized acoustic plate modes, another vibrational mode which is not supported by our semi-infinite substrate model [33]. A more involved analysis would be needed to investigate this issue further; a first step might be to make the substrate finite.

Chapter 3

Edge Electroacoustics

This chapter is a companion piece to papers II and III, which constitute a study of the interaction between 2D SAWs and magnetically induced electronic edge states in a sheet of graphene—“the wonder material”. I will begin by giving some background on graphene, and then give a brief, simplified, and (hopefully) intuitive description of the interaction studied in this chapter. I then proceed by describing the employed theoretical model, devoting one section to the mechanical subsystem, one to the electronic, and finally one to their interaction. I conclude by summarizing and discussing the results of papers II and III.

3.1 Background: Graphene

Carbon atoms are the building blocks of both diamonds and the graphite in your pencil; the difference is in the *structure*. Both diamond and graphite are crystals, i.e., they are made up of a vast number of atoms bonded to each other in a repeating pattern, essentially forming one huge molecule. In diamonds, the carbon atoms make up a complicated three-dimensional structure, while in graphite, they form clearly separated, weakly connected layers of hexagonal grids [49] (fig. 3.1). The long and relatively weak bonds between these layers are what makes pencils work; when the pencil tip rubs against the paper, graphite layers are torn loose and end up affixed to the paper surface. Different versions of the same element that differ only by crystal structure are referred to as *allotropes* of that element, from Greek *allos* (“other”) and *tropos* (“form”). Diamond and graphite are thus both

3.1. BACKGROUND: GRAPHENE

allotropes of carbon. Another carbon allotrope—the *carbon nanotube*—was discovered in 1991 [50]¹. Carbon nanotubes are best described, both visually and mathematically, as a single graphite layer rolled up and connected into a cylindrical tube (periodic boundary conditions). Because of this simple relation to graphite layers, much carried over from earlier theory [52–55].

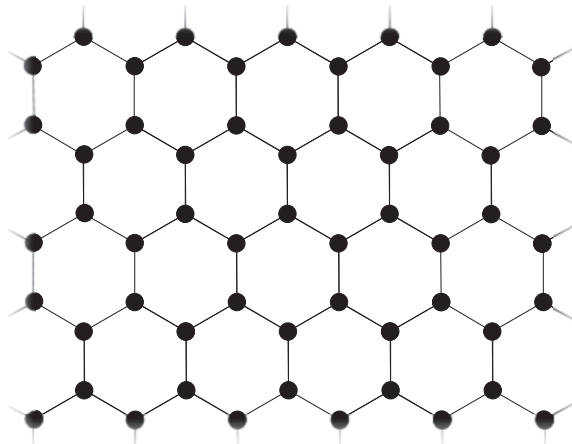


Figure 3.1: The “honeycomb” atomic lattice of graphene. Each black dot represents a carbon atom and the lines connecting them represent atomic bonds. Graphite is made up of several such layers stacked on top of each other, connected by weak bonds.

In 2004, the researchers A. Geim and K. Novoselov successfully isolated *individual* graphite layers [56]. They had thus discovered a new carbon allotrope: a crystal only *one atom* thick. The new material was named “graphene”. While single graphite layers had been studied theoretically for ages, the actual existence of a stable 2D structure had always been considered infeasible [57, 58]. Moreover, the feat had been accomplished by an astonishingly simple technique now known as the “scotch-tape method”—repeated peeling of graphite using scotch tape [56]. Because single graphite layers had always been the starting point when modeling graphite and carbon nanotubes, the theory of graphene predates its discovery; this gave the new material a running start.

Graphene is a 2D membrane, so the electrons within are restricted to movement in a plane. However, graphene is also flexible; it can not just contract and expand, but also vibrate out of plane [59], so the electrons actually

¹Carbon nanotubes had actually been discovered already in 1952 [51], but since the findings were published exclusively in Russian, in a Soviet journal, they were doubly obscured from the global research community by a language barrier and an iron curtain.

move in a *contracting* and *curving* 2D plane. And because of the way the carbon atoms are arranged, it turns out that the equations describing electrons in graphene are identical to those used to describe certain relativistic particles of zero mass [60].

The appeal of the material goes even further. Graphene is a superior conductor of electricity [56, 61], and despite being as thin as physically possible, it is incredibly strong [62]. Its strength has been illustrated by the cartoon picture of a cat sitting safely on a square-meter sheet of graphene supported only at the edges. The graphene would bend, but it would not break, and the mass of the graphene sheet would be roughly that of one of the cat’s whiskers [63]. The strength of graphene is due to the strength of the bonds between the carbon atoms and its hexagonal crystal structure. The hexagonal configuration of carbon atoms is actually the densest possible, since hexagonal tiling (fig. 3.1) is the optimal way to partition a surface into equal geometrical shapes; this is known as the “honeycomb conjecture” [64]. The dense structure makes graphene highly impermeable to gases and liquids [65]. In contrast, its negligible thickness makes it highly transparent to light [66], which is why researchers are currently using it in development of the next generation of touch screens [67].

Graphene is the thinnest [68], densest, strongest [62], most electrically conductive material in the world [56, 61], and a 2D, flexible, transparent [66] membrane with remarkable electronic behavior to boot [59]. For this reason it has been nicknamed “the material of superlatives”. For the purpose of this chapter, what is mainly relevant is that graphene is a 2D elastic material.

3.2 A System Overview

We will consider a sheet of graphene suspended in a perpendicular magnetic field. Electrons in a magnetic field experience a force which is perpendicular to both their velocities and the field, the Lorentz force, which causes them to move in circular orbits whose radii decrease with magnetic field strength (since the force increases and makes them do sharper turns); this is also true for the electrons inside the graphene sheet. If we look at the behavior near an edge of the sheet, we can think of the electrons as “bouncing” against the edge, thereby “skipping” along it (fig. 3.2). We call this image of electron behavior *skipping orbits* and note that the further we move the center of an electron orbit toward and outside the edge, the more tightly the orbits are

3.2. A SYSTEM OVERVIEW

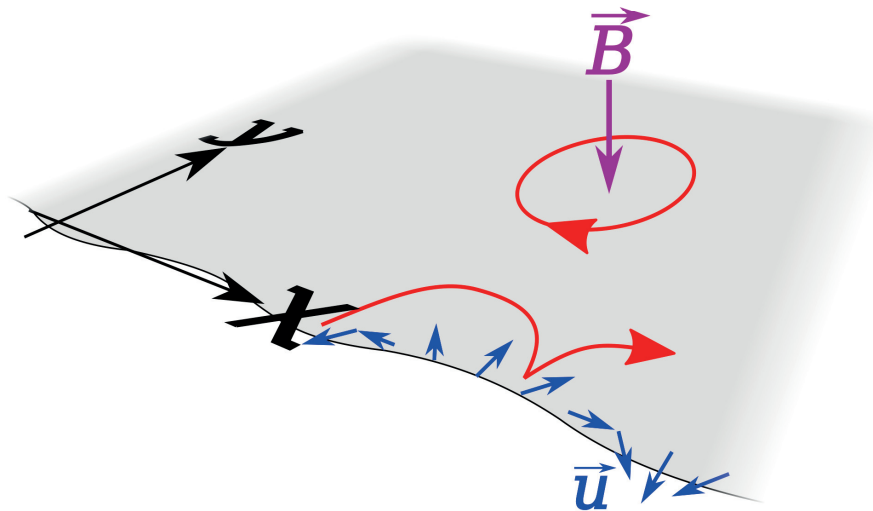


Figure 3.2: A schematic picture of a flat graphene sheet with an edge along the x -axis and an applied perpendicular magnetic field (purple). The electrons (red) follow localized Landau orbits in the bulk, but propagating “skipping orbits” near the edge. Along the edge there are also acoustic edge waves given by a 2D displacement field \mathbf{u} (blue).

squeezed against the edge, so the paths of the electrons become straighter, thereby increasing their effective velocity along the edge. This naïve picture does in fact capture many of the real features of the system. A net flow of electrons constitutes a current, so we can conclude that there are currents running along the edge, but not inside the bulk of the sheet since the electrons there just move in circles. Also, the more tightly the electrons are squeezed against the edge, the higher their velocity. While this classical picture is intuitively useful, we will treat the system quantum mechanically, so rather than classical skipping orbits, we will be considering quantum mechanical electronic *edge states*.

In addition to the skipping-orbit electrons, there are also acoustic waves which propagate along the edge (fig. 3.2). SAWs were introduced in chapter 2; these “edge acoustic waves” are simply their 2D analogue, the edge being a 1D surface. Acoustic waves consist of displacements of the atoms comprising the graphene sheet. As such, they change the local electron density and the lengths of the interatomic bonds. Naturally, the electrons reciprocate by resisting increases in density and deviations from the equilibrium bond length. In other words, acoustic waves interact with electrons. The interaction is especially strong between electronic edge states and acoustic edge waves with

similar localization to the edge. It is this resonant interaction that will be the focus of this chapter. In what follows, we will derive a mathematical framework with which to model it.

3.3 The Mechanical Subsystem

We will use the theory of elasticity, familiar from section 2.2, to treat the graphene sheet as a continuous medium; we thus ignore all details on the atomic level. This description is valid if the separation between the individual carbon atoms, which is on the order of single ångströms [59], is much smaller than the acoustic wavelengths considered. We will begin by introducing and deriving the considered SAW-type of this chapter: Rayleigh waves.

3.3.1 Rayleigh Waves

In chapter 2, we considered Love waves, a type of SAW which requires that the elastic substrate is covered by a film with a lower sound speed². We remarked in section 2.3 that without a film, we are left with a bare elastic half-space and the support for Love waves disappears. However, there is one type of SAW that *can* exist in a bare elastic half-space: Rayleigh waves, named after the physicist who first predicted their existence: Lord Rayleigh³. Rayleigh waves are comprised of both longitudinal and transverse motion. They are used for SAW sensing [69, 70] in dry conditions, but are unsuited for applications in liquids due to their out-of-plane component (see section 2.4). However, in this chapter, we are not concerned with liquids or acoustic sensors, but with the interaction with electrons. Specifically, we will be considering a semi-infinite graphene half-plane $y \geq 0$ with a single edge running along the x -axis (fig. 3.3). We will assume that the graphene sheet remains perfectly flat, i.e., there is no flexural (out-of-plane) motion. Therefore, unlike the systems considered in chapter 2, which were *effectively* 2D by symmetry, the system considered here is *truly* 2D, the edge being a 1D surface. Let us continue from the theory of sound waves laid out in section 2.2 and derive the displacement field and dispersion of Rayleigh waves.

We are solving the transverse and longitudinal wave equations, eqs. (2.4), for the respective components of the 2D displacement field. The param-

²More generally, they require a material-parameter gradient, $\mu(z)$, $\rho(z)$.

³John William Strutt, 3rd Baron Rayleigh.

3.3. THE MECHANICAL SUBSYSTEM

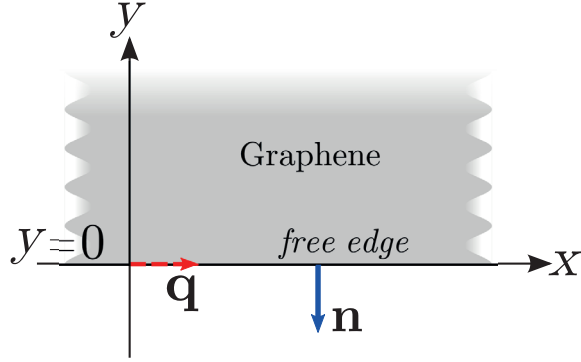


Figure 3.3: The graphene sheet (grey) is treated as a continuous 2D half-plane occupying $y \geq 0$. The edge ($y = 0$) is stress-free and the normal (blue) to the edge is $\mathbf{n} = (0, -1)^T$. Rayleigh waves propagate along the edge (wave vector $\mathbf{q} = (q, 0)^T$, red dashed arrow).

eters are the longitudinal and transverse sound speeds in graphene, $s_l = 2.1 \cdot 10^4$ m/s and $s_t = 1.4 \cdot 10^4$ m/s, respectively⁴ [71]. The 2D geometry is shown in fig. 3.3. We require that $u \rightarrow 0$ as $y \rightarrow \infty$ (SAW condition) and take the edge of the graphene sheet to be a free surface. The boundary condition is thus eq. (2.6) with $i = x, y$ only (2D) and edge normal vector $\mathbf{n} = (0, -1)^T$ (fig. 3.3). In addition, we also have the defining property of the transverse (longitudinal) displacement field: zero divergence (curl). Just as in chapter 2, we choose to work with complex fields for simplicity. However, here we will explicitly denote complex displacement fields with a bar: $\bar{\mathbf{u}}$. We have translational invariance in the x -direction and consider fields with a harmonic time dependence, $\sim \exp(i[qx - \omega t])$, with q being the wave vector x -component⁵.

Edge-localized (SAW) solutions to eqs. (2.4) are given by

$$\bar{\mathbf{u}}_i(x, y; t) = \bar{\mathbf{u}}_i(x, y)e^{-i\omega t} = \mathbf{A}_i e^{-\varkappa_i y + qx - \omega t}, \quad i = l, t \quad (3.1)$$

where \mathbf{A}_l and \mathbf{A}_t are constant 2-vectors and the quantities \varkappa_l and \varkappa_t are the inverse decay lengths into the bulk sheet (cf. \varkappa in chapter 2),

$$\varkappa_i = \sqrt{q^2 - (\omega^2/s_i^2)} > 0, \quad \varkappa_i \in \mathbb{R}, \quad i = l, t, . \quad (3.2)$$

Note that $\varkappa_t \neq \varkappa_l$, i.e., the transverse and longitudinal components have different degrees of localization [21, 72]. The remaining conditions allow us to

⁴Note that, in this chapter, we denote sound speeds with “ s_i ”, reserving “ v_i ” for electronic velocities.

⁵Note that, in this chapter, we use “ q ” for the acoustic wave vector and reserve the letter “ k ” for electronic wave vectors.

3.3. THE MECHANICAL SUBSYSTEM

solve for the constants \mathbf{A}_i up to an overall amplitude A (cf. A_0 in section 2.3) and to find an equation for the Rayleigh wave dispersion. Assuming a linear dispersion, $\omega(q) = \zeta s_t |q|$, we get a fourth-degree equation in the unknown ζ , which we solve numerically. In order for ω , \varkappa_l , and \varkappa_t to be real, we must have ζ real and $0 < \zeta < 1$. These restrictions leave only $\zeta \approx 0.89$, so

$$\omega_R(q) = s_R |q|, \quad (3.3)$$

where $s_R \equiv \zeta s_t = 1.2 \cdot 10^4$ m/s is the speed of Rayleigh waves; we have introduced the index R for ‘‘Rayleigh’’. We define constants λ_t and λ_l in terms of ζ such that that $\varkappa_i = \lambda_i |q|$, and rewrite the displacement field as

$$\bar{\mathbf{u}}_{R,q}(x, y) = A \mathbf{f}_q(y) e^{iqx}, \quad (3.4)$$

with

$$\mathbf{f}_q(y) = \begin{pmatrix} e^{-\lambda_l |q| y} - C_x e^{-\lambda_t |q| y} \\ -i \operatorname{sgn}(q) [-\lambda_l e^{-\lambda_l |q| y} + C_y e^{-\lambda_t |q| y}] \end{pmatrix}, \quad (3.5)$$

where we appended q as an index [21, 72]. The constants in eq. (3.5) all depend only on the ratio s_l/s_t and are close to unity. Specifically, we find

$$\begin{aligned} \lambda_l &= \sqrt{1 - \zeta^2} \approx 0.81, & C_x &= 2\lambda_l \lambda_t / (\lambda_t^2 + 1) \approx 0.61, \\ \lambda_t &= \sqrt{1 - (s_t/s_l)^2 \zeta^2} \approx 0.46, & C_y &= C_x / \lambda_t \approx 1.3. \end{aligned} \quad (3.6)$$

The *real* displacement field $\mathbf{u}_{R,q}$ is

$$\mathbf{u}_{R,q}(x, y; t) \equiv \frac{1}{2} (\bar{\mathbf{u}}_{R,q}(x, y) e^{-i\omega_R(q)t} + \bar{\mathbf{u}}_{R,q}^*(x, y) e^{i\omega_R(q)t}). \quad (3.7)$$

which is given in eq. (2)⁶ in paper II.

Rayleigh waves move slower than bulk waves, $s_R < s_t < s_l$, and are localized to the edge on the order of the wavelength. The waves take the shape of a ‘‘rolling’’ in-plane displacement along the edge (fig. 3.4), somewhat reminiscent of ocean waves. Since Rayleigh waves oscillate in the plane spanned by the surface normal and the propagation direction, they are 2D objects even in 3D systems, and typically the 3D Rayleigh-wave solutions are found by a 2D calculation which neglects the third dimension due to symmetry [21, 22, 72], similarly to how we treated Love waves in section 2.3. However, our system is *actually* 2D and the ‘‘surface’’ is the edge of the graphene sheet.

⁶When comparing with paper II, note that $2u_0 = A$.

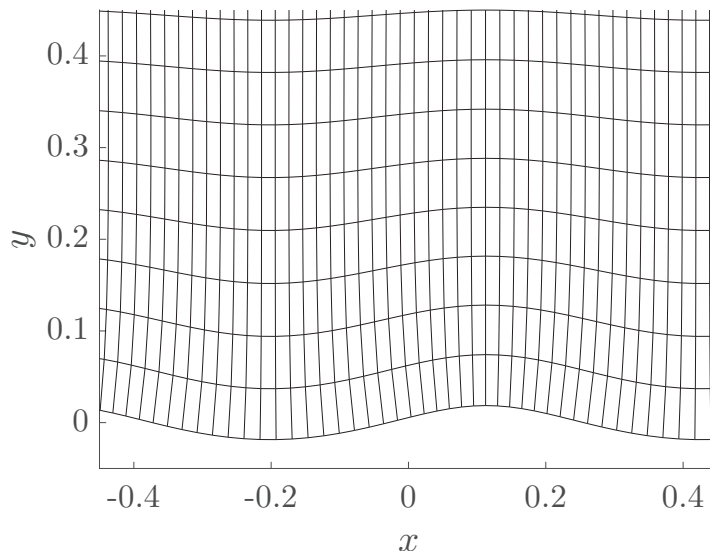


Figure 3.4: A snapshot of Rayleigh waves along an edge (at $y = 0$). The displacement field is according to eqs. (3.4) and (3.5), with arbitrary units.

3.3.2 A Quantized Acoustic Hamiltonian

Here, we will present a classical acoustic Hamiltonian from which the wave equations for acoustic waves, eqs. (2.4), can be derived. In chapter 2, a Hamiltonian formalism was not possible since the total energy of the system was not conserved due to viscous losses. Introducing a Hamiltonian will allow us to easily quantize the acoustic subsystem and then couple it to an electronic subsystem.

In section 2.2, we introduced the displacement field $\mathbf{u}(\mathbf{r})$ as the dynamic variable describing acoustic waves. By introducing a momentum $\boldsymbol{\pi}(\mathbf{r})$ conjugate to $\mathbf{u}(\mathbf{r})$, we can write a classical Hamiltonian [22] as⁷

$$H_{\text{ac}} = \iint \frac{\boldsymbol{\pi}^2(\mathbf{r})}{2\rho_{\text{gr}}} - \frac{\rho_{\text{gr}}}{2} \mathbf{u}(\mathbf{r}) \cdot \mathcal{L} \mathbf{u}(\mathbf{r}) \, dx \, dy \quad (3.8)$$

where $\rho_{\text{gr}} = 7.6 \cdot 10^{-7} \text{ kg/m}^2$ is the 2D mass density of graphene [73], and \mathcal{L} is a linear operator acting on $\mathbf{u}(\mathbf{r})$ defined as

$$\mathcal{L} = s_t^2 \mathbf{grad} \, \text{div} - s_t^2 \mathbf{curl} \, \text{curl}. \quad (3.9)$$

⁷Note that the integration is over the half-plane: $-\infty < x < \infty$, $0 \leq y < \infty$.

Hamilton's equations then yield the equation of motion for $\mathbf{u}(\mathbf{r})$ as [22]

$$\partial_t^2 u_i(\mathbf{r}; t) = L_{ij} u_j(\mathbf{r}; t) = \rho_{\text{gr}}^{-1} \partial_j \sigma_{ij}. \quad (3.10)$$

We recognize eq. (3.10) as eq. (2.2). We can thus recover the wave equations for sound waves, eqs. (2.4), from the Hamiltonian given in eq. (3.8). To quantize the acoustic subsystem, we can simply replace the displacement field and its conjugate momentum with operators which obey the canonical commutation relation, $[\hat{u}_i(\mathbf{r}), \hat{\pi}_j(\mathbf{r}')] = i\hbar \delta(\mathbf{r} - \mathbf{r}') \delta_{ij}$. The quantized version of the classical Hamiltonian in eq. (3.8) is then simply

$$\hat{H}_{\text{ac}} = \iint \frac{\hat{\boldsymbol{\pi}}^2(\mathbf{r})}{2\rho_{\text{gr}}} - \frac{\rho_{\text{gr}}}{2} \hat{\mathbf{u}}(\mathbf{r}) \cdot \mathcal{L} \hat{\mathbf{u}}(\mathbf{r}) \, dx \, dy \quad (3.11)$$

and the equations of motions in the Heisenberg picture replicate the classical equations of motion.

3.3.3 Eigenwaves & Phonons

When we consider the equation of motion, eq. (3.10), and assume that the (complex) displacement field $\bar{\mathbf{u}}_{m,\mathbf{q}}(\mathbf{r}; t)$ is *harmonic* with frequency $\omega_m(q)$, we get an eigenvalue equation with eigenvalue $-\omega_m^2(q)$ and ‘‘eigenwave’’ $\bar{\mathbf{u}}_{m,\mathbf{q}}(\mathbf{r})$; the index m labels different modes (wave types) and \mathbf{q} is the wave vector. It can be shown [22, 74] that the set of all eigenwaves constitute a complete basis for all displacement fields which satisfy the equation of motion and the boundary condition. When we quantize the eigenwave expansion of a displacement field, the expansion coefficients $\hat{b}_m(\mathbf{q})$ [$\hat{b}_m^\dagger(\mathbf{q})$] become annihilation [creation] operators for *phonons* of type $\{m, \mathbf{q}\}$. The creation of one phonon corresponds to a minimal excitation of the amplitude of its corresponding eigenwave. The eigenwave basis diagonalizes the Hamiltonian \hat{H}_{ac} into a sum of terms $\hbar\omega_m(q)\hat{b}_m^\dagger(\mathbf{q})\hat{b}_m(\mathbf{q})$ which simply count the number of phonons and add their energies.

In papers II and III, the only type of eigenwaves we consider are Rayleigh waves, $m = R$ and $\mathbf{q} = (q, 0)$, since we expect them to interact most strongly with electronic edge states when they are localized to the edge on the same length scale. A quantized real displacement field consisting only of Rayleigh waves can be written

$$\hat{\mathbf{u}}_R(\mathbf{r}) = \int \frac{dq}{2\pi} \sqrt{\frac{\hbar|q|}{2\rho_{\text{gr}}\omega_R(q)}} N_{\text{ac}} \left[\hat{b}_R(q) e^{iqx} \mathbf{f}_q(y) + \hat{b}_R^\dagger(q) e^{-iqx} \mathbf{f}_q^*(y) \right] \quad (3.12)$$

where the eigenwave normalization required for $[\hat{b}_R(q), \hat{b}_R(q')] = \delta(q - q')$ introduced the material constant

$$N_{\text{ac}} = \left(|q| \int_0^\infty \mathbf{f}_q^*(y) \cdot \mathbf{f}_q(y) dy \right)^{-1/2} \approx 1.2. \quad (3.13)$$

3.4 The Electronic Subsystem

Ultimately, the graphene sheet will be treated as a continuous medium, so we are not interested in details on the atomic level. However, the standard electronic theory of graphene is based on the underlying honeycomb lattice structure. It is in fact the hexagonal symmetry of the lattice which gives rise to the special electronic behavior [53, 59]. Therefore, we will begin this chapter at the atomic level and build up the constituents of the theory, then gradually “zoom out” to a larger length scale in which the details of the lattice structure are obscured.

3.4.1 The Graphene Low-Energy Hamiltonian

The standard description of electrons in graphene starts out from a tight-binding model for the honeycomb lattice. It is then seen in the spectrum that low-energy properties are well described by an effective model in which the Schrödinger equation has a form reminiscent of the 2D Dirac equation describing relativistic zero-mass fermions [59, 75].

Let us start with an infinite graphene sheet, without any edge or magnetic field. It consists of a 2D hexagonal honeycomb lattice of atomic bonds, where each vertex is occupied by a carbon atom. Thus each carbon atom is bonded to three neighboring atoms with one electron to spare, that of the $2p_z$ -orbital; these unbonded electrons are the dominant contribution to transport properties [53]. In the hexagonal lattice, there are two inequivalent atoms in each unit cell, A and B [53, 59]. The lattice formed by all the A -atoms (B -atoms) is called the A -sublattice (B -sublattice). We will choose the A -sublattice as the Bravais lattice and include the B -atoms via a two-atom basis. We define lattice vectors for sublattice A and nearest-neighbor vectors linking the two sublattices as in fig. 3.5a. The lattice vectors are

$$\mathbf{a}_1 = a \left(-\frac{1}{2}, -\frac{\sqrt{3}}{2} \right), \quad \mathbf{a}_2 = a \left(\frac{1}{2}, -\frac{\sqrt{3}}{2} \right), \quad (3.14)$$

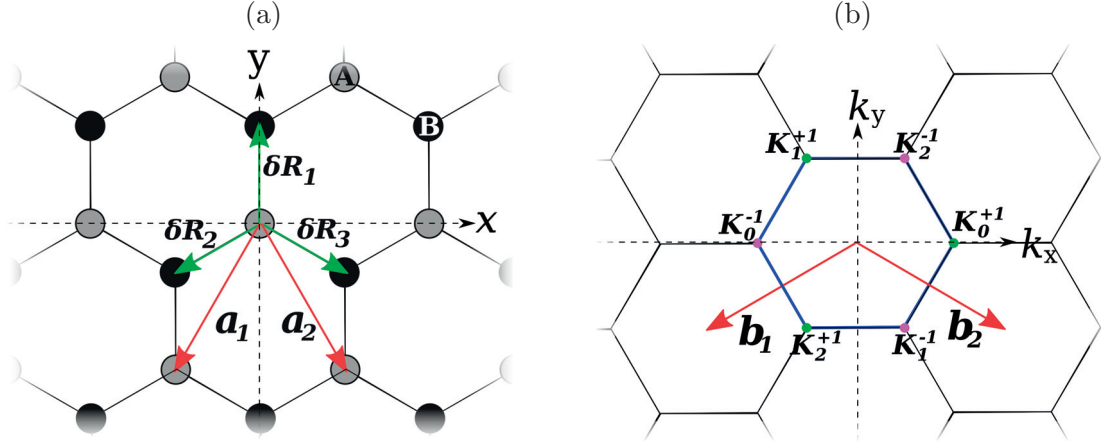


Figure 3.5: (a) The real-space lattice of graphene. There are two atoms per unit cell, labeled A (grey) and B (black). The A -sublattice lattice vectors are \mathbf{a}_1 and \mathbf{a}_2 (red) and each A -atom has three neighboring B -atoms, with nearest-neighbor vectors $\delta\mathbf{R}_n$, $n = 1, 2, 3$ (green). (b) The reciprocal lattice of graphene. The reciprocal lattice vectors are \mathbf{b}_1 and \mathbf{b}_2 (red) and the points at the corners of the first Brillouin zone (blue hexagon), $\mathbf{K}_\sigma^{(\tau)}$, are labeled by $\sigma = 0, 1, 2$, and $\tau = +1$ (green) and $\tau = -1$ (magenta).

where $a = 2.46 \text{ \AA}$ is the lattice constant [53, 59], and the vectors from an A -atom to its nearest neighbors are

$$\delta\mathbf{R}_1 = a \left(0, \frac{1}{\sqrt{3}} \right), \delta\mathbf{R}_2 = a \left(-\frac{1}{2}, -\frac{1}{2\sqrt{3}} \right), \delta\mathbf{R}_3 = a \left(\frac{1}{2}, -\frac{1}{2\sqrt{3}} \right). \quad (3.15)$$

The reciprocal lattice vectors are

$$\mathbf{b}_1 = \frac{2\pi}{a} \left(-1, -\frac{1}{\sqrt{3}} \right), \quad \mathbf{b}_2 = \frac{2\pi}{a} \left(1, -\frac{1}{\sqrt{3}} \right), \quad (3.16)$$

and the reciprocal lattice is also hexagonal, but rotated 90° with respect to the real lattice (fig. 3.5b).

Each carbon atom in the lattice has one unhybridized orbital, the $2p_z$ -orbital, associated with the free electron of that atom. We take these orbitals to be normalized and neglect any overlap between orbitals belonging to different atoms so that the set of all such $2p_z$ -orbitals can be used as a tight-binding orthonormal basis. We define the ket $|2p_z, \mathbf{R}\rangle$ as the atomic $2p_z$ -orbital of the carbon atom at lattice site \mathbf{R} . If we consider only interaction between

3.4. THE ELECTRONIC SUBSYSTEM

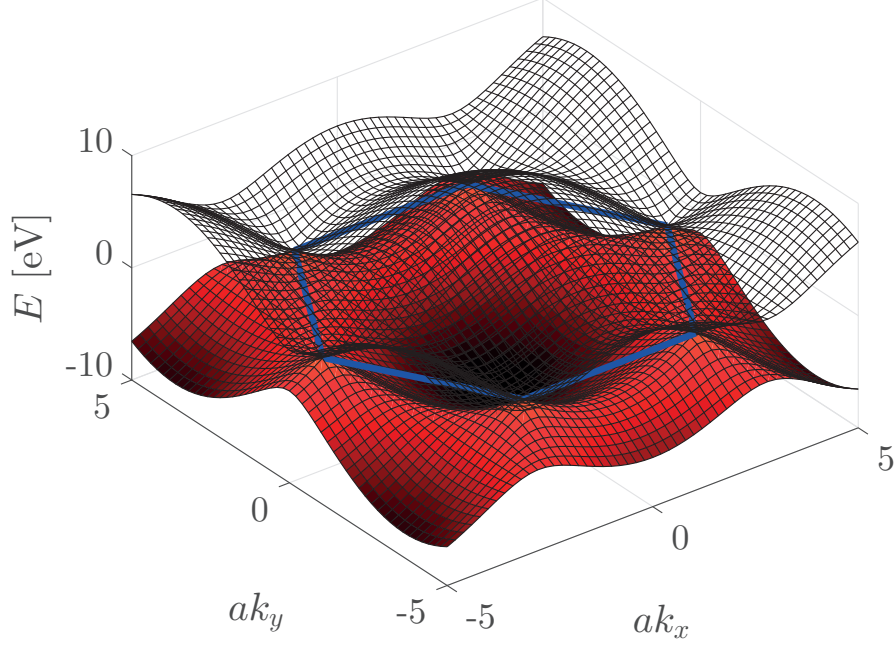


Figure 3.6: The nearest-neighbor tight-binding energy spectrum of graphene with $\epsilon_{2p} = 0$, hopping energy $t = 3$ eV and zero atomic wave function overlap. In the ground state, the conduction band (transparent mesh) is completely empty and the valence band (orange-red) is completely filled. The two bands touch at the corners of the hexagonal first Brillouin zone (blue) as defined in fig. 3.5b.

nearest neighbors⁸, we can write a tight-binding single-electron Hamiltonian

$$\hat{H} = \sum_{\mathbf{R}_A} \sum_{n=1}^3 -t_n |\mathbf{R}'_A + \boldsymbol{\delta}\mathbf{R}_n\rangle \langle 2p_z, \mathbf{R}_A| + \text{H.c.}, \quad (3.17)$$

where $-t_n$ is the hopping energy between nearest neighbors [53, 59] and N is the number of unit cells. There are no diagonal matrix elements of the form $\langle 2p_z, \mathbf{R} | \hat{H} | 2p_z, \mathbf{R} \rangle$; they are equal to the energy of the $2p_z$ -orbital, which we put to zero by choosing it as our reference energy, $\epsilon_{2p} \equiv 0$.

We now introduce a tight-binding basis set of Bloch functions for the

⁸We will justify the nearest-neighbor approximation and neglecting the orbital overlap later in the section.

single-electron state:

$$\begin{aligned}
 |A, \mathbf{k}\rangle &= \frac{1}{\sqrt{N}} \sum_{\mathbf{R}_A}^N e^{i\mathbf{k}\cdot\mathbf{R}_A} |2p_z, \mathbf{R}_A\rangle, \\
 |B, \mathbf{k}\rangle &= \frac{1}{\sqrt{N}} \sum_{\mathbf{R}_A}^N \sum_{n=1}^3 e^{i\mathbf{k}\cdot(\mathbf{R}_A+\delta\mathbf{R}_n)} |2p_z, \mathbf{R}_A + \delta\mathbf{R}_n\rangle.
 \end{aligned} \tag{3.18}$$

Expressing the Hamiltonian in eq. (3.17) in this basis, we get

$$\hat{H} = \sum_{\mathbf{k}} F(\mathbf{k}) |B, \mathbf{k}\rangle \langle A, \mathbf{k}| + \text{H.c.}, \quad F(\mathbf{k}) \equiv \sum_{n=1}^3 -t_n e^{-i\mathbf{k}\cdot\delta\mathbf{R}_n}. \tag{3.19}$$

We assume that the hopping energy between nearest-neighbors does not depend on the direction and write $t_1 = t_2 = t_3 \equiv t$. The hopping-energy parameter is commonly taken as $t \approx 3$ eV [53, 55, 59]. The Hamiltonian is easily diagonalized and we find that the energy spectrum is given by [53, 59]

$$E_{\pm}(\mathbf{k}) = \pm |F(\mathbf{k})|t. \tag{3.20}$$

The “ \pm ” corresponds to the valence and conduction band (fig. 3.6). Given Born-von-Karman boundary conditions [49], the number of states in a band is equal to twice (due to spin) the number of unit cells in the lattice. In graphene, there are two free electrons per unit cell, one per carbon atom, and thus we find that in the ground state, the valence band is completely filled and the conduction band is completely empty. The two bands touch at the corners of the first Brillouin zone (fig. 3.6). We denote these points $\mathbf{K}_{\sigma}^{(\tau)}$ where $\tau = \pm 1$ labels opposite corners, and $\sigma = 0, 1, 2$ labels the three pairs of opposite corners (fig. 3.5b). For low energies, around $E < 2 - 3$ eV, i.e., a temperature on the order of 10^4 K, the electronic system is well described in the vicinity of these points, so we construct an effective model [55, 59] by expanding the function $F(\mathbf{k})$ to first order. Defining $\mathbf{k}' \equiv \mathbf{k} - \mathbf{K}_{\sigma}^{(\tau)}$,

$$F(\mathbf{k}) \approx \sum_{n=1}^3 -t e^{-i\mathbf{K}_{\sigma}^{(\tau)}\cdot\delta\mathbf{R}_n} (1 - i\mathbf{k}' \cdot \delta\mathbf{R}_n). \tag{3.21}$$

The small parameter in this expansion is $|\mathbf{k}'|a$, so this amounts to the continuum limit where the lattice constant is small compared to the wavelength.

3.4. THE ELECTRONIC SUBSYSTEM

We now drop the prime on \mathbf{k}' and simply measure \mathbf{k} from the closest point $\mathbf{K}_\sigma^{(\tau)}$. Points $\mathbf{K}_\sigma^{(\tau)}$ of the same τ can be shown to differ from each other by a reciprocal lattice vector, and are thus equivalent. We expect that the spectrum will be independent of σ . Considering the geometry of the reciprocal lattice (fig. 3.5b) and using eqs. (3.21) and (3.15), we get a low-energy Hamiltonian for the K - K' pair denoted by σ [55, 59],

$$\hat{H}_\sigma = \sum_{\tau=\pm 1} e^{-i\tau\sigma\frac{2\pi}{3}} \hbar v_F \tau (k_x + i\tau k_y) |B, \mathbf{k}, \sigma, \tau\rangle \langle A, \mathbf{k}, \sigma, \tau| + \text{H.c.}, \quad (3.22)$$

where we used that $\tau^2 = 1$ and introduced (what will be seen to be) the Fermi velocity of graphene [59] as $[at\sqrt{3}/(2\hbar)] \equiv v_F \approx 10^6$ m/s. Considering different pairs of points σ merely introduces a phase factor which does not affect the spectrum, as was expected. However, for each σ , τ labels two inequivalent points, commonly called the “ K -point” ($\tau = +1$) and the “ K' -point” ($\tau = -1$). We arbitrarily choose $\sigma = 0$ and suppress this index. This corresponds to the points $\mathbf{K}^{(\tau)} = (\tau K_x, 0)$. As a matter of preference, we also make the unitary transformation $\hat{U} \hat{H} \hat{U}^\dagger \equiv \hat{H}_{\text{el}}$, where

$$\hat{U} = \sum_{\tau=\pm 1} |A, \mathbf{k}, \tau\rangle \langle A, \mathbf{k}, \tau| + \tau |B, \mathbf{k}, \tau\rangle \langle B, \mathbf{k}, \tau|. \quad (3.23)$$

The K - and K' -points are not coupled and can be treated separately, $\hat{H}_{\text{el}} = \sum_\tau \hat{H}_{\text{el}}^{(\tau)}$. The Schrödinger equation for the point K/K' ($\tau = +1/-1$) is

$$\hbar v_F \begin{pmatrix} 0 & k_x - i\tau k_y \\ k_x + i\tau k_y & 0 \end{pmatrix} \begin{pmatrix} \psi_A^{(\tau)}(\mathbf{k}) \\ \tau \psi_B^{(\tau)}(\mathbf{k}) \end{pmatrix} = E \begin{pmatrix} \psi_A^{(\tau)}(\mathbf{k}) \\ \tau \psi_B^{(\tau)}(\mathbf{k}) \end{pmatrix}, \quad (3.24)$$

$$\boldsymbol{\psi}_{(\tau)}(\mathbf{k}) \equiv (\psi_A^{(\tau)}(\mathbf{k}), \tau \psi_B^{(\tau)}(\mathbf{k}))^T.$$

The electronic states are now described by vectors, $\boldsymbol{\psi}_{(\tau)}(\mathbf{k})$, sometimes called *pseudospinors*. However, the components indicate the sublattice, not spin. Note that \mathbf{k} is always measured from the point in question, and that $\psi_A^{(\tau)}(\mathbf{k})$ and $\psi_B^{(\tau)}(\mathbf{k})$ are the components of the wave function in the basis given by eq. (3.18).

The spectrum in this effective model is, for both K and K' ,

$$E_\pm^{(\tau)}(\mathbf{k}) = \pm \hbar v_F |\mathbf{k}|, \quad \tau = \pm 1, \quad (3.25)$$

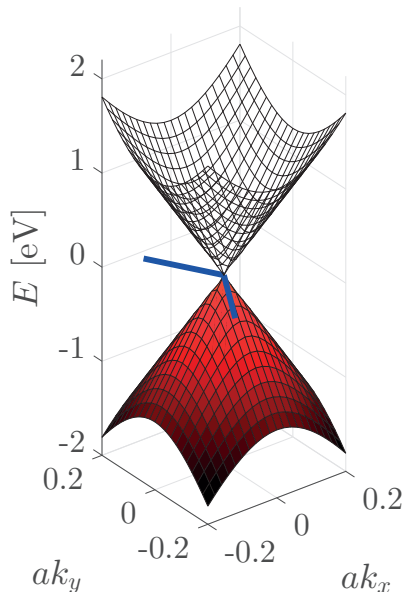


Figure 3.7: The effective-model (low-energy) spectrum of graphene around a K - or K' -point, at a corner of the first Brillouin zone (blue), cf. figs. 3.6 and 3.5b.

i.e., two mirrored cones on top of each other [53], with coinciding zero-energy apexes at the K -point (K' -point) (fig. 3.7). The spectrum around the K -point (K' -point) is sometimes referred to as the K -valley (K' -valley), a spectrum of this kind is known as a *Dirac cone*, and the point where the cones touch is called a *Dirac point*. The vanishing density of states at the Dirac point has led to graphene being labeled a “zero-gap semiconductor” [56, 76]. It is remarkable that eq. (3.24) is identical to the 2D Dirac equation for massless fermions [75], but with the speed of light replaced by v_F [59], the Fermi velocity⁹.

In deriving eq. (3.24) we neglected the overlap of atomic orbitals and kept only nearest-neighbor interaction. It can be shown that both the overlap and the second-nearest-neighbor interaction enter into the spectrum to second order in $|\mathbf{k}|$ [55], so in this regard, neglecting the overlap and the second-nearest-neighbor interaction is subsumed by the approximation made in doing a linear expansion in \mathbf{k} . In addition, the second-nearest-neighbor interaction introduces a constant energy shift. However, that energy shift is

⁹This is a crucial point. Too often in popular science writing are electrons in graphene described as “moving with the speed of light”. However, it is not the *speed* that is similar to relativistic particles ($v_F \ll c$), but the dispersion relation.

3.4. THE ELECTRONIC SUBSYSTEM

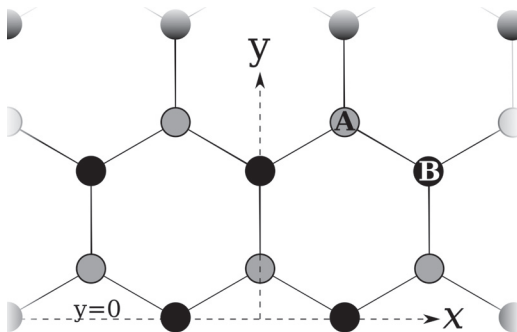


Figure 3.8: A graphene zigzag edge of B -atoms (black) along the x -axis at $y = 0$. At the edge, there are no A -atoms (grey), hence the wave function should vanish on the A -sublattice.

at least an order of magnitude lower than t [59].

We now have a Hamiltonian for the electronic subsystem which in itself makes no reference to the lattice structure. The pseudospinor components are envelope functions for the tight-binding Bloch functions corresponding to the two inequivalent sublattices, and we express the components with a continuous position variable, neglecting the fact that the A - and B -atoms are in different positions. In our continuum model, the sheet is continuous and at each position $\mathbf{r} = (x, y)$, the wave function has both an A - and a B -component. The Hamiltonian in eq. (3.24) is often used as a starting point in calculations without reference to the underlying lattice structure. This is valid in the cases where the discreteness of the lattice can be safely neglected [77–79].

We conclude this subsection by noting that a second-quantized electronic Hamiltonian can be written in terms of sublattice-space Pauli matrices σ_i as

$$\hat{H}_{\text{el}} = \sum_{\tau=\pm 1} \iint \hat{\psi}^\dagger(x, y) \hat{H}_{\text{el}}^{(\tau)} \hat{\psi}(x, y) dx dy, \quad (3.26)$$

$$\hat{H}_{\text{el}}^{(\tau)} = v_F(\sigma_x \hat{p}_x + \tau \sigma_y \hat{p}_y),$$

where we took $\hbar k_i \rightarrow \hat{p}_i$.

3.4.2 The Zigzag Edge

We have so far only considered an infinite sheet. To introduce an edge into our system, we must construct suitable electronic boundary conditions. As was

the case for the electronic Hamiltonian, the electronic boundary conditions are derived from the lattice structure. In theoretical graphene physics we typically neglect the disordered and uneven edges of real graphene sheets, and distinguish between only two types: zigzag and armchair edges [59]. Here we will assume the graphene half-plane to be bounded by a zigzag edge of B -atoms along the x -axis at $y = 0$ (fig. 3.8). All atoms on the zigzag edge belong to the B -sublattice, so at the edge the electronic wave function must vanish on the “missing” A -sublattice, meaning that the effective-model pseudospinor A -component must be zero. Considering the (position-space) wave function, the electronic boundary condition is [59, 78, 80]

$$\Psi_A(x, 0) = e^{iK_x x} \psi_{A,+1}(x, 0) + e^{-iK_x x} \psi_{A,-1}(x, 0) = 0, \quad (3.27)$$

which includes terms from both Dirac points. Since the system is translationally invariant along x , we must have

$$\psi_{k_x, \tau}(x, y) = e^{ik_x x} \phi_{k_x, \tau}, \quad \phi_{k_x, \tau} = \begin{pmatrix} \phi_{A, k_x, \tau}(y) \\ \phi_{B, k_x, \tau}(y) \end{pmatrix}, \quad (3.28)$$

which, together with eq. (3.27), means that we must have

$$\phi_{A, k_x, \tau}(0) = 0, \quad \tau = \pm 1. \quad (3.29)$$

Eq. (3.29) is the electronic boundary condition of our system: the pseudospinor A -component must vanish at the edge for both valleys separately. The fact that zigzag boundary conditions do not mix valleys means that the K - and K' -points can still be treated separately. This is in contrast to an armchair edge, which can be shown to mix valleys [59, 78, 80]. In fact, the edge was chosen as zigzag on account of this simplifying property.

3.4.3 Magnetically Induced Edge States

Here, we will derive the electronic spectrum and energy eigenfunctions in the presence of a magnetic field, perpendicular to the graphene half-plane, i.e., $\mathbf{B} = -B\mathbf{e}_z$ where \mathbf{e}_z is the z -direction unit vector, normal to the sheet, and $B > 0$ (see fig. 3.2). We neglect spin, which we will comment on later, and represent the field by a vector potential in the Landau gauge, $\hat{\mathbf{A}}_B = B\hat{y}\mathbf{e}_x$, which we introduce into the electronic Hamiltonian of eq. (3.26) via the minimal coupling $\hat{p}_i \rightarrow \hat{p}_i + e\hat{A}_i$ (the electron charge is $-e < 0$). In this

3.4. THE ELECTRONIC SUBSYSTEM

way, the magnetic vector potential couples the position in the y -direction and the x -component of the momentum. We will eventually find that the energy eigenfunctions corresponding to large positive momentum in the x -direction are localized near the edge and have a finite velocity along it. This has a correspondence to the classical skipping orbits discussed in section 3.2, whose paths became straighter when the y -position of the orbit center is moved further toward and even over the edge.

The magnetic field introduces a characteristic length scale into the system, the magnetic length

$$l_B \equiv \sqrt{\hbar/|eB|} \approx 26 \text{ nm}/\sqrt{B[\text{T}]} \quad (3.30)$$

where $B[\text{T}]$ (dimensionless) is the magnetic field strength in Tesla. In order for our continuum picture of the graphene sheet to be valid, we must have that the magnetic length is much larger than the distance between atoms, which is on the order of ångströms [59]. This condition is satisfied for magnetic fields of a few mT. We nondimensionalize the problem by defining $\tilde{x} \equiv x/l_B$, $\tilde{k}_x \equiv l_B k_x$ and analogously for the y -coordinate. Also, we define a dimensionless energy as

$$\tilde{E} = E/E_B, \quad E_B \equiv \sqrt{2}\hbar v_F/l_B. \quad (3.31)$$

Similarly to the valley index $\tau = \pm 1$, we introduce the sublattice index σ , where $\sigma = +1$ ($\sigma = -1$) indicates the pseudospinor A -component (B -component)¹⁰. We get four coupled equations:

$$(\hat{\tilde{k}}_x + \hat{\tilde{y}} + i\sigma\tau\hat{\tilde{k}}_y) \langle \sigma, \tau | \psi \rangle = \sqrt{2}\tilde{E} \langle -\sigma, \tau | \psi \rangle, \quad \sigma = \pm 1, \tau = \pm 1. \quad (3.32)$$

We now project the states into position space and solve for the \tilde{y} -dependent pseudospinors ϕ , see eq. (3.28). We must distinguish between two cases: energy $\tilde{E} = 0$ and $\tilde{E} \neq 0$.

For $\tilde{E} = 0$, the equations decouple. We solve them using a Gaussian ansatz and find that $\sigma = \tau$. However, the K -valley solution, $\sigma = \tau = +1$, cannot fulfill the boundary condition in eq. (3.29) and must be rejected. Therefore the only $\tilde{E} = 0$ solution is ($\tilde{k}_x \equiv \tilde{k}$)

$$\phi_{\tilde{k},0,-1}(\tilde{y}) = \left(0, \exp\left[-\frac{1}{2}(\tilde{k} + \tilde{y})^2\right] \right)^T. \quad (3.33)$$

¹⁰Note that this σ is not to be confused with any previously introduced σ .

Bizarrely, this solution satisfies the boundary condition *everywhere* as if there was no edge present. This zero-energy level has been the subject of several research papers [77, 81–83] and will not be discussed further in this thesis. We will ultimately consider low-energy transitions where this state is far below the chemical potential and thus inert.

We now return to eq. (3.32) and consider the case $\tilde{E} \neq 0$. We solve and substitute, finding the coupled equations

$$\left(\partial_\xi^2 + \nu + \frac{1}{2}\sigma\tau - \frac{1}{4}\xi^2 \right) \phi_{\sigma, \tilde{k}, \nu, \tau}(\xi) = 0, \quad (3.34)$$

$$\frac{1}{\sqrt{\nu}} \left(\frac{1}{2}\xi + \sigma\tau\partial_\xi \right) \phi_{\sigma, \tilde{k}, \nu, \tau}(\xi) = \phi_{-\sigma, \tilde{k}, \nu, \tau}(\xi), \quad (3.35)$$

where we have defined $\xi = \sqrt{2}(\tilde{k} + \tilde{y})$ and $\nu = \tilde{E}^2 > 0$. For $\sigma = \tau = +1$, eq. (3.34) becomes a well-known equation whose solutions are the so-called *parabolic cylinder functions* $D_\nu(\xi)$ and $D_{-\nu-1}(i\xi)$, of which only the first goes to zero as $\xi \rightarrow +\infty$. We therefore find that $\phi_{+1, \tilde{k}, \nu, +1} = D_\nu(\xi)$ [77, 79, 84, 85]. The other sublattice component, $\sigma = -1$, is found from eq. (3.35) using the relation $(\partial_\xi + \xi/2)D_\nu(\xi) = \nu D_{\nu-1}(\xi)$ [84, 85]. Since σ and τ only enter as the product $\sigma\tau$, interchanging valleys is equivalent to interchanging sublattices. Thus, for $\tau = -1$ (K' -valley), we simply swap $\sigma \leftrightarrow -\sigma$ and find

$$\phi_{\tilde{k}, \nu, +1}(\xi) = \begin{pmatrix} D_\nu(\xi) \\ \sqrt{\nu} D_{\nu-1}(\xi) \end{pmatrix}, \quad \phi_{\tilde{k}, \nu, -1}(\xi) = \begin{pmatrix} \sqrt{\nu} D_{\nu-1}(\xi) \\ D_\nu(\xi) \end{pmatrix}. \quad (3.36)$$

The boundary condition, eq. (3.29), then yields equations for the spectrum:

$$E_\nu^{(\tau)}(\tilde{k}) = \pm\sqrt{\nu}, \quad D_{\nu+(\tau-1)/2}(\sqrt{2}\tilde{k}) = 0. \quad (3.37)$$

Eq. (3.37) can be solved numerically [86]; the resulting spectrum is plotted in fig. 3.9 together with the dispersionless level $\tilde{E} = 0$. Due to the quadratic dependence of ν on \tilde{E} , the spectrum is electron-hole symmetric. At large negative \tilde{k} , the allowed energies $\pm\sqrt{\nu}$ tend to $\pm\sqrt{n}$, n being an integer; the bands asymptotically approach dispersionless *Landau levels* [59, 87] and the functions $D_\nu(\xi)$ approach the energy eigenfunctions of the unconfined quantum harmonic oscillator [85, 88], centered at $\tilde{y} = -\tilde{k}$. These are localized wave functions with zero velocity. In the classical skipping-orbit picture, this corresponds to electronic orbits with centers far from the edge (fig. 3.2). As \tilde{k} increases, the orbit center moves toward and over the edge, confining

3.4. THE ELECTRONIC SUBSYSTEM

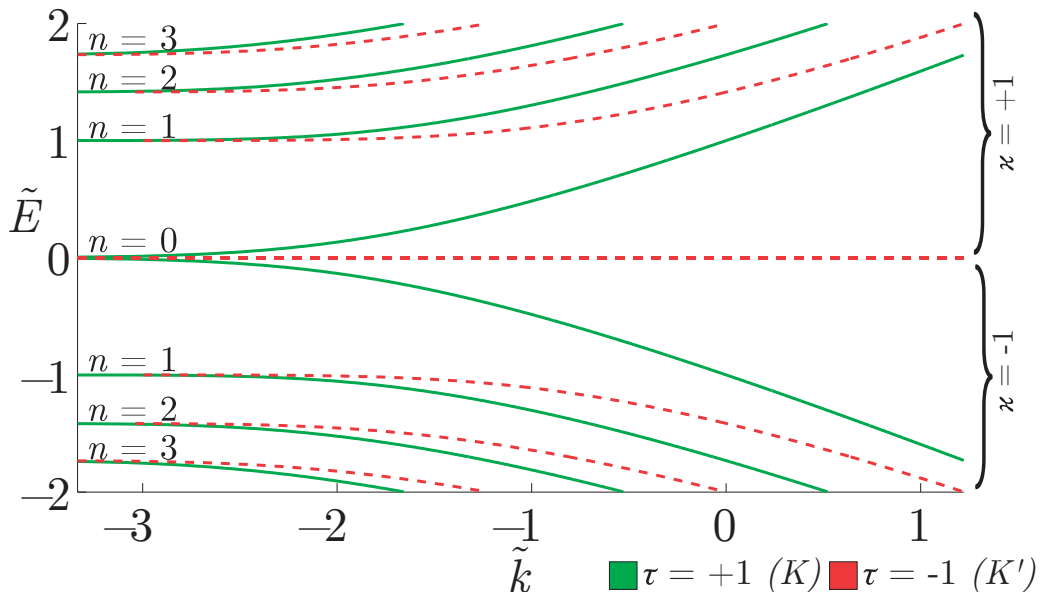


Figure 3.9: The scaled electronic spectrum for the considered system (energy in E_B , wave vectors in $1/l_B$), with a zigzag edge and a perpendicular magnetic field. The solid green (dashed red) lines are states in the K -valley, $\tau = +1$ (K' -valley, $\tau = -1$). The energy bands are labeled according to their corresponding bulk Landau level, i.e., $n = 0, 1, 2, \dots$ counted from $\tilde{E} = 0$, and $\nu = +1$ ($\nu = -1$) for positive-energy (negative-energy) levels. The K' -valley has a dispersionless energy level at precisely $\tilde{E} = 0$ instead of having any 0th energy band. (Note that we have neglected spin.)

the wave functions to within a few magnetic lengths of the edge (fig. 3.10). The energy levels simultaneously become dispersive bands with a finite velocity along the edge. We therefore see a clear correspondence between the quantum mechanical and skipping-orbit results. The bulk Landau levels are commonly labeled by an integer n , starting from $n = 0$ at zero energy. We will use the index n to label the energy band whose energy approaches the energy of Landau level n as $\tilde{k} \rightarrow -\infty$. Another index, $\nu = \pm 1$, will denote positive (+) and negative (-) energies (with respect to the charge neutrality point).

The energy spacing between the bands is on the order of $E_B \approx 26 \cdot \sqrt{B[T]}$ meV, corresponding to a temperature of $421 \cdot \sqrt{B[T]}$ K, while Zeeman splitting corresponds [79] to $0.67 \cdot B[T]$ K. Therefore, we may consider the bands as distinct and spin degenerate as long as the temperature T satisfies $0.67 \text{ K} \cdot B[T] \ll T \ll 421 \text{ K} \cdot \sqrt{B[T]}$.

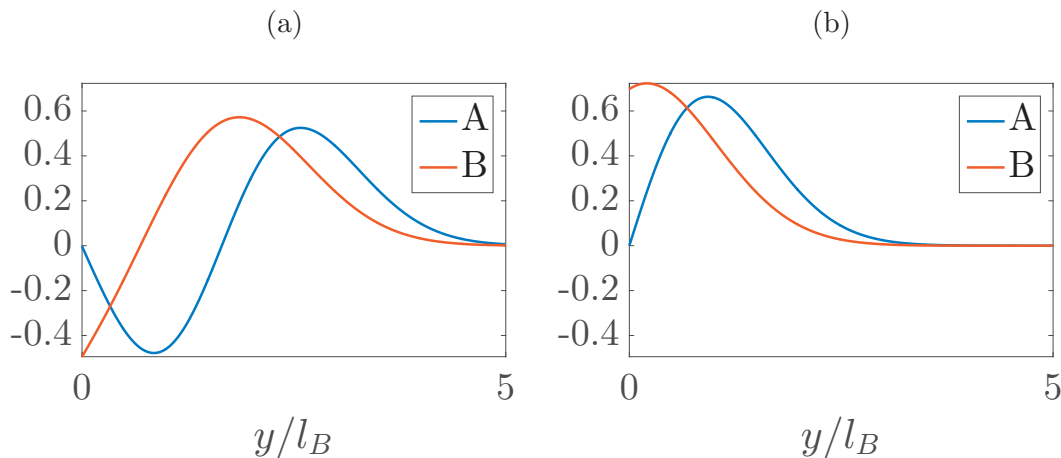


Figure 3.10: The A - and B -components of the (normalized) K -valley pseudospinor component, see eq. (3.36), where $\nu = (1 + \sqrt{2})/2$. The wave vectors are $kl_B = -1.29$ (a) and $kl_B = 0.36$ (b).

3.5 Electron-Strain Interaction

Strain in a graphene sheet causes deformations of the lattice which affect the electrons. The electron-strain interaction in graphene (presented below) was first calculated by Suzuura and Ando in 2001 when considering strain effects in carbon nanotubes [89].

The most straight-forward effect is a change in the size of the unit cell. The trace of the strain tensor, $u_{xx} + u_{yy}$, corresponds to a pure compression or dilation of the sheet, and thus of the individual unit cells. Changing the size of the unit cell changes the carrier concentration and thereby causes an energy shift. We model this effect by introducing a scalar potential proportional to the change in area due to deformation,

$$H_{\text{int},AA}^{(\tau)} = H_{\text{int},BB}^{(\tau)} = g_1(u_{xx} + u_{yy}). \quad (3.38)$$

The coupling constant has been estimated to $g_1 \approx 20$ eV [89]. The diagonal Hamiltonian matrix given by the above expression is invariant under the unitary transformation defined by eq. (3.23) and will be included in the full interaction Hamiltonian below.

In addition to changing the size of the unit cell, sheet deformations can also alter the shape of the lattice so that the distance between nearest-neighbor atoms changes. This is usually modeled by assuming that the deformation simply changes the hopping energy between the atoms. In subsec-

3.5. ELECTRON-STRAIN INTERACTION

tion 3.4.1 we assumed that the hopping energies to different nearest neighbors were equal, $t_1 = t_2 = t_3 \equiv t$. If we instead assume that the hopping energies differ by a small amount, $t_n = t + \delta t_n$, $\delta t_n \ll t$, and neglect terms $\propto \delta t_n \mathbf{k}$ since both $|\mathbf{k}|$ and δt_n are assumed small¹¹, an additional term appears in the off-diagonal elements:

$$H_{\text{int},BA}^{(\tau)} = \frac{1}{2} \left(\tau(\delta t_2 + \delta t_3 - 2\delta t_1) + i\sqrt{3}(\delta t_2 - \delta t_3) \right). \quad (3.39)$$

In the above, we have already included the effects of the unitary transformation defined by eq. (3.23). In order to express the changes in hopping energy δt_n in terms of strain, we assume that

$$\delta t_n = -t\beta \frac{\delta \mathbf{R}_n \cdot (\mathbf{u}_{B,n} - \mathbf{u}_A)}{(a/\sqrt{3})^2}, \quad (3.40)$$

where \mathbf{u}_A is the displacement of an A -atom and $\mathbf{u}_{B,n}$ is the displacement of its nearest-neighbor B -atom ($n = 1, 2, 3$). The hopping energy t and interatomic bond length $a/\sqrt{3}$ (a being the lattice constant) scales the energy and lengths, and $\beta \approx 2$ is a Grüneisen parameter [89]. In the theory of elasticity, we treat graphene as a continuous medium, not as a discrete lattice, so we take the vector difference in eq. (3.40) to the continuous limit and get

$$\mathbf{u}_{B,n} - \mathbf{u}_A \rightarrow \kappa(\delta \mathbf{R}_n \cdot \nabla)\mathbf{u}(\mathbf{r}), \quad (3.41)$$

where κ is a proportionality constant relating the discrete lattice to the continuous limit, and $\mathbf{u}(\mathbf{r})$ is the continuous 2D displacement field as defined in eq. (2.1). The differentiations on the components of the displacement field lead to the introduction of the strain tensor as defined in eq. (2.1) and we arrive at

$$H_{\text{int},BA}^{(\tau)} = g_2 (-\tau(u_{xx} - u_{yy}) + 2iu_{xy}), \quad (3.42)$$

where we defined the coupling constant $g_2 \equiv \hbar v_F \sqrt{3} \beta \kappa / [2a] \approx 2$ eV [89]. Comparing eq. (3.42) with eq. (3.24), we see that the strain interaction enters into the full electronic Hamiltonian similarly to a magnetic vector potential, $\mathbf{k} \rightarrow \mathbf{k} + \mathbf{A}^{(\tau)}$. For this reason, the interaction elements given by eq. (3.42) are

¹¹The fact that the interaction is an approximation to zeroth order in \mathbf{k} means that, in this model, strain cannot change the Fermi velocity.

sometimes referred to as a *strain-induced pseudomagnetic field* [90]. However, unlike a real magnetic field, strain does not break time-reversal symmetry¹².

We now include both the off-diagonal “pseudomagnetic field” of eq. (3.42) and the scalar deformation potential of eq. (3.38) in an electron-strain interaction Hamiltonian which we write using sublattice-space Pauli matrices as

$$\hat{H}_{\text{int}} = \sum_{\tau=\pm 1} \iint \hat{\psi}^\dagger(x, y) \mathbf{H}_{\text{int}}^{(\tau)}[\mathbf{u}(x, y; t)] \hat{\psi}(x, y) dx dy, \quad (3.43)$$

$$\mathbf{H}_{\text{int}}^{(\tau)}[\mathbf{u}(x, y; t)] = g_1(u_{xx} + u_{yy})\mathbf{I} + g_2(-\tau(u_{xx} - u_{yy})\boldsymbol{\sigma}_x + 2u_{xy}\boldsymbol{\sigma}_y).$$

Here, we have explicitly written the dependence of the interaction Hamiltonian on the displacement field $\mathbf{u}(x, y; t)$. In the case of a quantized acoustic field, the strain-tensor components are operators, $u_{ij} \rightarrow \hat{u}_{ij}$, defined in terms of their associated displacement-field operator $\hat{\mathbf{u}}(x, y)$ (see subsection 3.3.2).

3.6 Summary of Papers II & III

In both papers, we consider a zigzag edge of a graphene sheet in a perpendicular magnetic field and investigate the interaction between acoustic Rayleigh edge waves and electronic edge states. To begin with, we consider a *classical* acoustic field of Rayleigh waves $\mathbf{u}_{R,q}(x, y; t)$, eq. (3.7), and insert it into \hat{H}_{int} . The magnetic field enters via the minimal coupling $\hat{p}_x \rightarrow \hat{p}_x + eB\hat{y}$. Applying a gate voltage V_G to set the chemical potential $\mu = eV_G$, the full electronic Hamiltonian is [see eqs. (3.26) and (3.43)]

$$\hat{H} = \hat{H}_{\text{el}} + \hat{H}_{\text{int}}[\mathbf{u}_{R,q}(x, y; t)] - eV_G \quad (3.44)$$

which is supplemented by the boundary condition in eq. (3.29). We diagonalize \hat{H}_{el} using the wave functions described in subsection 3.4.3. However, due to the interaction with Rayleigh waves, the electronic edge states are not eigenstates of the full Hamiltonian and therefore couple to each other through the interaction; the interaction causes electronic transitions. Since acoustic fields are smooth on the scale of the lattice spacing¹³, they cannot mix valleys so we only have intravalley transitions. We specify an electronic state

¹²Since the wave vectors of the K - and K' -points are related by a sign reversal, the two valleys are related by time reversal [59]. The preservation of time-reversal symmetry is guaranteed by the interplay of the τ in eq. (3.42) and those in eq. (3.24).

¹³ $|\mathbf{K} - \mathbf{K}'| \sim a^{-1} \gg q$.

3.6. SUMMARY OF PAPERS II & III

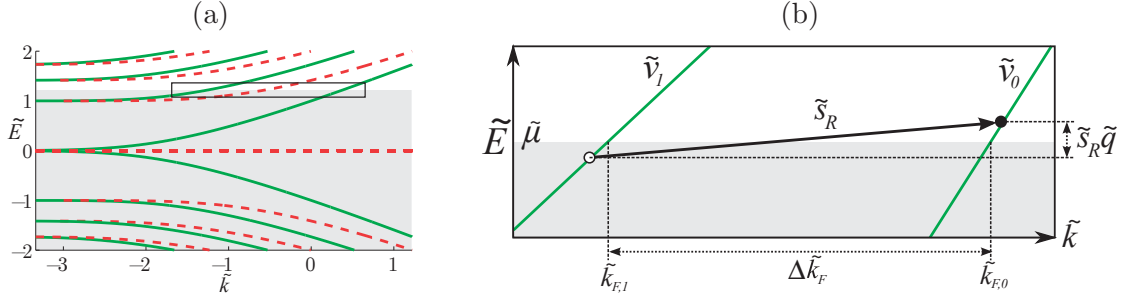


Figure 3.11: (a) The electronic spectrum with a shifted chemical potential (top of grey region) due to an applied gate voltage. A transition is possible where two bands in the same valley cross the chemical potential (black rectangle). (b) A close-up of the transition region (the black rectangle). On this energy scale, we may approximate the bands as *linear* with velocities \tilde{v}_1 and \tilde{v}_0 . Transitions (arrow) induced by the acoustic field create electron (\bullet) and hole (\circ) excitations near the Fermi crossing points $\tilde{k}_{F,1}$ and $\tilde{k}_{F,1}$. The acoustic wave vector must roughly match $\Delta\tilde{k}_F$.

j by τ_j , \tilde{k}_j , n_j , and \varkappa_j ; see fig. 3.9. The matrix element¹⁴ for an electronic transition $i \rightarrow f$ is

$$\begin{aligned} \langle f | \hat{H}_{\text{int}} [\bar{\mathbf{u}}_{R,q}(\mathbf{r}; t)] | i \rangle &= 2\pi\delta(\Delta\tilde{k} - \tilde{q}) V_{fi}(\tilde{q}) \exp\left(iE_B[\Delta\tilde{E} - \tilde{s}_R|\tilde{q}]t/\hbar\right) \delta_{\tau_i, \tau_j} \\ &+ 2\pi\delta(\Delta\tilde{k} + \tilde{q}) V_{fi}(-\tilde{q}) \exp\left(iE_B[\Delta\tilde{E} + \tilde{s}_R|\tilde{q}]t/\hbar\right) \delta_{\tau_i, \tau_j}, \end{aligned} \quad (3.45)$$

where $\Delta\tilde{k} = \tilde{k}_f - \tilde{k}_i$, $\Delta\tilde{E} \equiv \tilde{E}_f - \tilde{E}_i$, and the scaled sound speed is $\tilde{s}_R \equiv s_R/[\sqrt{2}v_F]$. The first (second) term in eq. (3.45) corresponds to an electronic transition involving absorption (emission) of acoustic energy. The interaction strength is

$$V_{fi}(\tilde{q}) = i\tilde{q}l_B^{-1}Ag_R/2, \quad g_R = F_1g_1 + F_2g_2, \quad (3.46)$$

where F_1 and F_2 (indices suppressed for brevity) are nondimensionalized \tilde{y} -integrals specific to the transition. Explicit expressions can be found in the appendix to paper II.

Since the speed of sound \tilde{s}_R is much lower than typical electronic velocities, the transitions appear almost horizontal in the electronic spectrum (fig. 3.11a). It follows that all transitions are interband, $n_f \neq n_i$, and confined to a narrow range of energies around the chemical potential¹⁵, so typically

¹⁴In paper II, we used the notation $\Lambda_{\tilde{k}_f, \tilde{k}_i}^\tau$ for this matrix element and explicitly extracted the momentum conserving factor.

¹⁵The exception is when \tilde{q} is very large. However, in this case the matrix element will vanish due to the states having very different degrees of localization.

$\varkappa_i = \varkappa_f = \text{sgn}(\mu)$. The interaction is strongest when the acoustic field is at resonance with the electronic states, $\tilde{q} = \Delta\tilde{k}$, $\tilde{s}_R|\tilde{q}| = \Delta\tilde{E}$. Far away from resonance, the matrix element, eq. (3.45), vanishes due to conservation of energy and momentum. We can thus restrict our attention to near-resonant transitions and *linearize* each band around the resonant state (fig. 3.11b). The dimensionless electronic velocity appearing in the linearization around state $j = i, f$, is $\tilde{v}_j = v_j/[\sqrt{2}v_F]$ (cf. \tilde{s}_R above), where v_j is the physical velocity. Additionally, we can approximate all \tilde{y} -dependent factors in eq. (3.46) by their resonant values¹⁶. Then $V_{fi}(\Delta\tilde{k})$ is just an energy specific to each resonance.

An approximate condition for resonant interaction is that the acoustic wave vector $q \sim 1/l_B$. Using eqs. (3.3) and (3.30), we get

$$f_{\text{ac}} = \omega_R(q)/[2\pi] \sim \sqrt{B[T]} \cdot 73 \text{ GHz}. \quad (3.47)$$

3.6.1 Results: Rayleigh Wave Attenuation

In paper II, we investigate the case when the acoustic field has a low amplitude A and electronic excitations relax quickly. The electronic dynamics are then well described by first order perturbation theory during the short time τ_{el} it takes for the electronic system to relax to equilibrium (due to e.g., edge defects, impurities). To be specific, we require that

$$|V_{fi}(\Delta\tilde{k})| \ll \hbar/\tau_{\text{el}}, \quad (3.48)$$

where $i \rightarrow f$ is a resonant transition from a state i below the chemical potential to a state f above it. Motivated by the fast electronic relaxation, we assume electronic equilibrium, and thus only consider the absorption term (first term) in eq. (3.45). We also assume low temperature so that the Fermi distribution function is a step function. We seek the *total* transition rate, not just between the resonant states, but between all near-resonant states in the same bands, i.e., from states close to i to states close to f . We use *Fermi's golden rule* to get the probability of transition per unit time—the “transition rate”—from a single initial state to a continuum of final states, then integrate over the initial states and enforce energy conservation. As already mentioned,

¹⁶In paper II, we did not distinguish between the resonant states and the crossing points of the chemical potential. However, the difference is negligible when considering the interaction strength since $\Delta\tilde{k} \approx \Delta\tilde{k}_F$.

3.6. SUMMARY OF PAPERS II & III

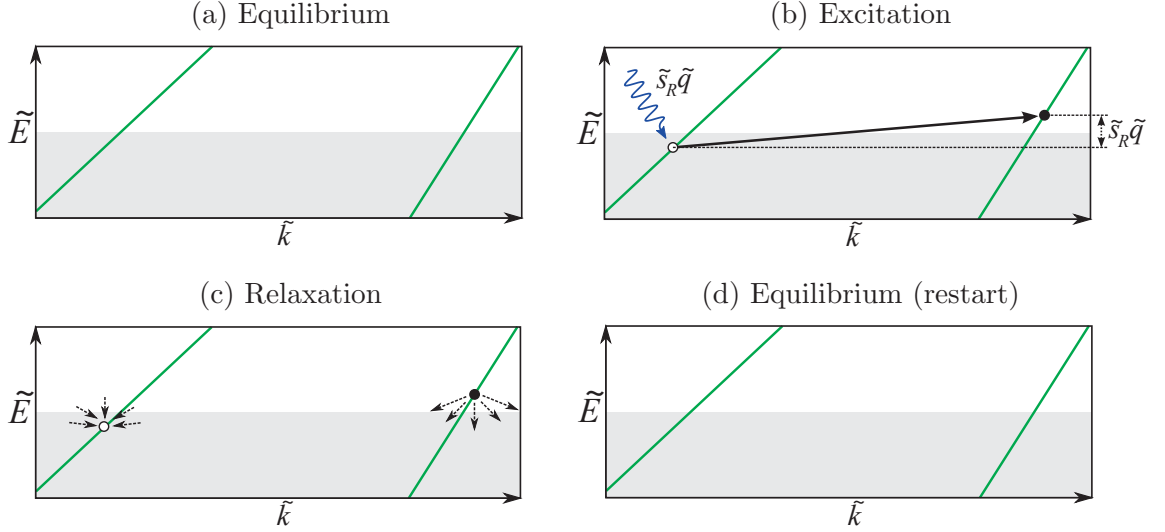


Figure 3.12: (a) The electronic subsystem is at equilibrium. We consider two linearized electronic energy bands near the chemical potential (top of grey region). (b) Interaction with a resonant acoustic Rayleigh wave (blue wiggly arrow) causes an electronic interband transition (black arrow), leaving behind a hole (\circ) in one band and an excited electron (\bullet) in the other. The electronic subsystem has now absorbed the energy $\tilde{s}_R \tilde{q}$ (units E_B) from the acoustic subsystem. (c) The electronic subsystem quickly relaxes to equilibrium. (d) The electronic subsystem is once again in equilibrium; the sequence is repeated anew. Each repetition of this cycle causes the acoustic subsystem to lose energy.

we linearize the spectrum around the resonant states and approximate V_{fi} to its resonant value. We get the transition rate (per length) between two resonant electronic populations in different bands:

$$W_{fi} = \frac{|V_{fi}(\Delta \tilde{k})|^2}{\hbar^2 |v_f - v_i|}. \quad (3.49)$$

The energy for each transition is taken from the acoustic field. Repeated transitions thereby cause an *attenuation* of the Rayleigh edge waves (fig. 3.12). If we multiply the transition rate W_{fi} by the proportion of energy lost in each transition, $\hbar s_R |\Delta k| / E_{ac}$, where

$$E_{ac} = \rho_{gr} \omega_R^2(q) \lim_{L \rightarrow \infty} \frac{1}{L} \int_{-L/2}^{L/2} dx \int_0^\infty dy |\mathbf{u}_{R,q}(x, y; t)|^2 = \frac{\rho_{gr} \omega_R^2(\Delta k) A^2}{2 |N_{ac}|^2 |\Delta k|} \quad (3.50)$$

is the total acoustic energy per length [22] [we used eqs. (3.7) and (3.13)], we

get an expression for the attenuation rate of the acoustic field:

$$\Gamma = \frac{|\Delta k|^2 |N_{\text{ac}}|^2 |g_R|^2}{2\hbar |v_f - v_i| \rho_{\text{gr}} s_R} = \frac{1}{\tau_D}. \quad (3.51)$$

Naturally, there may be other causes of acoustic attenuation; Γ is the attenuation rate due to the specific resonant electronic transition $i \rightarrow f$ and the proximate near-resonant transitions. In terms of the acoustic decay time $\tau_D = 1/\Gamma$, the energy of the acoustic field decays as $\sim \exp(-t/\tau_D)$ ¹⁷.

As an example, we consider the case when the gate voltage V_G positions the chemical potential precisely in the middle of the gap between bulk Landau levels 1 and 2, and resonant Rayleigh edge waves induce transitions from energy band $n_i = 1$ to $n_f = 0$ near the chemical potential¹⁸. At equilibrium, this is the only possible resonance due to the “missing” band in the K' -spectrum (see subsection 3.4.3, fig. 3.9). We find $g_R \approx 1.3$ eV. The electronic velocities v_i can be estimated from the slope of the energy bands in the spectrum (fig. 3.9). We then get $\tau_D \approx 3.4$ ns/ B [T].

We then consider the case when the gate voltage $V_G = -50$ mV and the Rayleigh-wave frequency $f_{\text{ac}} = 165$ GHz are fixed, but the magnetic field B is modulated, and numerically calculate Γ as a function of B . Changing the magnetic field B alters the separation energy E_B between bulk Landau levels¹⁹, causing the levels to move with respect to the chemical potential. E.g., decreasing B causes the energy levels to drop below the chemical potential, thus increasing the number of energy bands crossing it. This effect becomes simplified when considering the scaled energy spectrum (fig. 3.9). Since the shape of the scaled spectrum is independent of the magnetic field, the only effect is a shift in the position of the (scaled) chemical potential $\tilde{\mu} = \mu/E_B \propto 1/\sqrt{B}$. We gradually reduce B , causing the chemical potential $\tilde{\mu}$ to rise through the scaled spectrum. For each value of B , we then calculate Γ due to any and all possible transitions between the electronic bands. The results²⁰ are presented in fig. 3.13; more plots are available in paper II.

¹⁷It should be noted that we did not include a factor 2 for the spin degeneracy. Inclusion of this factor would halve the decay time. Then again, since the energy is quadratic in the amplitude, we can simply reinterpret the figure as the decay time of the amplitude.

¹⁸The wave functions in fig. 3.10 correspond to these states.

¹⁹“ E_1 ” in paper II.

²⁰We did not include the factor 2 for spin degeneracy.

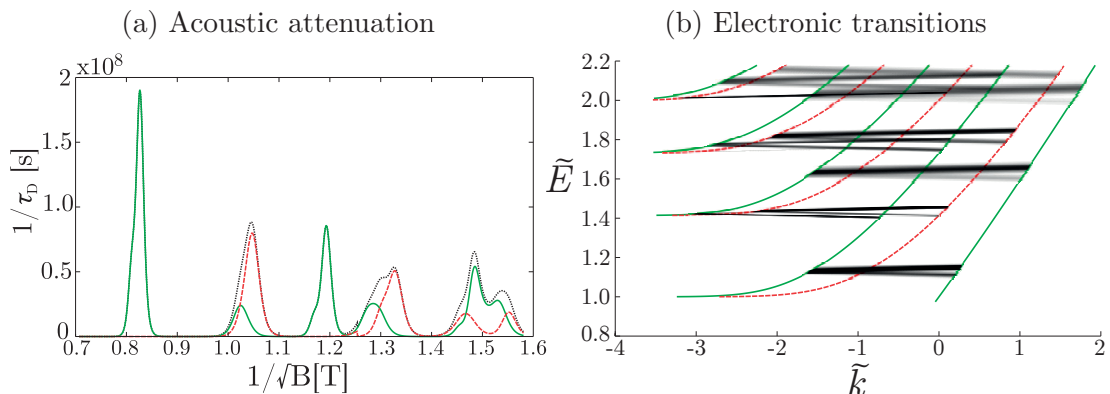


Figure 3.13: The gate voltage $V_G = -50$ mV and the acoustic frequency $f_{ac} = 165$ GHz are fixed, but the magnetic field B is gradually reduced, causing the scaled chemical potential $\tilde{\mu} \propto 1/\sqrt{B}$ and acoustic wave vector $\tilde{q} \propto 1/\sqrt{B}$ to increase. For each value of B , we numerically calculate the acoustic attenuation rate $1/\tau_D$ for all possible electronic transitions and plot $1/\tau_D$ vs $1/\sqrt{B}$ (a) for transitions in both the K - (green) and K' -valleys (red), as well as the summed attenuation rate for both valleys (black, dotted). We also plot the transitions themselves in the scaled spectrum (b), with line opacity proportional to $1/\tau_D$. We used a nonzero temperature $T = 5$ K.

3.6.2 Results: Electroacoustic Solitons

In paper III, we start from a fully quantized Hamiltonian for both the electronic and acoustic subsystems,

$$\hat{H} = \hat{H}_{el} + \hat{H}_{int} - eV_G + \hat{H}_{ac}, \quad (3.52)$$

[see eqs. (3.11) and (3.12)]. We assume that linear perturbation theory (e.g., Fermi’s golden rule) breaks down, i.e., eq. (3.48) is no longer true. Instead, we assume that electronic relaxation is negligible, i.e., τ_{el} is very large compared to all other time scales. This can be achieved by simply increasing the acoustic amplitude and thus $V_{fi}(\Delta\tilde{k})$, making the interaction dynamics much faster than electron relaxation. We then consider the full nonlinear system of equations for near-resonant coupling between the electronic and acoustic subsystems and solve it self-consistently. We find that it admits traveling electroacoustic *soliton* solutions which can move at speeds exceeding that of sound. A soliton, or “solitary wave”, is a wave packet with a *fixed profile*—its shape is constant—moving with constant velocity; for this reason, solitons were originally named “waves of translation”.

For simplicity, we consider the case when the chemical potential is positioned in the middle of the gap between bulk Landau levels 1 and 2 (fig. 3.11).

There are then two electronic bands intersecting the chemical potential in the K -valley, and only one in the K' -valley. Since transitions are interband and intravalley, we only need to consider the K -valley. We linearize the two energy bands $n = 1$ and $n = 0$ ($\varkappa = +1$) near the chemical potential and then reduce our 2D system to an *effective 1D model* for the edge by taking the y -dependent parts of the electronic wave functions as equal for all states in the same resonant population, i.e., we neglect their k -dependence (these functions of y are those depicted in fig. 3.10). Also, note that we will not use scaled quantities (e.g., \tilde{q} , \tilde{x}) in this section²¹.

As an example of the 2D \rightarrow 1D method, let us consider the acoustic subsystem, starting from eq. (3.12). We assume that the acoustic field is a wave packet consisting of near-resonant wave vectors²², $q \approx \pm\Delta k$. We then split the q -integral into two δq -integrals—one where $q = \Delta k + \delta q$, and one where $q = -\Delta k + \delta q$. As an approximation, we take $\omega_R(q) \approx \omega_R(\Delta k)$ in the square root of the prefactor, and $\mathbf{f}_q(y) \approx \mathbf{f}_{\pm\Delta k}(y)$. The phononic creation and annihilation operators now describe two different kinds of phonons, so we introduce a new pair of commuting phononic operators: $\hat{b}_R(\pm\Delta k + \delta q) \equiv \hat{b}_{\pm}(\delta q)$. If we now exploit the fact that $\mathbf{f}_{\Delta k}^*(y) = \mathbf{f}_{-\Delta k}(y)$, we may reorder terms so that

$$\hat{\mathbf{u}}_R(\mathbf{r}) = \sqrt{\frac{\hbar}{2\rho_{\text{gr}}\omega_R(\Delta k)}} N_{\text{ac}} \sqrt{|\Delta k|} \left[\mathbf{f}_{\Delta k}(y) e^{i\Delta k x} \left(\hat{u}_+(x) + \hat{u}_-^\dagger(x) \right) + \mathbf{f}_{\Delta k}^*(y) e^{-i\Delta k x} \left(\hat{u}_+^\dagger(x) + \hat{u}_-(x) \right) \right], \quad (3.53)$$

where we have defined the 1D operators

$$\hat{u}_{\pm}(x) = \int \frac{d\delta q}{2\pi} e^{i\delta q x} \hat{b}_{\pm}(\delta q), \quad \left[\hat{u}_{\pm}(x), \hat{u}_{\pm}^\dagger(x') \right] = \delta(x - x'); \quad (3.54)$$

all nonequivalent commutators being zero.

As mentioned in subsection 3.3.3, the full acoustic Hamiltonian in eq. (3.11) can be diagonalized by the eigenwave basis. For a field of Rayleigh waves, see eq. (3.12), we get (up to an additive constant energy)

$$\hat{H}_{\text{ac}} = \int \frac{dq}{2\pi} \hbar \omega_R(q) \hat{b}_R^\dagger(q) \hat{b}_R(q), \quad (3.55)$$

²¹And note especially that while \tilde{v} in paper II represented a nondimensionalized velocity, in the notation of paper III it instead represents v in a moving reference frame.

²²Actually, in paper III, we first considered the distance between Fermi crossing points, Δk_F , and then made a transformation to the true resonant states.

3.6. SUMMARY OF PAPERS II & III

where the number of Rayleigh-mode phonons with wave vector q are counted by the number operator $\hat{b}_R^\dagger(q)\hat{b}_R(q)$. We split this integral in the same way as in the derivation of eq. (3.53), get

$$\hat{H}_{ac} = \hbar s_R \int (\Delta k + \delta q) \hat{b}_+^\dagger(\delta q) \hat{b}_+(\delta q) + (\Delta k - \delta q) \hat{b}_-^\dagger(\delta q) \hat{b}_-(\delta q) \frac{d\delta q}{2\pi}, \quad (3.56)$$

and then use eq. (3.54) to write this in terms of the operators $\hat{u}_\pm(x)$. Replacing δq with derivatives $\pm i\partial_x$, we get

$$\hat{H}_{ac} = \hbar s_R \int \hat{u}_+^\dagger(x) (\Delta k - i\partial_x) \hat{u}_+(x) + \hat{u}_-^\dagger(x) (\Delta k + i\partial_x) \hat{u}_-(x) dx \quad (3.57)$$

which is a 1D Hamiltonian with position-space operators. The electronic subsystem and the interaction Hamiltonian can be reduced to 1D in a similar way (see paper III). A constant, Λ , describing the strength of the interaction then appears in the 1D interaction Hamiltonian²³; it is related to the acoustic attenuation rate Γ of this resonance through $\Lambda^2 = |v_0 - v_1|\Gamma$, see eq. (3.51). We then get an effective 1D model for resonant Rayleigh edge waves and electronic edge states, yielding the system of equations

$$\begin{aligned} i\hbar(\partial_t + v_0\partial_x)\hat{\psi}_0 &= -i\hbar\Lambda[\hat{u}_+ + \hat{u}_-^\dagger]\hat{\psi}_1, \\ i\hbar(\partial_t + v_1\partial_x)\hat{\psi}_1 &= +i\hbar\Lambda[\hat{u}_+^\dagger + \hat{u}_-]\hat{\psi}_0, \\ i\hbar([\partial_t + is_R\Delta k] + s_R\partial_x)\hat{u}_+ &= +i\hbar\Lambda\hat{\psi}_1^\dagger\hat{\psi}_0, \\ i\hbar([\partial_t - is_R\Delta k] - s_R\partial_x)\hat{u}_-^\dagger &= -i\hbar\Lambda\hat{\psi}_1^\dagger\hat{\psi}_0, \end{aligned} \quad (3.58)$$

which we solve self-consistently. At one point, we replace the quantized acoustic field with a classical field. The motivation for this is that a large amplitude corresponds to a huge number of phonons. In this case, acting on the state with an operator $\hat{b}_R^{(\dagger)}(q)$ to add or subtract *one* phonon has a negligible effect on the state, but the factor which emerges when the operator acts on the state is huge, being proportional to the square root of the number of phonons. We may therefore replace the operator with this number, thereby neglecting its effect on the state. Eventually, we arrive at a family of self-consistent solutions for the full set of equations.

The solutions for the acoustic field are traveling hyperbolic-secant profiles modulated by the resonance frequency. We label them by the parameter T ,

²³Not the same as the quantity $\Lambda_{\tilde{k}_f, \tilde{k}_i}^\tau$ in paper II.

which we interpret as the duration of an acoustic pulse. We have

$$\mathbf{u}_T(\mathbf{r}; t) = \frac{\lambda}{2\pi^2} \left(\frac{\hbar v_{\text{eff}} \Delta k}{g_R} \right) \left(\frac{\lambda}{L} \right) \text{sech} \left(\frac{x - vt}{L} \right) \times \\ \times \begin{pmatrix} [e^{-\lambda_l |\Delta k| y} - C_x e^{-\lambda_l |\Delta k| y}] \cos [\Delta k x - \omega_R(\Delta k) t] \\ [-\lambda_l e^{-\lambda_l |\Delta k| y} + C_y e^{-\lambda_l |\Delta k| y}] \sin [\Delta k x - \omega_R(\Delta k) t] \end{pmatrix}, \quad (3.59)$$

where $v_{\text{eff}} = \sqrt{(v_0 - v)(v_1 - v)}$, $g_R \approx 1.3 \text{ eV}$, λ is the acoustic wavelength, $L = v \cdot T$ is the soliton width, and the soliton velocity v is given by

$$v = \frac{s_R}{1 - \frac{1}{2}\Gamma T}. \quad (3.60)$$

The pulse duration T couples the velocity, amplitude and width of the profile, and we find that increasing the amplitude reduces the velocity, and vice versa (see fig. 3.14). It is found that the speed of these solitons can significantly exceed that of regular Rayleigh edge waves. For the solitons to exist, the pulse duration T must satisfy

$$1/f_{\text{ac}} \ll T \ll \tau_{\text{el}}. \quad (3.61)$$

Also, we must have that $T < 2/\Gamma$ so that eq. (3.60) does not diverge²⁴. The displacement field in eq. (3.59) is inversely proportional to the interaction energy g_R ; this should be understood as follows: if the interaction energy g_R is large, it is possible to form a soliton even at low amplitudes. However, if the interaction is weak, a large amplitude is needed.

The corresponding solutions for the electronic subsystem are in paper III found in terms of the somewhat mysterious quantities $\gamma_i = \boldsymbol{\psi}^\dagger \boldsymbol{\sigma}_i \boldsymbol{\psi}$, where $i = 1, 2, 3$ ($\boldsymbol{\sigma}_i$ are the Pauli matrices in electronic-band space). However, these quantities can be given an intuitive physical interpretation²⁵.

²⁴Another restriction is that T must be such that the soliton velocity is less than the electronic velocities, $v < v_1, v_0$, otherwise v_{eff} becomes imaginary. However, this restriction only amounts to a small correction to the one already mentioned: $T < 2/\Gamma[1 - (s_R/v_1)]$ (since $v_1 < v_0$).

²⁵A vigilant reader familiar with paper III might notice that I am pedagogically hiding a few details, e.g., the wave functions $\boldsymbol{\psi}$ in γ_i are actually scaled and transformed. Additionally, there is a set of γ_i for every energy ϵ (measured with respect to the resonant state in each band) and asymptotic solution \varkappa . However, these details do not invalidate the interpretation of the γ s. To be clear, in the notation of paper III, fig. 3.15 uses $\epsilon = -\hbar\omega_r/4$ and $\varkappa = 1$.

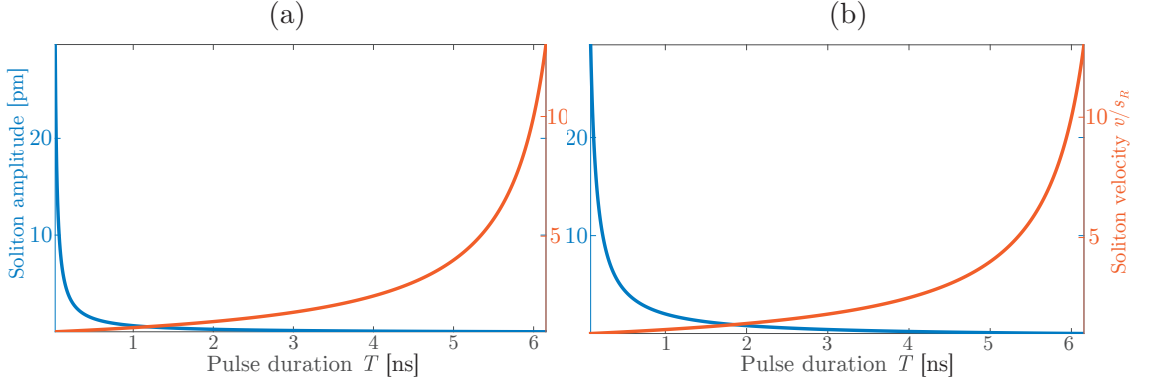


Figure 3.14: The soliton amplitude (blue) and scaled velocity v/s_R (red) plotted against the pulse duration T for (a) $B = 1$ T with $f_{ac} = 125$ GHz and for (b) $B = 10$ T with $f_{ac} = 400$ GHz.

- **Interband coupling:** The quantity $\gamma_1 = \psi_0^* \psi_1 + \psi_1^* \psi_0$ describes the amount of acoustically induced coupling between the resonant electronic populations in bands 0 and 1.
- **Transition asymmetry:** The quantity $\gamma_2 = i(\psi_1^* \psi_0 - \psi_0^* \psi_1)$ describes the asymmetry between transitions from band 0 to 1 and transitions from band 1 to 0 —the net amount of transitions to one band.
- **Population asymmetry:** The quantity $\gamma_3 = \psi_0^* \psi_0 - \psi_1^* \psi_1$ describes the difference in electronic population between bands 0 and 1.

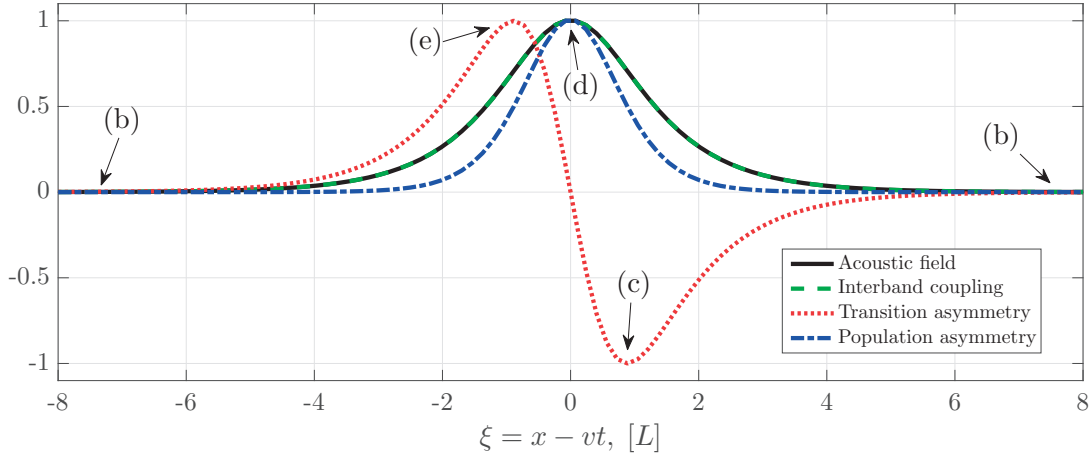
In fig. 3.15, we plot these together with the acoustic field and interpret the results.

3.6.3 Discussion & Outlook

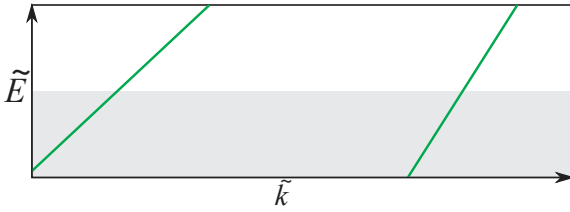
If Rayleigh edge waves can be reliably generated experimentally, it should be possible to test both of the described effects (attenuation and soliton formation) in a time-of-flight experiment. Since the Rayleigh edge waves have 1D wave fronts, they do not attenuate during propagation in the absence of defects [72, 91]; this could potentially make electronically induced attenuation more easily discernible.

It might also be possible to achieve Rayleigh-wave generation *by means of* the studied interaction. If one realized the system in which the chemical potential is different for two electronic bands, the system could begin

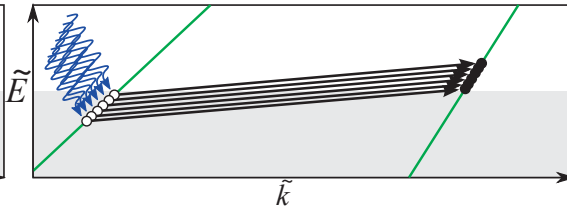
(a) Electroacoustic soliton profile



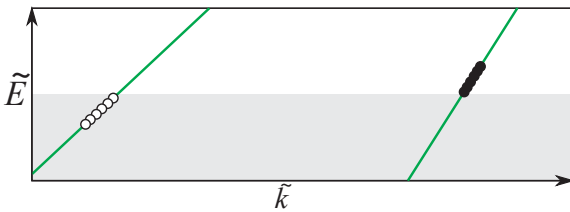
(b) Equilibrium



(c) Excitation



(d) Nonequilibrium



(e) Deexcitation

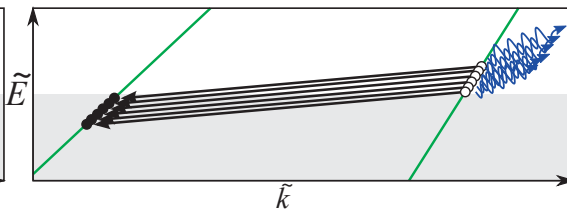


Figure 3.15: (a) The electronic and acoustic components of an electroacoustic soliton; each scaled by their respective maximum value. The abscissa is the position in the rest frame of the soliton, in units of the soliton width $L = vT$. As can be expected, the interband coupling exactly matches the acoustic field responsible for the coupling. Far away from the acoustic field, electrons are at equilibrium (b). In the front half of the traveling soliton, resonant electrons absorb acoustic energy and become excited through interband transitions (c) until the maximal population asymmetry is reached at the soliton center (d). In the back half of the soliton, the electrons deexcite through re-emission of acoustic energy (e) until the electronic equilibrium is restored (b) behind the soliton. The hypersonic velocities attainable by the soliton can thus be explained by some of the acoustic energy continuously being absorbed and re-emitted by the much faster electrons.

3.6. SUMMARY OF PAPERS II & III

relaxation to equilibrium through, e.g., interaction with the acoustic subsystem, thereby generating Rayleigh edge waves and possibly even hypersonic solitons. Soliton generation would then act as a mechanism for electronic relaxation.

We did not discuss acoustic sensors in this chapter, but it is conceivable (though speculative) that the Rayleigh edge waves themselves could be used for “edge mass-sensing”. In a graphene sheet, there are dangling bonds at the edges to which foreign atoms and molecules can attach. It is possible that the presence of alien atoms or molecules on the edge could induce an attenuation of and/or a velocity shift in the edge waves, in a way analogous to the SAW sensors described in chapter 2. This would then make the attached mass detectable.

Theoretically, the work could be continued by also including flexural motion, as flexural edge vibrations are known to exist [92]. Another way forward could be to consider multi-soliton solutions, which are expected from comparison with similar systems [93]. In addition, during the work on paper III, there was an attempt to treat the system with the bosonization technique from 1D quantum theory. This attempt ultimately proved unsuccessful, and bosonization was abandoned in favor of other methods. However, it is well-known that the electronic edge states can be treated using this theory [94]. Therefore, bosonization might be worth revisiting. Possibly, such an approach could facilitate a fully quantum treatment of the acoustic field.

Chapter 4

Nanoelectromechanical Actuation

In chapter 2, I gave an introduction to the field of acoustic sensors. In this chapter, I will describe how the miniaturization of technology is pushing, e.g., sensor technology, toward the quantum realm. This is a motivation for the study of nanoelectromechanical *actuation*, i.e., the generation of mechanical vibrations in a nanoscopic system via electronic means. I give a brief background and then introduce some concepts via example systems. I then summarize papers IV and V which present two different methods of nanomechanical actuation. Before summarizing paper V, I give a short introduction to superconductivity since it is a crucial ingredient in paper V.

4.1 Background: NEMS

An electromechanical system has both electronic and mechanical components. The system considered in chapter 3, a vibrating graphene edge interacting with electronic edge states, is an example of such a system. In chapter 2, we considered only the mechanical component of SAW sensors, but since the SAWs are both created—*actuated*—and read out via the piezoelectric effect (section 2.1), SAW sensors are also electromechanical. More precisely, SAW sensors are *microelectromechanical* systems (MEMS) since they have dimensions on the micrometer scale¹. MEMS devices are ubiqui-

¹One might argue that they are even “nanoscale” given the small thicknesses of, e.g., some guiding layers.

tous in modern technology; examples include medical ultrasound transducers [95], the accelerometers in smartphones and video-game controllers [96], and the airbag deployment systems in cars [97]. Naturally, technological advancements are rapidly shrinking technological components, and we are moving towards the age of *nanoelectromechanical* systems: NEMS [98].

On the face of it, NEMS are simply MEMS made smaller. However, the miniaturization can bring significant benefits, other than just taking up less space. NEMS sensors seem poised to constitute the first wave of commercialized NEMS devices and, unsurprisingly, a small sensor can be made more sensitive than a large one. The principle of a shift in resonance frequency due to adsorbed mass, familiar from chapter 2, also applies in the nanoscopic regime. With a sufficiently small resonator (the vibrating component), the adsorption onto its surface of as little as a single nucleon could be detectable. Current experimental techniques have already allowed for NEMS mass sensors with femto- [99], atto- [100], zepto- [101, 102], and even yoctogram resolution [103]. For comparison: the mass of a proton is about 1.7 yoctograms.

However, changing the length scale also changes the physics involved. As components become smaller, their surface-to-volume ratio increases, leading to considerable surface effects. Furthermore, quantum mechanical effects become relevant. For instance, if you try to build as precise a sensor as possible, sooner or later, you must inevitably grapple with the *de facto* probabilistic nature of quantum mechanics. Furthermore, if two electronic components are sufficiently close² to each other, the electronic wavefunctions significantly extend into both components; we say that the electrons can “tunnel” between them. This effect can cause a short-circuit if not anticipated, and limits how small conventional electronic components can be made. While it may sound like a drawback to be forced back to the drawing board and rethink device design with quantum mechanics in mind, it also holds significant promise. For example, different techniques have been successfully employed to cool mechanical systems to their ground state [104–107] and also to adjust a mechanical state with single-phonon precision [108].

Graphene and carbon nanotubes (see section 3.1) are regarded as promising building blocks for NEMS devices because of their excellent material properties [109]. Graphene is a flexible conducting membrane with high tensile strength and low mass, and carbon nanotubes can be used as mechanical

²Typically a distance on the order of tenths of nanometers or less.

resonators with very high Q -factors³. In a typical setup, a flexible mechanical component, e.g., a graphene ribbon, a carbon nanotube, or a nanoscopic beam, is suspended over a trench so that it is free to vibrate. In the bottom of the trench, one usually places a back gate (a plate electrode) which allows for tuning of the electric potential on the resonator, which can be connected to electrodes and/or put sufficiently close to a component to allow for electronic tunneling.

The SAW sensors in chapter 2 relied on IDTs for the generation and read-out of SAWs. In general, the success of NEMS devices will require reliable ways to generate, control, and detect mechanical vibrations. The study of the actuation of mechanical motion in NEMS is therefore an active research field. The most straightforward way to actuate vibrations is to apply a resonant ac voltage from a back gate [98, 110–113], but there are also suggestions for nonresonant actuation. However, many of these involve an electric current passing through the mechanical resonator [106, 107, 114–117]. The actuation mechanism in paper IV does not belong to any of these categories, but before summarizing that publication, I will devote two sections to the introduction of some basic NEMS building blocks by considering two example systems.

4.2 Example: Resonant Actuation

In this section, we will consider a simple and well-known example system to demonstrate two straightforward methods of NEMS actuation which have carried over from MEMS. I will use this example to introduce some concepts useful to an understanding of the research in papers IV and V.

The system consists of a carbon nanotube (CNT) connected at the ends to two electronic leads and suspended above a gate electrode (fig. 4.1). Since the CNT is of finite extent, its mechanical Hamiltonian diagonalizes not into eigenwaves, but eigenmodes, e.g., bending, twisting, breathing. We assume that only the fundamental vertical bending mode of the CNT is relevant and model the CNT deflection $x(t)$ as a classical mechanical resonator (oscillator) with effective mass m_{eff} and natural frequency ω ,

$$\partial_t^2 x + \frac{\omega}{Q} \partial_t x + \omega^2 x = \frac{F_{\text{el}}}{m_{\text{eff}}}, \quad (4.1)$$

³The Q -factor is the reciprocal of twice the damping ratio, and thus the relative loss of energy per cycle. A high Q -factor means low damping.

4.2. EXAMPLE: RESONANT ACTUATION

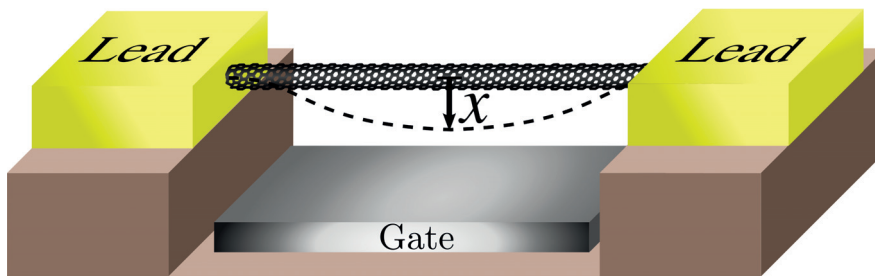


Figure 4.1: A carbon nanotube (CNT) suspended between two leads (yellow) above a gate (grey). The CNT and the gate forms a capacitor with a capacitance which changes with the nanotube deflection x . A voltage with both a dc and an ac component is applied to the gate. (Brown components are insulating.)

where the damping constant ω/Q is written in terms of the resonator Q -factor. CNT resonators are famous for their high Q -factors; $Q \sim 10^4$ can be considered standard, but values $Q \sim 10^6$ have also been achieved [118]. CNT natural frequencies typically range from ~ 10 MHz to ~ 1 GHz [119, 120], with shorter CNTs being stiffer and thus having a higher frequency.

4.2.1 Capacitive Coupling

The resonator is driven by a force F_{el} which is the result of a *capacitive coupling* to the gate. Together, the gate and the CNT constitute a capacitor with capacitance $C(x)$ and capacitive energy $E_C = -C(x)V^2/2$ where V is the voltage drop across the capacitor [121]. We apply an electric potential to the gate so that $V = V_{\text{dc}} + V_{\text{ac}} \sin(\Omega t)$. The capacitance C is a function of the CNT deflection x since it changes the distance between the capacitor “plates” (CNT and gate). Thus, the capacitive driving force $F_{\text{el}} = -\partial_x E_C$ is

$$F_{\text{el}} = \frac{1}{2}(\partial_x C) [V_{\text{dc}}^2 + 2V_{\text{dc}}V_{\text{ac}} \sin(\Omega t)] + O(V_{\text{ac}}^2). \quad (4.2)$$

We assume that the ac voltage V_{ac} is small and keep only first-order terms. We then separate the deflection into a static and a dynamic component, $x(t) = x^{\text{st}} + \Delta x(t)$, and expand the capacitance around x^{st} ,

$$C(x) \approx C(x^{\text{st}}) + C'(x^{\text{st}})\Delta x + \frac{1}{2}C''(x^{\text{st}})\Delta x^2, \quad (4.3)$$

We insert this into eq. (4.1) and equate static and dynamic terms. We find that the static deflection x^{st} , i.e., the shift in the resting position due

to the static potential pulling on the CNT, must be found self-consistently from

$$x_{\text{st}} = -C'(x^{\text{st}})V_{\text{dc}}^2/[2m_{\text{eff}}\omega^2] \quad (4.4)$$

while the dynamic terms can be rearranged to

$$\begin{aligned} \partial_t^2 \Delta x + \frac{\omega}{Q} \partial_t \Delta x + [\tilde{\omega}^2 + \omega_{\text{par}}^2(t)] \Delta x &= \frac{F_{\text{dir}}(t)}{m_{\text{eff}}}, \\ F_{\text{dir}}(t) &= C'(x^{\text{st}})V_{\text{dc}}V_{\text{ac}} \sin(\Omega t), \\ \omega_{\text{par}}^2(t) &= -[C''(x^{\text{st}})V_{\text{dc}}V_{\text{ac}}/m_{\text{eff}}] \sin(\Omega t), \end{aligned} \quad (4.5)$$

where $\tilde{\omega}$ is the *renormalized* mechanical frequency,

$$\tilde{\omega}^2 \equiv \omega^2 \left(1 - \frac{C''(x^{\text{st}})V_{\text{dc}}^2}{m_{\text{eff}}\omega^2} \right). \quad (4.6)$$

4.2.2 Direct Resonance

To begin with, assume that the capacitive force varies negligibly with x , i.e., $C''(x^{\text{st}}) = 0$. Then $\tilde{\omega} = \omega$ and $\omega_{\text{par}} = 0$; there is no renormalization of frequency. However, we have a harmonic driving force $F_{\text{dir}}(t)$, see eq. (4.5). If the driving frequency $\Omega \approx \omega$, we have (direct) resonant driving of the resonator. The bending mode is actuated and starts to oscillate with increasing amplitude, eventually stabilizing at an amplitude limited by the intrinsic mechanical damping ω/Q . Details on resonant driving of a harmonic oscillator can be found in any decent textbook on mechanics, e.g., ref. 122; we will not discuss it further.

4.2.3 Parametric Resonance

Now, instead consider the case when the capacitive force depends on Δx , i.e., $C''(x^{\text{st}}) \neq 0$. The frequency is then renormalized, $\tilde{\omega} \neq \omega$, see eq. (4.6). This renormalization is equivalent to a change in the stiffness $\kappa = m_{\text{eff}}\omega^2$. A decrease (an increase) in stiffness is sometimes called *softening* (*stiffening*).

Inside the [...] -brackets in eq. (4.5), an additional term $\omega_{\text{par}}^2(t)$ enters as a *time dependent* frequency shift, or, equivalently, a time dependent variation of the stiffness. It can be shown that if the driving frequency is approximately *twice* the natural frequency, $\Omega \approx 2\omega$, mechanical oscillations can

4.2. EXAMPLE: RESONANT ACTUATION

be actuated through this term by a phenomenon called *parametric resonance* [123]—“parametric” since the driving is inside a *parameter*: the stiffness constant. When the CNT has already been deflected away from its resting position, it is retroactively stiffened by the capacitive force. Stiffening the already deflected CNT increases its potential energy and results in a greater acceleration toward the resting position (a stronger “spring force”). The term responsible for parametric resonance must change sign every time $\Delta x(t)$ does; otherwise the CNT would instead be *softened*, counteracting the effect. This is why parametric resonance occurs at *twice* the natural frequency.

Unlike direct resonance, parametric resonance only works if the CNT is already vibrating. If not, $\Delta x = 0$ and the parametric-resonance term is identically zero. It is thus an example of a dynamical *instability*: any small deviation⁴ from the exact resting position leads to actuation [122]. In further contrast to direct resonance, parametrically actuated motion is not stabilized by the intrinsic mechanical damping. In order for the resonator to be parametrically excited at all, it is necessary for the parametric driving to overpower the damping. However, once actuated, the amplitude keeps growing without end. Of course, physical amplitudes do not diverge; this is only true of the theoretical model, eq. (4.1). In the considered system, the bending mode of the CNT is a mechanical eigenmode, but the very existence of separate eigenmodes rests on the harmonic approximation. This approximation gets worse as the amplitude increases, and eventually nonlinear effects must be taken into account. A simple and therefore common way to introduce a nonlinearity to the oscillator eq. (4.1) is to add a *Duffing term*, ηx^3 where η is a constant [124]. The inclusion of a Duffing term leads to a saturation of the parametrically actuated amplitude—it eventually reaches a stationary state of self-sustained oscillations (a stable limit cycle [122]).

Actuation through parametric resonance and the resulting stationary oscillations can be studied by, e.g., the Krylov-Bogolyubov averaging method (see ref. 125) or by transforming to a rotating frame and averaging over fast frequencies (see, e.g., ref. 126, or just paper V).

⁴The “small deviation” can simply be the unavoidable result of thermal fluctuations.

4.3 Example: The Shuttle Instability

Here, we will consider an example system which is not quite as well-studied as that in section 4.2. Once again, the purpose is to introduce the reader to some concepts and models which will be of use in understanding papers IV and V. We will model the mechanical subsystem classically but the electronic subsystem quantum mechanically, i.e., a *semiclassical* approach.

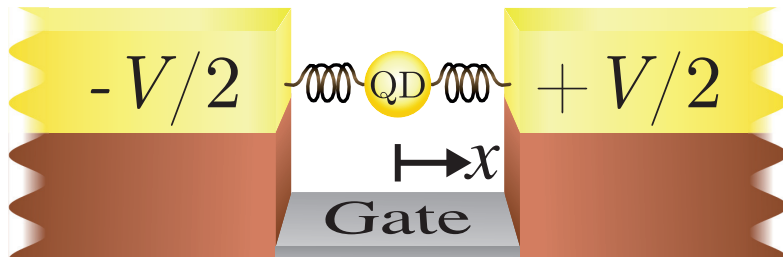


Figure 4.2: A schematic depiction of a nanoelectromechanical shuttle system. A metallic grain (yellow sphere), electronically modeled as a quantum dot (QD), is placed between two leads (yellow blocks) with voltage bias V . Springs allow the QD position x to oscillate. A gate electrode (grey) allows for tuning of the QD energies. (Brown components are insulating.)

We consider the system in fig. 4.2, noting that the picture is merely schematic—there are (so far) no actual mesoscopic springs like those depicted in the figure. However, while the depiction is chosen because of its clarity, the actual model has practical applicability. This system was originally proposed to explain features of silver coated DNA strands [114]. The springs were supposed to model some mechanical features of the DNA strands⁵ and the metallic grain in the middle was a simplified model for the electronic properties of the metal coating. Actually, it remains an elegant example of how a real-world object can be simplified and modeled theoretically. Subsequently, nanoelectromechanical shuttles have been realized in a number of ways, e.g., using lithographic techniques to create a laterally oscillating single-clamped beam with an isolated “grain” at the free end [127], as well as trapping a C60 molecule in a van-der-Waals potential between two leads [128]. For a review, see ref. 129. Here, our main purpose is to introduce NEMS concepts.

The springs allow the grain to perform lateral oscillations between the two leads. The lateral position of the grain is modeled as a classical mechanical resonator, see eq. (4.1), with an electrostatic force $F_{\text{el}} \approx -\alpha qV$ ($\alpha > 0$ is a

⁵And do not double helices somewhat resemble springs?

constant). This force is due to an electrical field originating in an applied charge bias V between the leads (see fig. 4.2). The mechanical resonator is thus coupled to the grain charge q . This brings us to the electronic subsystem of the grain, which we will treat as a *quantum dot*.

4.3.1 A Quantum Dot

Space is (at least) 3D, a *plane* is 2D, a *line* is 1D, and a *dot* is 0D—zero-dimensional. If a piece of material is sufficiently small, the spatial confinement of, e.g., electrons results in clearly separated energy levels; one can then ignore the internal spatial degrees of freedom and treat it as a *quantum dot* (QD), a zero-dimensional quantum system, sometimes likened to an “artificial atom” because of its discrete spectrum [130].

A model Hamiltonian for a QD is

$$\hat{H}_{\text{QD}} = \sum_j E_j \hat{d}_j^\dagger \hat{d}_j. \quad (4.7)$$

where \hat{d}_j^\dagger is the fermionic creation operator for an electron on the QD with energy E_j ; thus $\hat{d}_j^\dagger \hat{d}_j = \hat{n}_j$ is the corresponding number operator, with eigenvalues $n_j = 0, 1$; each QD energy level is either empty or occupied by an electron. If the separation between QD energy levels is much larger than all other relevant energies, particularly the voltage bias eV and the lead temperature $k_B T$, the QD can be tuned by a gate voltage so that all but a single energy level are rendered inert⁶ and we arrive at a *single-electron* QD, with

$$\hat{H}_{\text{QD}} = E_1 \hat{d}^\dagger \hat{d}. \quad (4.8)$$

The energy E_1 should contain both the QD energy level \mathcal{E}_1 and the electrostatic energy⁷ associated with placing an electron on the QD. The QD energies can be tuned by a gate voltage. As for the electrostatic energy, let us assume that the the QD is charge neutral when $n = 0$ and call $|0\rangle$ the “charge neutral” state, in contrast to the occupied state $|1\rangle = \hat{d}^\dagger |0\rangle$, which has charge $q = -e$. Then $E_1 = \mathcal{E}_1 + e^2/C(x)$.

If eq. (4.8) was the full story, charge would be conserved and there would not be much of an electronic system at all. However, we assume that the

⁶We are completely ignoring spin in this example.

⁷This energy depends on x , which is the origin of the electrostatic force F_{el} . However, we will neglect the x -dependence in the energy when considering the electron dynamics.

distance between the QD and the two leads is small enough for electrons to be able to *tunnel* between them.

4.3.2 Tunneling Coupling

Quantum mechanically, an electron has some finite probability of being found in a classically forbidden region. If the QD (grain) is sufficiently close to a lead, the wavefunctions which describe electrons in the lead and those that describe electrons on the QD overlap. If an electron is prepared in a state where it is definitely on the QD, its wavefunction quickly delocalizes so that a subsequent measurement has some finite probability of finding it inside the leads⁸. One then says that the electron has “tunneled” to the leads.

Electron tunneling between the QD and the leads can be modeled by the tunneling Hamiltonian

$$\hat{H}_T = \sum_{\mathbf{k}} \sum_{l=L,R} T_{l,\mathbf{k}}(x) \hat{c}_{l,\mathbf{k}}^\dagger \hat{d} + T_{l,\mathbf{k}}^*(x) \hat{d}^\dagger \hat{c}_{l,\mathbf{k}} \quad (4.9)$$

where $\hat{c}_{l,\mathbf{k}}^\dagger$ creates an electron with wave vector \mathbf{k} in lead l . The first (second) term thus represents tunneling from (to) the QD. The tunneling matrix elements $T_{l,\mathbf{k}}(x)$ depend on the grain position x since it is easier for electrons to tunnel shorter distances than longer ones because more of the electronic wavefunctions overlap. Starting from the Schrödinger equation and considering a plane-wave electronic wavefunction with energy E incident on a potential barrier of height $U > E$, one can find that the transmitted component of the wavefunction decays $\sim \exp(-x/[2\lambda_E])$ where $2\lambda_E = \hbar/\sqrt{2m|E-U|}$ (the factor “2” is for later convenience). This is a very simple model, but it motivates us to assume that the tunneling matrix elements have an exponential dependence on distance,

$$T_{L,\mathbf{k}}(x) = T \exp(-x/[2\lambda]), \quad T_{R,\mathbf{k}}(x) = T \exp(x/[2\lambda]). \quad (4.10)$$

Here, λ is an *effective tunneling length* which we assume equal for tunneling to both leads. The effective tunneling length should be determined experimentally; typically $\lambda \sim 1 \text{ \AA}$. Note that we have assumed that λ is independent

⁸Or rather, finding one less electron on the QD and one additional electron in the leads. They are, after all, indistinguishable particles. However, consistently talking that way rarely increases clarity.

4.3. EXAMPLE: THE SHUTTLE INSTABILITY

of energy; this is reasonable since the finite range of energies we consider are likely much smaller⁹ than $|E - U|$, the work function of the leads. Further, we have assumed that $T_{L,\mathbf{k}}(0) = T_{R,\mathbf{k}}(0) \equiv T$.

Tunneling thus allows the electric charge of the QD to vary by coupling it to the leads, which we are yet to describe. Whereas the electronic subsystem of the grain—the QD—was simple to model due to its small number of degrees of freedom, the leads are (roughly speaking) simple to model because of the *opposite* reason: their large number of degrees of freedom.

4.3.3 Electron Reservoirs

The electronic leads are considered as electron reservoirs with a large number of electronic states. A Hamiltonian for the reservoirs is

$$\hat{H}_{\text{leads}} = \hat{H}_L + \hat{H}_R, \quad \hat{H}_l = \sum_{\mathbf{k}} \epsilon_{l,\mathbf{k}} \hat{c}_{l,\mathbf{k}}^\dagger \hat{c}_{l,\mathbf{k}} = \int d\epsilon_l \nu(\epsilon_l) \epsilon_l \hat{c}_l^\dagger(\epsilon_l) \hat{c}_l(\epsilon_l). \quad (4.11)$$

The QD was assumed to have clearly separated energy levels and coherent dynamics (we made no mention of relaxation) resolved on the single-electron level. The reservoirs on the other hand, are assumed to have a large density of states $\nu(\epsilon_l)$ (often assumed constant) and a huge number of electrons which are constantly scattering. This way, the addition or removal of a single electron has a negligible effect on the state of a reservoir. Inside reservoir l , whatever excitation is created is rapidly erased by scattering and the reservoir relaxes to thermal equilibrium wherein its density operator is

$$\hat{\rho}_l = \frac{1}{Z_l} \exp\left(-\frac{\hat{H}_l - \mu_l}{k_B T_l}\right) \quad (4.12)$$

where T_l is the temperature and the partition function Z_l ensures $\text{Tr}[\hat{\rho}_l] = 1$. Here, we assume that $T_L = T_R \equiv T$. The bias voltage V between the leads enter into eq. (4.12) as shifted chemical potentials, $\mu_l \rightarrow \mu_l \pm eV/2$. The equilibrium density operator and anticommutation of the fermionic operators lead directly to Fermi-Dirac statistics.

⁹Assuming $\lambda = 1 \text{ \AA} = \hbar/\sqrt{2m|E - U|}$ where m is the electron mass, we get $|E - U| \approx 3.8 \text{ eV} \sim 44\,000 \text{ K}$, which is huge.

4.3.4 Electronic Rate Equation

From the quantized electronic Hamiltonian $\hat{H} = \hat{H}_{\text{QD}} + \hat{H}_T + \hat{H}_{\text{leads}}$, it is possible to derive an equation for the probability $P_1(t)$ for the QD to be occupied. This involves considering the reservoir-QD coupling to second order, neglecting quantum correlations between the reservoirs and the QD, assuming that the reservoirs thermalize on a short time scale, and any other approximations that may have slipped the author's mind for the moment. In the supplemental material for paper IV, we perform this procedure explicitly. Here, we will instead emphasize that such *rate equations*¹⁰ can be written down immediately from physical arguments.

Consider the time derivative of the occupation probability, $\partial_t P_1$. With probability P_1 , the QD is occupied, and P_1 can decrease through electron tunneling to either lead l . The electron tunneling rates $\Gamma_l(x)$ are found from the tunneling matrix elements $T_l(x)$ using Fermi's golden rule, $\Gamma_l(x) = 2\pi|T_l(x)|^2/\hbar$. In addition, there must be an empty state to which the electron can tunnel. The probability of this is $[1 - f_{F,l}(E_1)]$, where $f_{F,l}(E_1)$ is the Fermi function for lead l . Analogously, P_1 can increase by tunneling given that the QD is charge neutral (probability P_0) and that there is an available electron in a lead [probability $f_{F,l}(E_1)$]. We thus find

$$\partial_t P_1 = \sum_{l=L,R} \Gamma_l(x) \{-P_1[1 - f_{F,l}(E_1)] + P_0 f_{F,l}(E_1)\}. \quad (4.13)$$

Note that the probability P_0 for the QD being in the state $|0\rangle$ does not require a separate equation; by normalization, $P_0 + P_1 = 1$ so P_0 (say) can be eliminated. The position dependent tunneling rates are¹¹ $\Gamma_L(x) = \Gamma \exp(-x/\lambda)$ and $\Gamma_R(x) = \Gamma \exp(x/\lambda)$.

We can now write the charge q in the capacitive force as $-eP_1$, since an electron with charge $-e$ is occupying the QD with probability P_1 .

4.3.5 Static QD & Tunneling Current

Let us set the time derivatives to zero and consider the static solutions to the mechanical and electronic equations, $x = x^{\text{st}}$ and $P_1 = P_1^{\text{st}}$. We then calculate the electric current between the leads by considering the difference

¹⁰Sometimes “master equations” or “kinetic equations”.

¹¹This is the reason for the “2” introduced alongside λ earlier.

4.3. EXAMPLE: THE SHUTTLE INSTABILITY

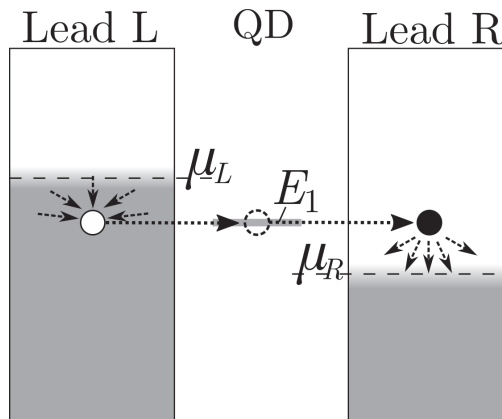


Figure 4.3: The electronic energies of the system shown in fig. 4.2. The voltage biased electronic occupation (grey) inside the leads promotes tunneling (dashed arrows) from the left lead, via the QD energy level (grey line), to the right lead. Excitations quickly relax inside the leads (small converging/diverging arrows).

in rates of tunneling left and right. Due to the voltage bias V between the leads, electrons preferentially tunnel from the left lead, via the QD, to the right lead (fig. 4.3). This *tunneling current* is proportional to the tunneling rate Γ and increases with the voltage bias V . The tunneling current can be blocked by adjusting the gate voltage so that no QD energy level lies between the chemical potentials of the leads. Measuring the current while varying the gate voltage and voltage bias is a typical technique to map energy levels [94]. As we have seen, the tunneling current exists even for a static QD. However, QD movement can significantly modify the current-voltage characteristics.

4.3.6 Actuation & Shuttle Current

Let us now consider the stability of the system. We make the second-order eq. (4.1) for the grain position x into two first-order equations by defining the velocity: $\partial_t x \equiv v$. We then use ω and λ to nondimensionalize the system and consider small deviations from the static solution. We get a matrix equation, $\partial_\tau \chi(\tau) = \mathbf{M} \chi(\tau)$, where \mathbf{M} is constant matrix and the system state vector is $\chi(\tau = t\omega) = (\delta x/\lambda, \delta v/[\lambda\omega], \delta P_1)^T$. This is a *linear dynamical system*; the stability of the origin (the static solution) can be analyzed using standard techniques, e.g., by considering the eigenvalues of \mathbf{M} . It is then found that that the origin becomes unstable when the voltage bias exceeds a certain threshold voltage [114, 129], $V > V_{\text{thr}}$. This electromechanical instability results in oscillations in both the charge $-eP_1$ and the grain position x . The

source of energy which pumps these oscillations is the maintained voltage bias V between the leads.

It is found that these oscillations result in a time averaged direct current. This “shuttle current” is due to the grain charging near one lead and discharging near the other. As it approaches one lead, tunneling causes the grain charge (measured with respect to the static charge) to switch sign. Thus, the force switches sign and the grain accelerates toward the other lead, where tunneling again switches the direction of the force¹². In this way, the grain oscillations “shuttle” electrons between the leads [129].

In the next section, we will put some of the concepts introduced in the last two sections to use and summarize paper IV.

4.4 Summary of Paper IV

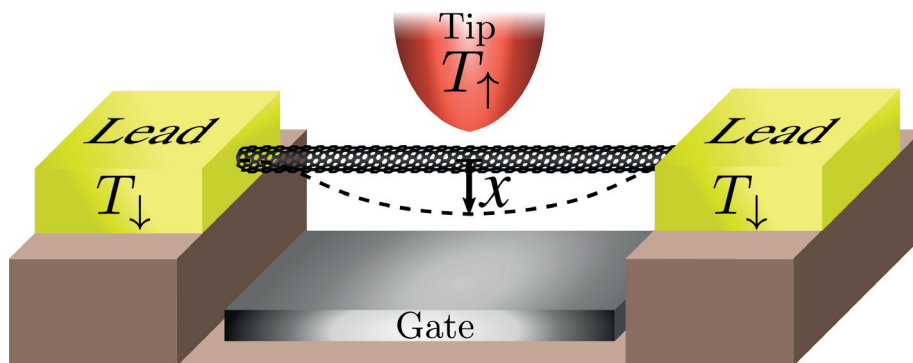


Figure 4.4: A carbon nanotube (CNT) is suspended between two half-metallic leads (yellow) which are spin-polarized with spin down (\downarrow) and held at temperature T_{\downarrow} . A tip electrode (red) with opposite spin polarization (\uparrow) and different temperature T_{\uparrow} is suspended above the CNT and thus sensitive to the CNT mechanical deflection x (black arrow). The deflection x is acted upon by a capacitive force from an underlying gate (grey). We consider the two leads as a single reservoir of spin-down electrons and the tip as a reservoir of spin-up electrons. Electrons can tunnel back and forth between the CNT and their source reservoir, but not between reservoirs.

We consider a carbon nanotube (CNT) suspended between two electronic leads (fig. 4.4). The mechanical subsystem consists of the fundamental bending mode of the CNT, described by the CNT deflection x and modeled as a damped harmonic oscillator. The CNT deflection is capac-

¹²For an old-school electromechanical shuttle, google “Franklin bells”.

4.4. SUMMARY OF PAPER IV

itively coupled to an underlying gate, resulting in an electrostatic driving force $F_{el} = -\partial_x[q^2/C(x)]$. [See sec. 4.2 and eq. (4.1).]

The length of the CNT is assumed to be small enough so that the spatial quantization of electronic energies renders all but two energy levels \mathcal{E}_1^σ inert, one per spin $\sigma = \uparrow, \downarrow$. The CNT thereby operates as a two-electron quantum dot (QD, see subsection 4.3.1) with four possible states: the charge neutral state $|0\rangle$, the state with an extra spin-up (-down) electron $|\uparrow\rangle$ ($|\downarrow\rangle$), and the doubly populated state $|2\rangle$ containing two extra electrons, one of each spin. Introducing electronic creation operators \hat{d}_σ^\dagger , we have $|\sigma\rangle = \hat{d}_\sigma^\dagger |0\rangle$, $|2\rangle = \hat{d}_\uparrow^\dagger \hat{d}_\downarrow^\dagger |0\rangle$, and the number operators $\hat{n}_\sigma = \hat{d}_\sigma^\dagger \hat{d}_\sigma$.

The leads at the ends of the CNT are *half-metallic*, meaning that they—in the considered range of energies—only have states with a single spin, in this case spin down [131]. Spin-down electrons can tunnel¹³ through thin insulating barriers between the leads and the CNT. Since both leads are equivalent, we will model the *pair of leads* as a single reservoir of spin-down electrons (see subsection 4.3.3). Another electrode, in the form of a tip, is positioned above the middle of the CNT, close enough for electron tunneling—tunneling which is sensitive to the CNT deflection x (see subsection 4.3.2). The tip is also half-metallic, but in contrast to the leads, it has only spin-*up* states, and thus serves as a reservoir of spin-up electrons. The half-metallic nature of the reservoirs prevents electron exchange between them; electrons can only tunnel back and forth between the QD and their respective reservoir (a “spin-valve effect”). We choose the chemical potential μ in each reservoir to be the same, but hold the spin-up reservoir (the tip electrode) at temperature T_\uparrow and the spin-down reservoir (the leads) at temperature T_\downarrow . We assume that excitations inside the reservoirs relax quickly so that the reservoirs can be treated as if always in thermal equilibrium.

By applying a static voltage to the gate underneath the CNT, the QD energy levels are tuned so that the single-electron energies (adjusted for QD-gate capacitance) $E_1^\sigma(x) = \mathcal{E}_1^\sigma + e^2/C(x)$ are below the chemical potential μ but the energy $E_2(x)$ of the double-populated state $|2\rangle$ is above it (fig. 4.5). The extra energy in the double-populated state cannot be understood in terms of single-electron energy levels and is a consequence of *electron-electron interaction* through the capacitive coupling. The CNT-gate capacitor has capacitive energy $E_C = q^2/C(x)$, which is a *quadratic* function of q . It therefore follows that adding a second electron to the singly occupied QD requires the

¹³We assume that electrons do not change spin during tunneling events.

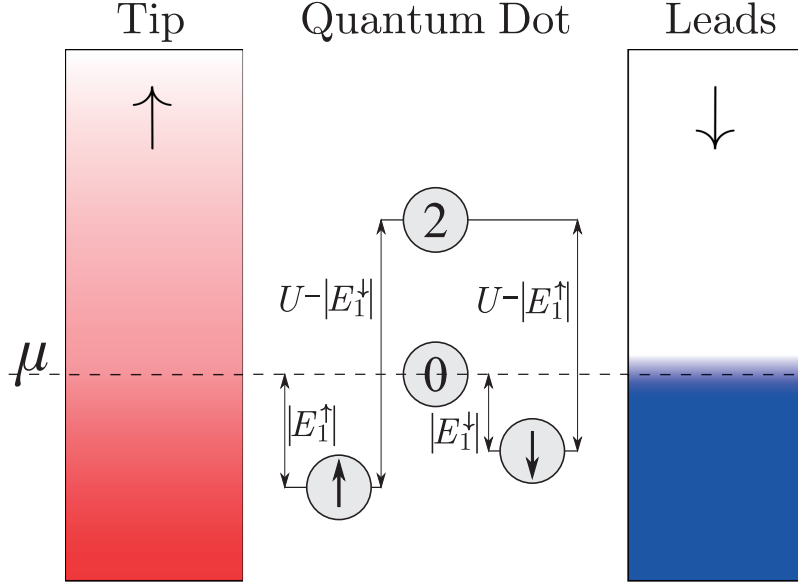


Figure 4.5: Schematic picture of the two reservoirs and the QD states. The single-electron energy levels are below the chemical potential μ , $E_1^\uparrow, E_1^\downarrow < E_0 \equiv 0$. Color (red/blue) opacity indicates state occupancy. However, the electron-electron interaction energy U ensures that when the QD is double-populated, it has an energy $E_2 = E_1^\uparrow + E_1^\downarrow + U$ which is higher than μ , since $U > |E_1^\uparrow| + |E_1^\downarrow|$.

additional energy $U = [(2e)^2 - 2e^2]/C(x) = 2e^2/C(x)$. To summarize, the electronic Hamiltonian for the QD, reservoirs (R), and tunneling (T) is

$$\begin{aligned} \hat{H}_{\text{QD}} &= E_1^\uparrow(x)\hat{n}_\uparrow + E_1^\downarrow(x)\hat{n}_\downarrow + U(x)\hat{n}_\uparrow\hat{n}_\downarrow, \\ \hat{H}_R &= \sum_{\mathbf{k}, \sigma=\uparrow, \downarrow} \varepsilon_{\mathbf{k}, \sigma} \hat{c}_{\mathbf{k}, \sigma}^\dagger \hat{c}_{\mathbf{k}, \sigma}, \quad \hat{H}_T = \sum_{\mathbf{k}} \left(\mathcal{T}_\uparrow e^{-x/[2\lambda]} \hat{c}_{\mathbf{k}, \uparrow}^\dagger \hat{d}_\uparrow + \mathcal{T}_\downarrow \hat{c}_{\mathbf{k}, \downarrow}^\dagger \hat{d}_\downarrow + \text{H.c.} \right). \end{aligned} \quad (4.14)$$

Inserting the total electronic Hamiltonian $\hat{H}_{\text{QD}} + \hat{H}_R + \hat{H}_T$ in the Liouville-von-Neumann equation, we can then derive a system of rate equations for the probabilities P_α for the QD to be in either of the states $\alpha = 0, \uparrow, \downarrow, 2$ (see subsection 4.3.4). The CNT deflection enters into these equations in two ways: 1) through the energies entering the Fermi occupation probabilities, and 2) through the exponential deflection dependence of the tunneling rate of spin-up electrons $\propto \exp(-x/\lambda)$, where λ is an effective tunneling length. We neglect the first of these effects but keep the latter¹⁴. The electronic subsystem is thus affected by the CNT deflection through the changes in the

¹⁴This assumption is further motivated in the paper.

tunneling rate of spin-up electrons. In turn, the CNT deflection is affected by the electronic QD state through the capacitive force

$$F_{\text{el}} = (-\partial_x E_1^\uparrow)n_\uparrow + (-\partial_x E_1^\downarrow)n_\downarrow + (-\partial_x U)P_2 \quad (4.15)$$

where $n_\sigma = P_\sigma + P_2$ is the probability of finding a spin- σ electron on the QD and the forces in parentheses are assumed constant¹⁵.

4.4.1 Results: Actuation by a Heat Flow

Due to the spin-valve effect, there is neither mass nor charge transfer between the reservoirs. Nevertheless, energy exchange is possible due to the electron-electron interaction induced through the capacitive coupling. Let us assume that $T_\uparrow > T_\downarrow$. There is then a *heat flow* from the tip to the leads through the QD, mediated by the electron-electron interaction U . To understand how this works, let us first assume that the CNT is static. The energy transfer between the reservoirs can then be understood in terms of a cyclic sequence of tunneling events; this is depicted in fig. 4.6.

Of course, in actuality we do not consider a discrete chain of “tunneling events”. Rather, we consider ongoing tunneling processes which result in flows of probability between the four QD states. The effect of CNT deflection on these probability flows is explained in fig. 4.7. The CNT deflection does *not* affect the average QD charge $-e(n_\uparrow + n_\downarrow)$ since the increased tunneling to the QD is compensated by the increased tunneling from it. However, it *does* affect the average of the *square* of the charge, $e^2(n_\uparrow + n_\downarrow + 2P_2)$, which is what enters into the capacitive force¹⁶. Deflection toward (away from) the tip increases (decreases) P_2 , and thereby the capacitive force. This force has a component which is an instantaneous response to the deflection—an extra “spring force”—which simply adds to the stiffness of the CNT. However, there is also a delayed response; intuitively, a “spring force” which lags behind the mechanical oscillations and therefore accelerates the deflection past its resting position. In the paper, we explicitly show that this force can actuate the CNT deflection if the energy provided by the heat flow overcomes the intrinsic mechanical damping. An explicit excitation criterion¹⁷ is given in eq. (9), paper IV.

¹⁵That is, we approximate the capacitive force by its value at the static deflection x^{st} .

¹⁶Remember, the electron-electron interaction energy $U(x)$ entered precisely as the difference $[(2e)^2 - 2e^2]/C(x)$.

¹⁷There is a typo in paper IV, eq. (9); the factor $\omega\lambda$ belongs in the denominator.

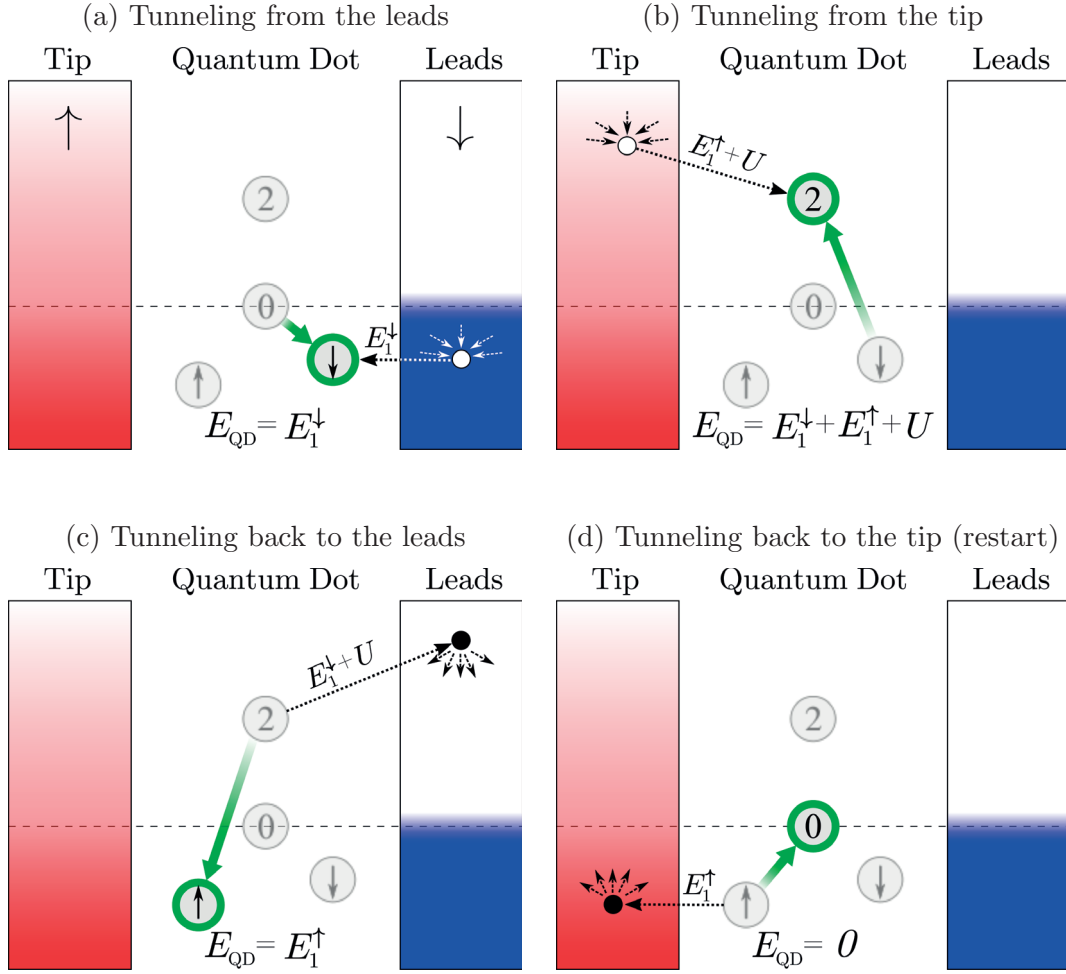


Figure 4.6: The cyclic electron dynamics resulting in a heat flow. Here, the CNT is assumed static. (a) The quantum dot (QD) is initially in the charge neutral state $|0\rangle$. A spin-down electron with energy E_1^\downarrow tunnels (dashed arrow) from a state below the chemical potential (dashed line) in the leads to the QD, bringing it (green arrow) to the state $|\downarrow\rangle$. The hole (\circ) created in the leads is quickly erased by relaxation (dashed converging arrows), leaving the spin-down electron with no state to return to. (b) Due to the relatively high temperature of the tip, there are high-energy electrons available for tunneling. A spin-up electron with energy $E_1^\uparrow + U$, where U is the electron-electron interaction energy, tunnels from the tip onto the QD, bringing it to the high-energy state $|2\rangle$. (c) The spin-down electron returns to the leads from the high-energy QD state $|2\rangle$, bringing the QD to the state $|\uparrow\rangle$. The electron returns with additional energy U , which is then dissipated inside the leads as the electronic excitation (\bullet) relaxes (dashed diverging arrows). (d) Due to the high temperature of the tip, there are empty low-energy states available, so the spin-up electron returns to the tip with energy E_1^\uparrow , which is U less energy than it left with. The QD is back in the charge neutral state $|0\rangle$ and the cycle can restart. Each cycle transfers the energy U from the tip to the leads.

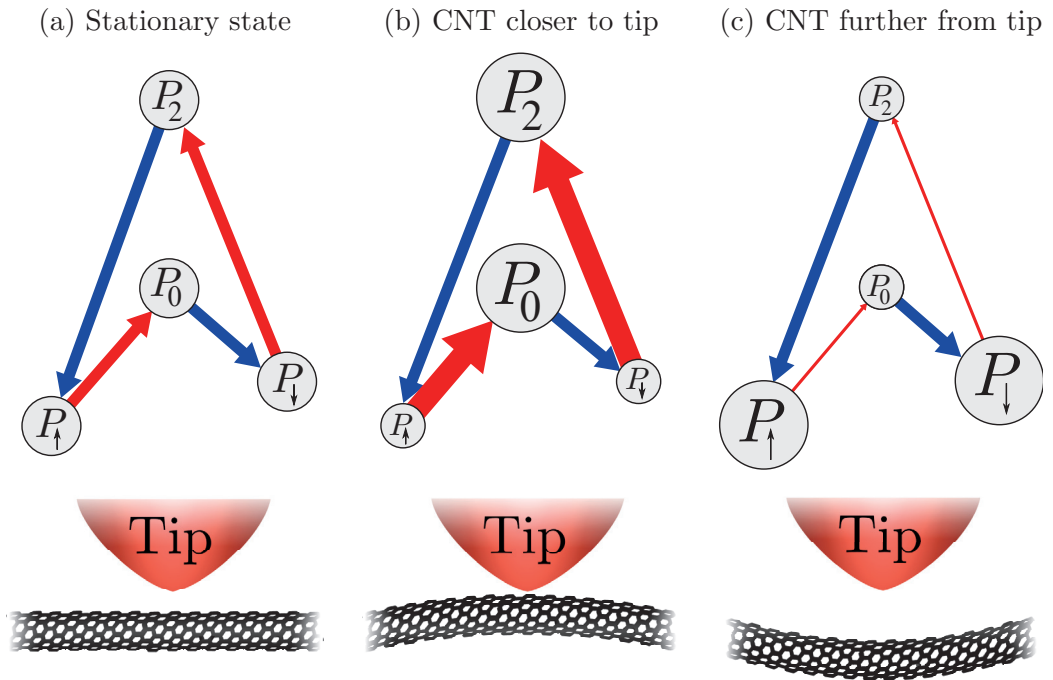


Figure 4.7: Probability flows and coupling to mechanical deflection. (a) In the stationary state, the flows of probability (arrows) between the QD states (circles) are equal. The flow of probability into a state is equal to the flow out from it. Red arrows indicate probability flow due to tunneling between the QD and the tip. Blue arrows indicate probability flow due to tunneling between the QD and the leads. (b) If the CNT is deflected toward the tip, the rate of tunneling between the QD and the tip increases (depicted schematically as thicker arrows). This creates a bottleneck effect which causes an accumulation of probability in the charge neutral and doubly occupied states (larger probabilities are here drawn as larger circles). (c) Conversely, if the CNT is deflected away from the tip, the tip-QD tunneling rate decreases (thinner arrows) and probability starts to accumulate in the singly occupied states.

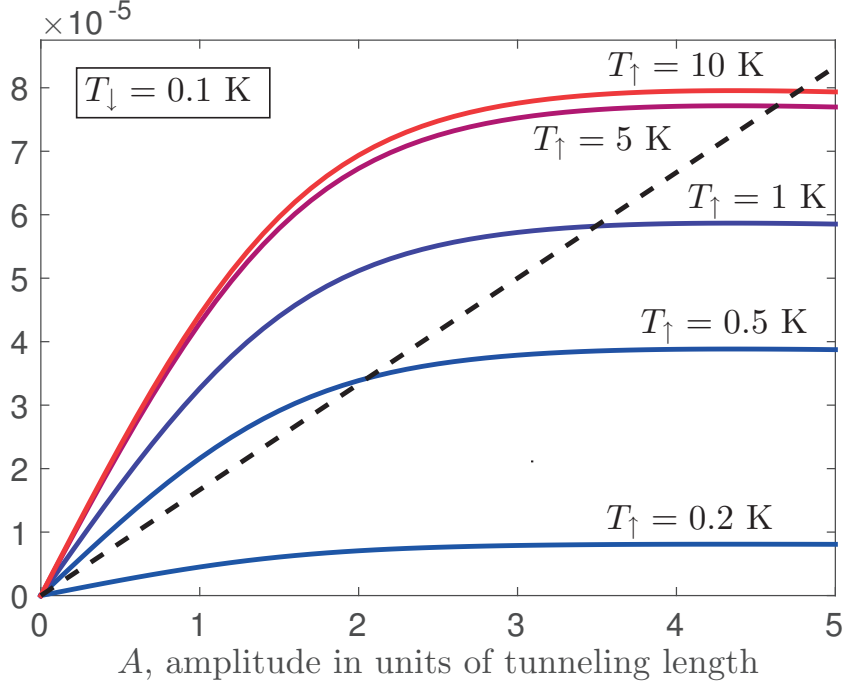


Figure 4.8: The mechanical damping (dashed, $Q = 3 \times 10^4$) and the pumping induced by the heat flow (solid lines) for different temperatures, as indicated. The ordinate is in units of $\lambda\omega$. The pumping efficiency decreases with amplitude, as evidenced by the leveling-out of the solid lines. Self-sustained oscillations occur when pumping and damping are balanced (solid-dashed intersections). We use the parameters $\lambda = 1 \text{ \AA}$, $m_{\text{eff}} = 10^{-21} \text{ kg}$, $U = -2E_1^{\sigma} = 0.1 \text{ meV}$, $|\partial_x U| \sim 10 \mu\text{eV}/\text{\AA}$, and $\omega = 2\Gamma_{\sigma} = 1 \text{ GHz}$. For further clarification, see paper IV.

Once actuated, the mechanical amplitude starts to grow. Because the pumping from the heat flow decreases in efficiency with amplitude, it eventually reaches a balance with the intrinsic mechanical damping and the amplitude stabilizes (fig. 4.8); this typically occurs for amplitudes on the order of the tunneling length $\lambda \sim 1 \text{ \AA}$. Thus, in this system, there is no need to introduce any mechanical nonlinearities (e.g., a Duffing term, see subsection 4.2.3) to saturate the mechanical amplitude.

The energy which pumps the mechanical motion is provided by the temperature difference $T_{\uparrow} - T_{\downarrow}$ of the reservoirs. The work performed by this “nanoelectromechanical heat engine” on the CNT deflection can be either positive or negative, depending on the sign of the temperature difference. This means that either pumping or damping, as desired, can always be achieved by simply adjusting the temperature difference.

4.4.2 Discussion & Outlook

The NEMS actuation method suggested here is based on a heat flow mediated by a capacitive electron-electron interaction. This heat flow does not entail any transfer of electrons between the reservoirs, and thereby it does not require any electric current. Neither did we apply an alternating field. The absence of both dc and ac driving sets it apart from many other actuation schemes [98, 106, 107, 110–117].

The prototype system (fig. 4.4) seems experimentally feasible, given its resemblance to existing devices [132]. It is also conceivable that the same phenomenon could be demonstrated in structurally dissimilar but mathematically similar systems, wherein electron exchange is blocked by some means other than a spin-valve effect.

Further theoretical work on this system should probably treat the mechanical subsystem quantum mechanically. In this way, one could study the ability of the heat engine to work as a “fridge”, i.e., if it is possible to use the same set-up to cool the mechanical subsystem. Another interesting direction would be to more carefully consider the energy transfer to the mechanical subsystem. When we modeled the CNT bending mode as a classical oscillator, we really gave the system no choice; the only way to pump energy into the resonator is to actuate its mechanical motion. However, a more careful, quantum treatment, could allow for a more detailed study of the pumping.

Before moving on to the final publication of this thesis, I will now give a brief introduction to the phenomenon of superconductivity. The reason being that paper V is an example of *superconducting* NEMS. As we shall learn in the next section, superconductivity is—in some sense—an *electromechanic* phenomenon.

4.5 Background: Superconductivity

“*The disappearance of the resistance of mercury*” is the title of a 1911 paper by the physicist Heike Kamerlingh Onnes [133], a pioneer in extreme cooling techniques. He had discovered that below a *critical temperature* of about 4.19 K, the dc resistance of mercury abruptly dropped to *zero*. Without resistance, currents persisted after their source had been removed [134]. Subsequent experiments showed that the same phenomenon could be observed in several other materials; each having a different critical temper-

ature T_c . Kamerlingh Onnes named his discovery *superconductivity*¹⁸ and it earned him the Nobel prize in 1913. While superconductivity might at first have been construed as a mere case of “perfect conductivity”, the 1933 discovery of the *Meissner effect* [135]—the total expulsion of magnetic fields from the interior of a superconductor—made it clear that the transition from the normalconducting to the superconducting state was *qualitatively* special, something thitherto undreamt of.

A phenomenological theory [136] was devised by the London brothers in 1935, but it was not until the 50s that superconductivity theory really picked up the pace. In 1950, the *Ginzburg-Landau theory* of superconductivity was presented by its eponymous creators [137]. Ginzburg and Landau drew from the latter’s own theory of thermodynamic phase transitions and characterized the superconducting state by a “*complex order parameter*” ψ , which is zero (normalconducting state) when the temperature $T > T_c$ and nonzero (superconducting state) when $T < T_c$. They then used symmetry arguments to write down the free energy in terms of ψ . The Ginzburg-Landau theory was strictly phenomenological; they gave no definite interpretation of ψ . The microscopic origin of superconductivity itself remained unknown.

An important clue was provided by the discovery of the *isotope effect*: T_c depends on the isotopic mass [138], hinting that the *lattice* somehow figures into superconductivity. This prompted R. H. Ogg to suggest that superconductivity was due to electrons forming *pairs* coupled by lattice vibrations [139]. In 1956, Leon Cooper considered a lone pair of electrons residing above a fully occupied and inert Fermi sea (this final part is important) [140]. He showed that, given an *attractive* electron-electron interaction which he assumed was phononic in origin, the electrons can lower their total energy by forming entangled pairs, *regardless* of how weak the interaction is, as long as the temperature is below a critical value. The critical temperature could then be understood by considering the temperature dependence of the pair binding energy. These bound electron pairs are now known as *Cooper pairs*. A Cooper pair should not be viewed as two conjoined electrons traveling “hand in hand”. The pair formation is rather a matter of correlation, and can be understood through a classical consideration of the origin of the phononic electron-electron attraction. Electrons are negatively charged and thus repel each other. However, they attract the positively charged ions making up the lattice, so a moving electron slightly constricts the lattice, leaving

¹⁸Originally, he named it “supraconductivity”. This term lives on in, e.g., Swedish.

4.5. BACKGROUND: SUPERCONDUCTIVITY

a wake of positive charge which can attract another electron. Reciprocally, the positive wake of that electron can attract the first one. Cooper showed that it is energetically favorable for paired electrons to be time-reversals of each other ($k \leftrightarrow -k$, spin $\uparrow \leftrightarrow \downarrow$); this allows the electrons to take maximal advantage of each other's wakes. Quantum mechanically, a Cooper-pair state is the quantum entanglement of two electronic states such that if there is an electron in the state $|\mathbf{k}, \uparrow\rangle$, there is definitely an electron in the state $|\mathbf{-k}, \downarrow\rangle$, and vice versa.

In a follow-up paper in 1957 [141], Bardeen, Cooper (again), and Schrieffer (“BCS”), generalized the theory¹⁹. In *BCS theory*, all electrons with energies close to the Fermi energy interact with each other attractively. When two electrons form a Cooper pair, the other electrons—which themselves are involved in Cooper-pair formation—constitute a background field which effectively replaces the inert Fermi sea from Cooper’s original paper. Cooper-pair formation is thus a collective phenomenon—the electrons “help” each other form pairs. Further, since Cooper pairs are comprised of two (spin-half) electrons, they obey *bosonic* statistics and can occupy the same quantum ground state. We thus find that the superconducting electrons form a collective entity—a “superconducting condensate”—which can behave essentially as a single particle. Its collective nature makes the condensate insensitive to, e.g., scattering from impurities and is the reason for the disappearance of the resistance. Since electrons near the Fermi energy can gain energy by forming Cooper pairs, an energy gap opens up preventing single-particle excitations: the *superconducting energy gap*.

While Ginzburg-Landau theory has tremendous practical use, BCS theory elucidates on the origin of the superconducting state. In the late 50s, L. P. Gor’kov connected the two theories by showing that Ginzburg-Landau theory could be derived from BCS theory [143]. He reduced the two-body interaction between electrons present in BCS theory to the one-body problem of noninteracting electrons moving in a thermally averaged (and thus temperature dependent) mean-field “pair potential” Δ , the magnitude of which is the superconducting energy gap. He then found that this pair potential could (more or less) be identified with the Ginzburg-Landau complex order parameter, $\Delta \sim \psi$.

¹⁹N. N. Bogoliubov published his own work on superconductivity at the same time [142]. He considered the phononic electron-electron interaction more explicitly and showed how to diagonalize the Hamiltonian by considering quasiparticles consisting of superpositioned electrons and holes.

I will conclude this section by noting that there are different types of superconductors, and not all of them are very well understood. “Low-temperature type-I superconductors” are those that are best understood and should conform to the impression the reader got from the above paragraphs. This is the only type with which we will concern ourselves in this thesis.

4.6 The Josephson Effect

If the superconducting energy gap is large compared to other considered energies, single-electron²⁰ excitations are forbidden. Assuming that all electrons have been paired up, we can then consider only the condensate of bosonic Cooper pairs. We will work within this model.

As was first suggested by the theoretician B. D. Josephson in 1962 [144, 145], when two superconductors are weakly coupled to each other by Cooper-pair tunneling, a finite supercurrent between them is possible even in the ground state. This *Josephson current* is known to be proportional to $\sin(\Delta\phi)$, where $\Delta\phi$ is the difference in the phases of the complex order parameters of the superconductors (we assume their magnitudes are equal). We will now introduce a simple mathematical formalism for superconductivity and use it to derive the Josephson current.

Let us consider two superconducting leads, labeled L (left) and R (right), separated by a thin insulating barrier through which Cooper-pair tunneling is possible. Tunneling allows the number of Cooper pairs to fluctuate around some average number of Cooper pairs \bar{N} , which we assume is the same for both leads. We introduce an orthogonal basis $|n_L\rangle \otimes |n_R\rangle$, where n_l is the number of excess Cooper pairs in lead $l = L, R$ measured from \bar{N} . These are the eigenstates of the number operators²¹

$$\hat{n}_l = \sum_{n_l} n_l |n_l\rangle \langle n_l|, \quad \hat{n}_l |n_l\rangle = n_l |n_l\rangle, \quad l = L, R, \quad (4.16)$$

²⁰Really electronic quasiparticles, as known from Fermi liquid theory.

²¹All summation limits have been extended to $\pm\infty$ as an approximation. This results in problems with normalization, which we brashly ignore, as is often the practice. The conscientious reader may interpret the n -summations in the states as containing an implicit normalization constant.

4.6. THE JOSEPHSON EFFECT

We use this basis to write a Cooper-pair tunneling Hamiltonian as²²

$$\begin{aligned}\hat{H}_J &= -\frac{\hbar\omega_J}{2} \sum_{n_L, n_R} |n_L - 1\rangle \langle n_L| \otimes |n_R\rangle \langle n_R - 1| + \text{H.c.} \\ &= -\frac{\hbar\omega_J}{2} e^{i\hat{\phi}_L} e^{-i\hat{\phi}_R} + \text{H.c.}\end{aligned}\quad (4.17)$$

where we have defined the unitary operators

$$e^{i\hat{\phi}_l} \equiv \sum_{n_l} |n_l - 1\rangle \langle n_l|, \quad l = L, R, \quad (4.18)$$

which can be shown to satisfy

$$\left[e^{\pm i\hat{\phi}_l}, \hat{n}_l \right] = \pm e^{i\hat{\phi}_l}, \quad l = L, R. \quad (4.19)$$

For a normalconducting lead, we usually assume that its state is effectively unchanged by tunneling events due to a rapid relaxation to equilibrium (see subsection 4.3.3). However, a *superconducting* lead should be in a coherent quantum mechanical state. Further, the Josephson current is a ground-state phenomenon. From these arguments, it follows that the states of the leads must be eigenstates of the tunneling Hamiltonian, i.e., of the operators in eq. (4.18). These operators have the eigenstates

$$e^{\pm i\hat{\phi}_l} |\phi_l\rangle = e^{\pm i\phi_l} |\phi_l\rangle, \quad |\phi_l\rangle = \frac{1}{\sqrt{2\pi}} \sum_{n_l} e^{i\phi_l n_l} |n_l\rangle, \quad 0 \leq \phi_l < 2\pi; \quad (4.20)$$

we will refer to ϕ_l as the *phase* of the (condensate in) lead l . Note that these eigenstates are superpositions of states with different number of Cooper pairs.

Now, in order to have a current between the superconductors, it is necessary to break the left-right symmetry of the system. If the two leads were completely identical, there would be no preferred direction and therefore no average current. Let us therefore suppose that the two leads are in different eigenstates, $\phi_L \neq \phi_R$, and write the ground state as $|\phi_L\rangle \otimes |\phi_R\rangle$. To calculate the tunneling current, we first use eq. (4.19) and charge conservation to derive a Heisenberg-picture current operator

$$\hat{J} = (-2e)\partial_t \hat{n}_L = (-2e)\frac{i}{\hbar} \left[\hat{H}_J, \hat{n}_L \right]. \quad (4.21)$$

²²We assume that \bar{N} is large so that the effect of adding or removing a single Cooper pair is negligible.

We then calculate the ground-state expectation value of \hat{J} . Using eq. (4.20),

$$\langle \phi_R | \otimes \langle \phi_L | \hat{J} | \phi_L \rangle \otimes | \phi_R \rangle = 2e\omega_J \sin(\Delta\phi) \quad (4.22)$$

where $\Delta\phi \equiv \phi_R - \phi_L$. We interpret the phases ϕ_j as the phases of the complex order parameters of the leads and identify the Josephson current.

We conclude this section by noting that, from eq. (4.20), it follows that an *isolated* superconductor, wherein the number of Cooper pairs is fixed, is in a number state

$$|n\rangle = \frac{1}{\sqrt{2\pi}} \int_0^{2\pi} d\phi e^{-i\phi n} |\phi\rangle \quad (4.23)$$

and thus does not have a definite phase. It is therefore meaningless to speak of the “phase” of an isolated superconductor²³. However, phase *differences*, as we have seen, have real physical implications.

4.7 The Cooper-Pair Box

A *Cooper-pair box* (CPB) is a superconducting QD (see section 4.3.1). Basically, a CPB is created when a metallic QD is cooled to the superconducting state. We write the electrostatic energy of a CPB containing $N = \bar{N} + n$ Cooper pairs (see section 4.6) as²⁴ [129, 146]

$$E_{\text{CPB}} = E_C [2N - \alpha V_G]^2 = E_C [2\bar{N} + 2n - \alpha V_G]^2, \quad (4.24)$$

where V_G is a gate voltage used to tune the CPB energies and E_C and α are parameters. If we tune V_G so that $\alpha V_G = 2\bar{N} + 1$, we get

$$E_{\text{CPB}} = E_C [2n - 1]^2, \quad (4.25)$$

which is degenerate in $n = 0, 1$. This hints at the possibility of creating coherent superpositions of the QD states $|0\rangle$ and $|1\rangle$, which differ by one Cooper pair [129, 146]. Let us consider a CPB which can exchange Cooper pairs with two superconducting leads, labeled $l = L, R$. A tunneling Hamiltonian can be written [cf. eq. (4.17)]

$$\hat{H}_J = \hat{H}_J^{(L)} + \hat{H}_J^{(R)}, \quad \hat{H}_J^{(l)} = -\frac{\hbar\omega_J^{(l)}}{2} \sum_{n_l} |n_l - 1\rangle \langle n_l| \otimes |1\rangle \langle 0| + \text{H.c.} \quad (4.26)$$

²³Although people frequently do so.

²⁴As always, we assume that Δ is large enough to prevent single-electron excitations. In this case, $\Delta > E_C$.

4.8. SUMMARY OF PAPER V

Analogously to section 4.6, we write the (unchanging) states of the superconducting leads as $|\phi_L\rangle \otimes |\phi_R\rangle$ [see eq. (4.20)], and get

$$\hat{H}_J = \sum_{l=L,R} -\frac{\hbar\omega_J^{(l)}}{2} e^{i\phi_l} |1\rangle \langle 0| + \text{H.c.} \quad (4.27)$$

Since the leads are always in the same states, we usually omit them and consider only the CPB states $|0\rangle$ and $|1\rangle$. The leads appear only as phase factors in the tunneling matrix elements. The tunneling Hamiltonian \hat{H}_J couples $|0\rangle$ and $|1\rangle$, causing an energy splitting $\hbar[\omega_J^{(L)} + \omega_J^{(R)}]/2$. The new energy eigenstates are $[|0\rangle \pm |1\rangle]/\sqrt{2}$, i.e., superpositions of none or a single excess Cooper pair. This kind of *single-Cooper-pair* box has been realized experimentally [147, 148]. The operator for supercurrent between the leads, via the CPB, is

$$\hat{J} = (-2e) \frac{\partial_t \hat{n}_L - \partial_t \hat{n}_R}{2} = -ei \left(\omega_J^{(l)} e^{i\Delta\phi/2} - \omega_J^{(r)} e^{-i\Delta\phi/2} \right) |1\rangle \langle 0| + \text{H.c.} \quad (4.28)$$

where we used eq. (4.19) and made a unitary transformation so that only the phase difference $\Delta\phi = \phi_R - \phi_L$ appears explicitly. It can be shown that the asymmetry $\omega_J^{(L)} \neq \omega_J^{(R)}$ cannot by itself lead to a tunneling supercurrent. On the other hand, $\Delta\phi \neq 0$ *does* lead to a tunneling current, as might be surmised from section 4.6. If $\Delta\phi = 0$, current is prohibited by symmetry.

In paper V, we consider a symmetric system with zero phase difference and show how, in spite of this, a direct supercurrent can be achieved nanoelectromechanically.

4.8 Summary of Paper V

In paper V, we consider a system similar to the nanoelectromechanical shuttle (section 4.3), but superconducting, see fig. 4.9. We have a single-Cooper-pair box (CPB, see section 4.7) sandwiched in the middle of the gap between two superconducting leads with which it can exchange Cooper pairs through tunneling, see eq. (4.27). Crucially, we assume that the leads are held at *zero* phase difference, $\Delta\phi \equiv 0$. For a static CPB, we would thus get zero supercurrent between the leads (see section 4.7). The purpose of the paper is to show how a direct supercurrent can be achieved, regardless of the left-right symmetry of the system, by considering a *movable* CPB.

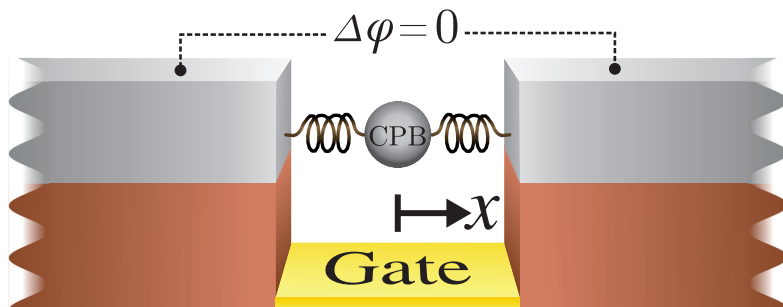


Figure 4.9: A schematic picture of the system. A Cooper-pair box (CPB, grey sphere) is attached to springs allowing it to oscillate laterally between two superconducting leads (grey blocks). Its position x is measured from its resting position in the middle of the gap. A gate (yellow) is used to tune the CPB as well as to apply an ac driving field. The leads are held at zero phase difference, making the system perfectly symmetric about $x = 0$. (Brown components are insulating.)

We designate the CPB position by \hat{x} and model it as a quantum harmonic oscillator (hence the springs in fig. 4.9) with a Duffing term (see subsection 4.2.3). Cooper-pair tunneling is \hat{x} -dependent in the same way as single-electron tunneling is, so we introduce an effective tunneling length λ (see subsection 4.3.2) through $\omega_J^{(L)} = \omega_J \exp(-x/\lambda)$, $\omega_J^{(R)} = \omega_J \exp(+x/\lambda)$, see eq. (4.27). We do not include any capacitive forces; however, since the tunneling matrix elements depend on \hat{x} , they result in forces pulling the CPB toward the leads. At $x = x^{\text{st}} = 0$, these forces exactly cancel each other.

We assume that the CPB state $|0\rangle$ is charge neutral so that the charged state $|1\rangle$ has charge $-2e$. We use the same gate which tunes the CPB state (see section 4.7) to also apply an ac voltage V_0 , oscillating harmonically with frequency Ω , which modulates the energy of the charged state. The full Hamiltonian is therefore

$$\hat{H} = \left(\frac{\hat{p}^2}{2m} + \frac{m\omega_m^2 \hat{x}^2}{2} + \frac{\eta}{4} \hat{x}^4 \right) - 2eV_0 \cos(\Omega t) |1\rangle \langle 1| \quad (4.29)$$

$$- \frac{\hbar\omega_J}{2} (e^{-\hat{x}/\lambda} |1\rangle \langle 0| + e^{\hat{x}/\lambda} |1\rangle \langle 0| + \text{H.c.}).$$

4.8.1 Results: Actuation & Supercurrent

We assume that the ac voltage is weak and introduce the small parameter $\epsilon = eV_0/[\hbar\omega_J] \ll 1$. Additionally, we assume that the amplitude of mechanical oscillations is much smaller than λ . As an approximation, we calculate

4.8. SUMMARY OF PAPER V

the electronic²⁵ dynamics for a static CPB, $x = x^{\text{st}} = 0$. In this approximation, the charge dynamics are dominated by the ac driving field. As can be expected, we find that the ac field induces charge oscillations on the CPB,

$$q(t) \approx -e[1 + 2\epsilon \cos(\Omega t)]. \quad (4.30)$$

We then calculate the mechanical dynamics of the CPB under the assumption that the electronic dynamics are unaffected by CPB movement. We find that the forces pulling the CPB toward the leads have components which oscillate with *twice* the driving frequency Ω . When $\Omega \approx \omega$, this therefore results in mechanical actuation through parametric resonance (see subsection 4.2.3). The energy pumping the mechanical motion is provided by the ac driving field. The CPB position is parametrically actuated to one of *two* stable limit cycles,

$$x_{\pm}(t) = A \sin\left(\Omega t \pm \frac{\pi}{2}\right), \quad A \sim \epsilon \sqrt{\frac{\hbar\omega_J}{6\lambda^2\eta}}. \quad (4.31)$$

The mechanical oscillations have the same frequency as the charge oscillations since they both share a common origin, cf. eqs. (4.31) and (4.30). We find that the combined electromechanical CPB dynamics are circular trajectories in charge-position space (fig. 4.10). The trajectory is clockwise for one stable state and counterclockwise for the other; we therefore call these two stable states “chiral states”. In a chiral state, the CPB effectively charges near one lead and discharges near the other, and we find that there is a superconducting shuttle current between the two leads (see subsection 4.3.6). The time averaged supercurrent—see eq. (4.28)—is equal in magnitude but opposite in direction for the two chiral states:

$$\bar{J}_{\pm} \approx \pm e\Omega \frac{A}{\lambda} \frac{eV_0}{2\hbar\omega_J}. \quad (4.32)$$

We have thus shown that a direct supercurrent can appear in a left-right symmetric system. The direction of the supercurrent is the result of a spontaneous breaking of symmetry. The symmetry is broken as the mechanical subsystem is parametrically actuated to one of two possible stable limit cycles. Which cycle is reached is random; it is the result of fluctuations from the unstable static position (assuming that the initial conditions are symmetric).

²⁵“Electronic” in the sense that Cooper pairs are paired electrons.

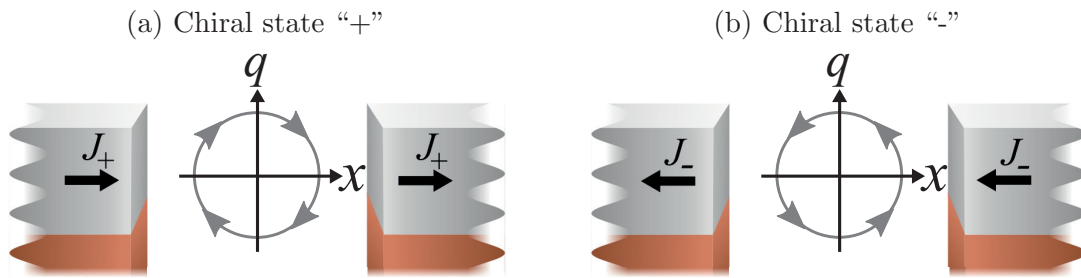


Figure 4.10: Charge-position dynamics in the chiral states “+” (a) and “-” (b). Due to the automatic synchronization of the charge and position oscillations, the CPB charges near one lead and discharges near the other. Cooper pairs are therefore coherently transferred between the leads, creating a direct supercurrent J_{\pm} . The direction of the supercurrent is different for the two chiral states.

4.8.2 Results: Noise-Induced Supercurrent Reversal

Finally, we consider the influence of noise in the system by adding a weak stochastic force to the (now assumed classical) mechanical dynamics. We estimate that the fluctuations will cause relatively rare transitions between the chiral states, $x_-(t) \leftrightarrow x_+(t)$. Such transitions flip the phase of the mechanical oscillations and thus reverses the supercurrent direction. This kind of stochastic process, where the system switches infrequently between two distinct states, is called a *telegraph process*.

4.8.3 Discussion & Outlook

In the last decade, there have been several theoretical proposals for how to achieve a supercurrent without a phase difference [149–159] and recently one was realized experimentally [160]. In that experiment, they utilized an external magnetic field and spin-orbit coupling to *explicitly* break the symmetries preventing a supercurrent. Our proposal uses NEMS techniques to break the spatial²⁶ symmetry *spontaneously*. As an implication of this, the supercurrent can flow in either direction for the same system parameters.

Our system is similar to that in ref. 161. However, there, the authors considered a *normalconducting* system with *incoherent* electron transport described by electronic rate equations (see subsection 4.3.4). Superconducting components allow us to consider the coherent transport of Cooper pairs.

²⁶The time-reversal symmetry is explicitly broken by the ac driving field. This also means that the supercurrent is a nonequilibrium phenomenon.

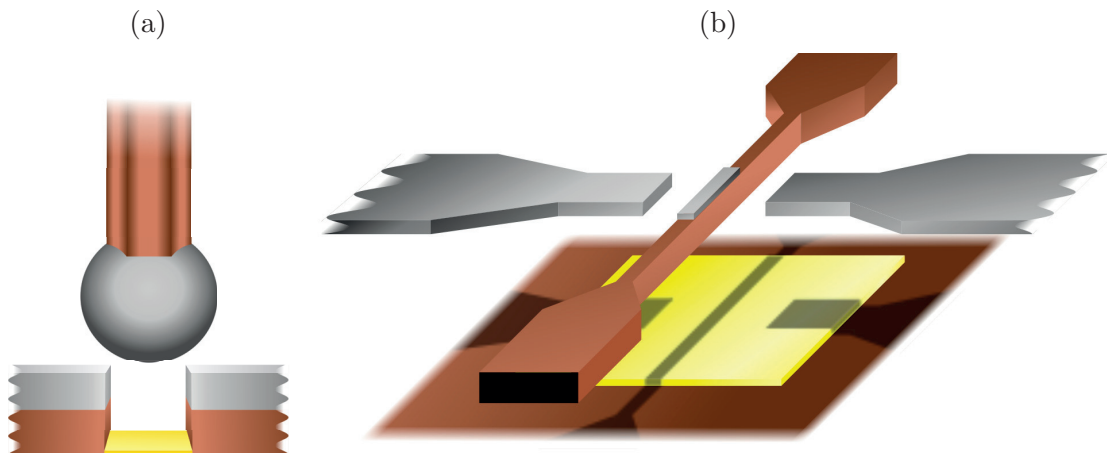


Figure 4.11: Two ways to realize the system schematically depicted in fig. 4.9. (a) A bendable nanowire with a superconducting seed (grey sphere), suspended between two superconducting leads (grey blocks). (b) A superconducting metallic island (grey rectangle) on a nanobeam which is free to oscillate laterally between two superconducting leads (grey). (Brown components are insulating.)

Using a movable CPB to coherently transport Cooper pairs was originally suggested in refs. 162 and 163. In those publications, the CPB had an explicitly time dependent position and was only in tunneling contact with one lead at a time. In comparison, our system might prove easier to realize experimentally and thus allow for an experimental study of the considered phenomena.

The system shown in fig. 4.9 is schematic; as noted in section 4.3, there are²⁷ no actual mesoscopic “springs” (yet). However, a system with the considered mathematical structure can potentially be realized in a number of ways, see fig. 4.11 for two examples. Since the geometry of the system is essentially that of the shuttle instability (section 4.3), but superconducting, it can be expected that experimental techniques applied to one of them might also be applicable to the other.

²⁷To the author’s knowledge.

Chapter 5

Concluding Words

One of the joys of mesoscopic physics is that it draws upon and combines so much of physics. The classical theory of acoustic waves, laid out and employed in chapter 2, carries without modification over to the graphene sheet considered in chapter 3. There, surface acoustic waves—originally described in the 1800s by Lord Rayleigh—merge elegantly with electrons—described by the quantum theory of the 1900s—to produce electroacoustic solitons¹.

It is the intermediate scale of mesoscopic physics which allows us to utilize such a large portion of the physicist’s toolbox: the classical and quantum harmonic oscillators, the theory of elasticity, electrostatics and electrodynamics, quantum mechanics, thermodynamics, superconductivity, etc.

Scientists are now testing the limits between classical and quantum physics, and on the applications side, a “quantum revolution” is picking up pace. As technology shrinks, mesoscopic physics grows.

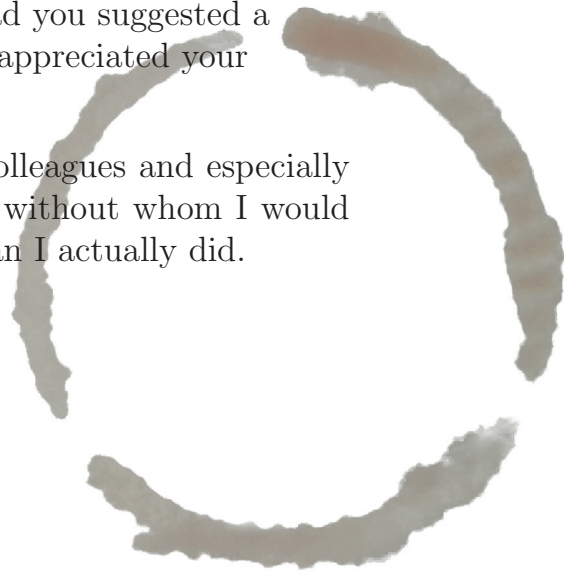
¹As an aside, the soliton phenomenon was first identified by John Scott Russell as a “solitary” water wave traveling down the Union Canal in Scotland. This was in 1834, 8 years before the birth of Lord Rayleigh.

ACKNOWLEDGMENTS

First of all, I thank my supervisor, Leonid Gorelik, for his guidance and patience.

Secondly, I thank Martin. I'm glad you suggested a collaboration, and I have greatly appreciated your assistance and company.

Thirdly, I thank the rest of my colleagues and especially all of my friends and loved ones, without whom I would have crashed even more times than I actually did.



Bibliography

- [1] D. S. Ballantine, R. M. White, S. J. Martin, A. J. Ricco, E. T. Zellers, G. C. Frye, and H. Wohltjen, *Acoustic wave sensors: Theory, design, and physico-chemical applications*, Applications of modern acoustics, Academic Press, 1997.
- [2] D. Johannsmann, *The quartz crystal microbalance in soft matter research: Fundamentals and modeling*, Soft and Biological Matter, Springer International Publishing, 2014.
- [3] G. Sauerbrey, *Verwendung von Schwingquarzen zur Wägung dünner Schichten und zur Mikrowägung*, Z. Phys. **155** (1959), 206–212.
- [4] Michael Rodahl, Fredrik Höök, Anatol Krozer, Peter Brzezinski, and Bengt Kasemo, *Quartz crystal microbalance setup for frequency and Q-factor measurements in gaseous and liquid environments*, Review of Scientific Instruments **66** (1995), no. 7, 3924–3930.
- [5] Nurbek Kakenov, Osman Balci, Omer Salihoglu, Seung Hyun Hur, Sinan Balci, and Coskun Kocabas, *Weighing graphene with QCM to monitor interfacial mass changes*, Applied Physics Letters **109** (2016), no. 5, 053105.
- [6] M. Ohring, *Materials science of thin films*, Elsevier Science, 2001.
- [7] W. H. King, *Piezoelectric sorption detector*, Analytical Chemistry **36** (1964), no. 9, 1735–1739.
- [8] Setyawan P. Sakti, Nur Chabibah, Senja P. Ayu, Masdiana C. Padaga, and Aulanni'am Aulanni'am, *Development of QCM biosensor with specific cow milk protein antibody for candidate milk adulteration detection*, Journal of Sensors (2016).

- [9] Thomas Frisk, Niklas Sandström, Lars Eng, Wouter van der Wijngaart, Per Månsson, and Göran Stemme, *An integrated QCM-based narcotics sensing microsystem*, *Lab Chip* **8** (2008), 1648–1657.
- [10] Thomas Johansson, *Affinity Measurements Using Quartz Crystal Microbalance (QCM)*, pp. 683–693, Springer, Berlin, Heidelberg, 2010.
- [11] K. Kanazawa and J. G. Gordon, *The oscillation frequency of a quartz crystal resonator in contact with a liquid*, *Anal. Chim. Acta* **175** (1985), 99–105.
- [12] N. Doy, G. McHale, M. I. Newton, C. Hardacre, R. Ge, J. M. MacInnes, D. Kuvshinov, and R. W. Allen, *Small volume laboratory on a chip measurements incorporating the quartz crystal microbalance to measure the viscosity-density product of room temperature ionic liquids*, *Biomicrofluidics* **4** (2010), no. 1.
- [13] Kerstin Länge, Bastian E. Rapp, and Michael Rapp, *Surface acoustic wave biosensors: a review*, *Anal. Bioanal. Chem.* **391** (2008), no. 5, 1509–1519.
- [14] Michael Saitakis and Electra Gizeli, *Acoustic sensors as a biophysical tool for probing cell attachment and cell/surface interactions*, *Cell. Mol. Life Sci.* **69** (2011), no. 3, 357–371.
- [15] Fabrice Martin, Michael I. Newton, Glen McHale, Kathryn A. Melzak, and Electra Gizeli, *Pulse mode shear horizontal-surface acoustic wave (SH-SAW) system for liquid based sensing applications*, *Biosens. Bioelectron.* **19** (2004), no. 6, 627–632.
- [16] Electra Gizeli, Nicholas J. Goddard, Christopher R. Lowe, and Adrian C. Stevenson, *A Love plate biosensor utilising a polymer layer*, *Sensor. Actuat. B-Chem.* **6** (1992), no. 13, 131–137.
- [17] R. M. White and F. W. Voltmer, *Direct piezoelectric coupling to surface elastic waves*, *Applied Physics Letters* **7** (1965), no. 12, 314–316.
- [18] Hank Wohltjen, *Mechanism of operation and design considerations for surface acoustic wave device vapour sensors*, *Sensors and Actuators* **5** (1984), no. 4, 307–325.

- [19] Jennifer Brookes, Rory Bufacchi, Jun Kondoh, Dorothy M. Duffy, and Rachel A. McKendry, *Determining biosensing modes in SH-SAW device using 3D finite element analysis*, Sensors and Actuators B: Chemical **234** (2016), 412–419.
- [20] M. V. Voinova, *Modelling of the response of acoustic piezoelectric resonators in biosensor applications - Part 1: The general theoretical analysis*, J. Sens. Sens. Syst. **4** (2015), 137–142.
- [21] L. D. Landau and E. M. Lifshitz, *Theory of Elasticity*, Course of Theoretical Physics, no. 7, Butterworth-Heinemann, Oxford, 2008.
- [22] H. Ezawa, *Phonons in a half space*, Ann. Phys. **67** (1971), 438–460.
- [23] A. E. H. Love, *Some problems of geodynamics: Being an essay to which the Adams Prize in the University of Cambridge was adjudged in 1911*, Nineteenth Century Collections Online: Science, Technology, and Medicine: 1780-1925, Part II, University Press, 1911.
- [24] A. D. Degtyar and S. I. Rokhlin, *Stress effect on boundary conditions and elastic wave propagation through an interface between anisotropic media*, The Journal of the Acoustical Society of America **104** (1998), no. 4, 1992–2003.
- [25] K. Mitsakakis, A. Tsortos, J. Kondoh, and E. Gizeli, *Parametric study of SH-SAW device response to various types of surface perturbations*, Sensor. Actuat. B-Chem. **138** (2009), no. 2, 408–416.
- [26] Haekwan Oh, Wen Wang, Keekeun Lee, and Sangsik Yang, *Sensitivity evaluation of a Love wave sensor with multilayer structure for biochemical application*, Proc. SPIE **7207** (2009), 72070R–72070R–8.
- [27] Ernesto Calderon, Michel Gauthier, Frédéric Decremps, Gérard Hamel, Gérard Syfosse, and Alain Polian, *Complete determination of the elastic moduli of α -quartz under hydrostatic pressure up to 1 GPa: an ultrasonic study*, J. Phys. Condens. Matter **19** (2007), no. 43, 436228.
- [28] MakeItFrom.com, *Polymethylmethacrylate (PMMA, Acrylic)*, <http://www.makeitfrom.com/material-properties/Polymethylmethacrylate-PMMA-Acrylic>, page accessed 2017-03-01.

- [29] K. Saha, F. Bender, A. Rasmusson, and E. Gizeli, *Probing the viscoelasticity and mass of a surface-bound protein layer with an acoustic waveguide device*, *Langmuir* **19** (2003), no. 4, 1304–1311.
- [30] Glen McHale, Michael Ian Newton, and Fabrice Martin, *Theoretical mass, liquid, and polymer sensitivity of acoustic wave sensors with viscoelastic guiding layers*, *J. Appl. Phys.* **93** (2003), no. 1, 675–690.
- [31] Jiansheng Liu, Lijun Wang, and Shitang He, *On the fundamental mode Love wave in devices incorporating thick viscoelastic layers*, *Chin. Phys. Lett.* **32** (2015), no. 06, 064301.
- [32] A. M. Kosevich, E. S. Syrkin, and M. V. Voinova, *Acoustic sensors using Langmuir-Blodgett films*, pp. 191–199, Springer US, Boston, MA, 1995.
- [33] G. McHale, M. I. Newton, and F. Martin, *Layer guided shear horizontally polarized acoustic plate modes*, *J. Appl. Phys.* **91** (2002), no. 9, 5735–5744.
- [34] L. D. Landau and E. M. Lifshitz, *Fluid Mechanics*, Course of Theoretical Physics, no. 6, Elsevier Science, 2013.
- [35] G. McHale, M. I. Newton, and F. Martin, *Theoretical mass sensitivity of Love wave and layer guided acoustic plate mode sensors*, *J. Appl. Phys.* **91** (2002), no. 12, 9701–9710.
- [36] Luca Martinetti, Alexander M. Mannion, William E. Voje Jr., Renxuan Xie, Randy H. Ewoldt, Leslie D. Morgret, Frank S. Bates, and Christopher W. Macosko, *A critical gel fluid with high extensibility: The rheology of chewing gum*, *Journal of Rheology* **58** (2014), no. 4, 821–838.
- [37] H. Faridi and J. M. Faubion, *Dough Rheology and Baked Product Texture*, Springer US, 2012.
- [38] N. Özkaya, M. Nordin, and D. Leger, *Fundamentals of Biomechanics: Equilibrium, Motion, and Deformation*, Springer, 1999.
- [39] David B. Hall, Patrick Underhill, and John M. Torkelson, *Spin coating of thin and ultrathin polymer films*, *Polymer Engineering & Science* **38** (1998), no. 12, 2039–2045.

- [40] E. Gizeli, F. Bender, A. Rasmusson, K. Saha, F. Josse, and R. Cernosek, *Sensitivity of the acoustic waveguide biosensor to protein binding as a function of the waveguide properties*, *Biosens. Bioelectron.* **18** (2003), no. 11, 71399–1406.
- [41] Wen Wang and Shitang He, *Theoretical analysis on response mechanism of polymer-coated chemical sensor based Love wave in viscoelastic media*, *Sensors and Actuators B: Chemical* **138** (2009), no. 2, 432–440.
- [42] Jiansheng Liu, *A theoretical study on Love wave sensors in a structure with multiple viscoelastic layers on a piezoelectric substrate*, *Smart Mater. Struct.* **23** (2014), no. 7, 075015.
- [43] Jia Du and Geoffrey L. Harding, *A multilayer structure for Love-mode acoustic sensors*, *Sensors and Actuators A: Physical* **65** (1998), no. 2, 152–159.
- [44] Jiansheng Liu, *A simple and accurate model for Love wave based sensors: Dispersion equation and mass sensitivity*, *AIP Adv.* **4** (2014), no. 7, 077102.
- [45] C. Valencia, M. C. Sanchez, A. Ciruelos, and C. Gallegos, *Influence of tomato paste processing on the linear viscoelasticity of tomato ketchup*, *Revista de Agaroquimica y Tecnologia de Alimentos* **10** (2004), no. 2, 95–100.
- [46] Rod Cross, *Elastic and viscous properties of silly putty*, *American Journal of Physics* **80** (2012), no. 10, 870–875.
- [47] R. M. Christensen, *Theory of Viscoelasticity*, Civil, Mechanical and Other Engineering Series, Dover Publications, 2003.
- [48] Zhengliang Cao and Hefeng Dong, *Attenuation dispersion of Love waves in a viscoelastic multilayered halfspace*, pp. 2998–3002, Society of Exploration Geophysicists, 2010.
- [49] Neil W. Ashcroft and N. David Mermin, *Solid State Physics*, Brooks/Cole, 1976.
- [50] Sumio Iijima, *Helical microtubules of graphitic carbon*, *Nature* **354** (1991), 56–58.

- [51] L. Radushkevich and V. M. Lukyanovich, (*Russian only*), *Journal of physical chemistry* **26** (1952), 88–95.
- [52] M. S. Dresselhaus and G. Dresselhaus, *Intercalation compounds of graphite*, *Advances in Physics* **51** (2002), no. 1, 1–186.
- [53] P. R. Wallace, *The band theory of graphite*, *Phys. Rev.* **71** (1947), 622–634.
- [54] G. Dresselhaus and M. S. Dresselhaus, *Spin-orbit interaction in graphite*, *Phys. Rev.* **140** (1965), A401–A412.
- [55] Riichiro Saito, Gene Dresselhaus, Mildred S. Dresselhaus, et al., *Physical Properties of Carbon Nanotubes*, vol. 35, World Scientific, 1998.
- [56] K. S. Novoselov, A. K. Geim, S. V. Morozov, D. Jiang, Y. Zhang, S. V. Dubonos, I. V. Grigorieva, and A. A. Firsov, *Electric field effect in atomically thin carbon films*, *Science* **306** (2004), no. 5696, 666–669.
- [57] O. A. Shenderova, V. V. Zhirnov, and D. W. Brenner, *Carbon nanostructures*, *Critical Reviews in Solid State and Materials Sciences* **27** (2002), no. 1-4, 227–356.
- [58] L. D. Landau and E. M. Lifshitz, *Statistical Physics, Part I*, Butterworth-Heinemann, Oxford, 2011.
- [59] A. H. Castro Neto, F. Guinea, N. M. R. Peres, K. S. Novoselov, and A. K. Geim, *The electronic properties of graphene*, *Rev. Mod. Phys.* **81** (2009), 109–162.
- [60] K. S. Novoselov, A. K. Geim, S. V. Morozov, D. Jiang, M. I. Katsnelson, I. V. Grigorieva, and S. V. Dubonos, *Two-dimensional gas of massless Dirac fermions in graphene*, *Nature* **438** (2005), 197.
- [61] K. I. Bolotin, K. J. Sikes, Z. Jiang, M. Klima, G. Fudenberg, J. Hone, P. Kim, and H. L. Stormer, *Ultra-high electron mobility in suspended graphene*, *Solid State Communications* **146** (2008), no. 9-10, 351–355.
- [62] Changgu Lee, Xiaoding Wei, Jeffrey W. Kysar, and James Hone, *Measurement of the elastic properties and intrinsic strength of monolayer graphene*, *Science* **321** (2008), no. 5887, 385–388.

- [63] The Royal Swedish Academy of Sciences, *Scientific background on the nobel prize in physics 2010*, (2010).
- [64] Thomas C. Hales, *The honeycomb conjecture*, *Discr. Comput. Geom.* **25** (2001), 1–22.
- [65] Vikas Berry, *Impermeability of graphene and its applications*, *Carbon* **62** (2013), 1–10.
- [66] R. R. Nair, P. Blake, A. N. Grigorenko, K. S. Novoselov, T. J. Booth, T. Stauber, N. M. R. Peres, and A. K. Geim, *Fine structure constant defines visual transparency of graphene*, *Science* **320** (2008), no. 5881, 1308.
- [67] J Wang, M Liang, Y Fang, T Qiu, J Zhang, and L Zhi, *Rod-coating: towards large-area fabrication of uniform reduced graphene oxide films for flexible touch screens.*, *Advanced materials (Deerfield Beach, Fla.)* **24** (2012), no. 21, 2874–2878.
- [68] A. K. Geim and K. S. Novoselov, *The rise of graphene*, *Nat. mater.* **6** (2007), 183–191.
- [69] Henry Wohltjen and Raymond Dessy, *Surface acoustic wave probe for chemical analysis. I. Introduction and instrument description*, *Analytical Chemistry* **51** (1979), no. 9.
- [70] Sukru U. Senveli and Onur Tigli, *A novel surface acoustic wave sensor for microparticle sensing and quantification*, *IEEE Sensors Journal* **15** (2015), no. 10.
- [71] Eduardo V. Castro, H. Ochoa, M. I. Katsnelson, R. V. Gorbachev, D. C. Elias, K. S. Novoselov, A. K. Geim, and F. Guinea, *Limits on charge carrier mobility in suspended graphene due to flexural phonons*, *Phys. Rev. Lett.* **105** (2010), 266601.
- [72] I. Arias and J. D. Achenbach, *Rayleigh wave correction for the BEM analysis of two-dimensional elastodynamic problems in a half-space*, *International Journal for Numerical Methods in Engineering* **60** (2004), no. 13, 2131–2146.

- [73] Kristen Kaasbjerg, Kristian S. Thygesen, and Karsten W. Jacobsen, *Unraveling the acoustic electron-phonon interaction in graphene*, Phys. Rev. B **85** (2012), 165440.
- [74] D. V. Anghel and T. Kühn, *Quantization of the elastic modes in an isotropic plate*, Journal of Physics A: Mathematical and Theoretical **40** (2007), no. 34, 10429.
- [75] F. Mandl and G. Shaw, *Quantum Field Theory*, John Wiley & Sons, Chichester, 2008.
- [76] Daniel R. Cooper, Benjamin DAnjou, Nageswara Ghattamaneni, Benjamin Harack, Michael Hilke, Alexandre Horth, Norberto Majlis, Mathieu Massicotte, Leron Vandsburger, Eric Whiteway, and Victor Yu, *Experimental review of graphene*, ISRN Condensed Matter Physics **2012** (2012), 56.
- [77] Igor Romanovsky, Constantine Yannouleas, and Uzi Landman, *Unique nature of the lowest Landau level in finite graphene samples with zigzag edges: Dirac electrons with mixed bulk-edge character*, Phys. Rev. B **83** (2011), 045421.
- [78] L. Brey and H. A. Fertig, *Electronic states of graphene nanoribbons studied with the Dirac equation*, Phys. Rev. B **73** (2006), 235411.
- [79] V. P. Gusynin, V. A. Miransky, S. G. Sharapov, and I. A. Shovkovy, *Edge states in quantum Hall effect in graphene (review article)*, Low Temperature Physics **34** (2008), no. 10, 778–789.
- [80] Luis Brey and H. A. Fertig, *Edge states and the quantized Hall effect in graphene*, Phys. Rev. B **73** (2006), 195408.
- [81] Mitsutaka Fujita, Katsunori Wakabayashi, Kyoko Nakada, and Koichi Kusakabe, *Peculiar localized state at zigzag graphite edge*, Journal of the Physical Society of Japan **65** (1996), no. 7, 1920–1923.
- [82] Mitsuhiro Arikawa, Yasuhiro Hatsugai, and Hideo Aoki, *Edge states in graphene in magnetic fields: A specialty of the edge mode embedded in the $n=0$ Landau band*, Phys. Rev. B **78** (2008), 205401.

- [83] V. P. Gusynin, V. A. Miransky, S. G. Sharapov, I. A. Shovkovy, and C. M. Wyenberg, *Edge states on graphene ribbons in magnetic field: Interplay between Dirac and ferromagnetic-like gaps*, Phys. Rev. B **79** (2009), 115431.
- [84] M. Abramowitz and I. A. (Eds.) Stegun, *Handbook of Mathematical Functions with Formulas, Graphs, and Mathematical Tables*, New York: Dover, 1970.
- [85] E. T. Whittaker, *On the functions associated with the parabolic cylinder in harmonic analysis*, Proc. London Math. Soc. **35** (1902), 417–427.
- [86] E. Cojocaru, *Parabolic cylinder functions implemented in matlab*, arXiv:0901.2220, Mathworks online database (2009), URL: <http://www.mathworks.se/matlabcentral/fileexchange/22620>.
- [87] Z. Jiang, E. A. Henriksen, L. C. Tung, Y.-J. Wang, M. E. Schwartz, M. Y. Han, P. Kim, and H. L. Stormer, *Infrared spectroscopy of Landau levels of graphene*, Phys. Rev. Lett. **98** (2007), 197403.
- [88] P. Dean, *The constrained quantum mechanical harmonic oscillator*, Mathematical Proceedings of the Cambridge Philosophical Society **62** (1966), 277–286.
- [89] Hidekatsu Suzuura and Tsuneya Ando, *Phonons and electron-phonon scattering in carbon nanotubes*, Phys. Rev. B **65** (2002), 235412.
- [90] F. Guinea, M. I. Katsnelson, and A. K. Geim, *Energy gaps and a zero-field quantum Hall effect in graphene by strain engineering*, Nat. Phys. **6** (2010), 30.
- [91] Weiwei Liu, Younho Cho, Haidang Phan, and Jan D. Achenbach, *Study on the scattering of 2-D Rayleigh waves by a cavity based on BEM simulation*, Journal of Mechanical Science and Technology **25** (2011), no. 3, 797–802 (English).
- [92] Alexander V. Savin and Yuri S. Kivshar, *Vibrational Tamm states at the edges of graphene nanoribbons*, Phys. Rev. B **81** (2010), 165418.
- [93] A. E. Borovik, E. N. Bratus, and V. S. Shumeiko, *Hypersonic solitons in metals*, Sov. Phys. JETP **68** (1989), 826–832.

- [94] Henrik Bruus and Karsten Flensberg, *Many-Body Quantum Theory in Condensed Matter Physics*, Oxford University Press, Oxford, 2009.
- [95] C. T. Leondes, *Mems/Nems: (1) handbook techniques and applications design methods, (2) fabrication techniques, (3) manufacturing methods, (4) sensors and actuators, (5) medical applications and MOEMS*, Springer US, 2007.
- [96] R. Colin Johnson, *There's more to MEMS than meets the iPhone*, http://www.eetimes.com/document.asp?doc_id=1305409, 2007, page accessed 2017-04-27.
- [97] Bosch Semiconductors & Sensors, *Airbag systems*, http://www.bosch-semiconductors.de/en/automotive_electronics/mems/airbag_systems_2/airbagsystems_.html, 2017, page accessed 2017-04-27.
- [98] K. L. Ekinici and M. L. Roukes, *Nanoelectromechanical systems*, Review of Scientific Instruments **76** (2005), no. 6.
- [99] Nickolay V. Lavrik and Panos G. Datskos, *Femtogram mass detection using photothermally actuated nanomechanical resonators*, Applied Physics Letters **82** (2003), no. 16, 2697–2699.
- [100] K. L. Ekinici, X. M. H. Huang, and M. L. Roukes, *Ultrasensitive nanoelectromechanical mass detection*, Applied Physics Letters **84** (2004), no. 22, 4469–4471.
- [101] Y. T. Yang, C. Callegari, X. L. Feng, K. L. Ekinici, and M. L. Roukes, *Zeptogram-scale nanomechanical mass sensing*, Nano Lett. **6** (2006), no. 4, 583–586.
- [102] B. Lassagne, D. Garcia-Sanchez, A. Aguasca, and A. Bachtold, *Ultrasensitive mass sensing with a nanotube electromechanical resonator*, Nano Lett. **8** (2008), no. 11, 3735–3738.
- [103] J. Chaste, A. Eichler, J. Moser, G. Ceballos, R. Rurali, and A. Bachtold, *A nanomechanical mass sensor with yoctogram resolution*, Nature Nanotechnology **7** (2012), 301–304.

- [104] Menno Poot and Herre S.J. van der Zant, *Mechanical systems in the quantum regime*, Physics Reports **511** (2012), no. 5, 273–335.
- [105] F. Santandrea, L. Y. Gorelik, R. I. Shekhter, and M. Jonson, *Cooling of nanomechanical resonators by thermally activated single-electron transport*, Phys. Rev. Lett. **106** (2011), 186803.
- [106] P. Stadler, W. Belzig, and G. Rastelli, *Ground-state cooling of a carbon nanomechanical resonator by spin-polarized current*, Phys. Rev. Lett. **113** (2014), 047201.
- [107] J. Atalaya and L. Y. Gorelik, *Spintronics-based mesoscopic heat engine*, Phys. Rev. B **85** (2012), 245309.
- [108] A. D. O’Connell, M. Hofheinz, M. Ansmann, R. C. Bialczak, M. Lenander, E. Lucero, M. Neeley, D. Sank, H. Wang, M. Weides, J. Wenner, J. M. Martinis, and A. N. Cleland, *Quantum ground state and single-phonon control of a mechanical resonator*, Nature **464** (2010), no. 7289, 697–703.
- [109] Xining Zang, Qin Zhou, Jiyoung Chang, Yumeng Liu, and Liwei Lin, *Graphene and carbon nanotube (CNT) in MEMS/NEMS applications*, Microelectronic Engineering **132** (2015), 192–206, Micro and Nanofabrication Breakthroughs for Electronics, MEMS and Life Sciences.
- [110] K.L. Ekinici, *Electromechanical transducers at the nanoscale: Actuation and sensing of motion in nanoelectromechanical systems (NEMS)*, Small **1** (2005), no. 8-9, 786–797.
- [111] D. Garcia-Sanchez, A. M. van der Zande, A. San Paulo, B. Lassagne, P. L. McEuen, and A. Bachtold, *Imaging mechanical vibrations in suspended graphene sheets*, Nano Letters **8** (2008), no. 5, 1399–1403, PMID: 18402478.
- [112] Yuehang Xu, Changyao Chen, Vikram V. Deshpande, Frank A. DiRenno, Alexander Gondarenko, David B. Heinz, Shuaimin Liu, Philip Kim, and James Hone, *Radio frequency electrical transduction of graphene mechanical resonators*, Applied Physics Letters **97** (2010), no. 24.

- [113] Q. P. Unterreithmeier, E. M. Weig, and J. P. Kotthaus, *Universal transduction scheme for nanomechanical systems based on dielectric forces*, Nature **458** (2009), 1001–1004.
- [114] L. Y. Gorelik, A. Isacsson, M. V. Voinova, B. Kasemo, R. I. Shekhter, and M. Jonson, *Shuttle mechanism for charge transfer in Coulomb blockade nanostructures*, Phys. Rev. Lett. **80** (1998), 4526–4529.
- [115] A. Isacsson, L. Y. Gorelik, M. V. Voinova, B. Kasemo, R. I. Shekhter, and M. Jonson, *Shuttle instability in self-assembled Coulomb blockade nanostructures*, Physica B: Condensed Matter **255** (1998), no. 14, 150–163.
- [116] Tomáš Novotný, Andrea Donarini, and Antti-Pekka Jauho, *Quantum shuttle in phase space*, Phys. Rev. Lett. **90** (2003), 256801.
- [117] Pascal Stadler, Wolfgang Belzig, and Gianluca Rastelli, *Ground-state cooling of a mechanical oscillator by noise-interference in Andreev-reflections*, arXiv:1511.04858 (2015).
- [118] J. Moser, A. Eichler, J. Güttinger, M.I. Dykman, and A. Bachtold, *Nanotube mechanical resonators with quality factors of up to 5 million*, Nature Nanotechnology **9** (2014), 10071011.
- [119] J. Chaste, M. Sledzinska, M. Zdrojek, J. Moser, and A. Bachtold, *High-frequency nanotube mechanical resonators*, Applied Physics Letters **99** (2011), no. 21, 213502.
- [120] Edward A. Laird, Fei Pei, Wei Tang, Gary A. Steele, and Leo P. Kouwenhoven, *A high quality factor carbon nanotube mechanical resonator at 39 GHz*, Nano Letters **12** (2012), no. 1, 193–197, PMID: 22111547.
- [121] L. D. Landau, E. M. Lifshitz, and L. P. Pitaevskii, *Electrodynamics of Continuous Media*, Course of Theoretical Physics, no. 8, Pergamon, 1984.
- [122] J. B. Marion and S. T. Thornton, *Classical Dynamics of Particles & Systems*, Harcourt Brace Jovanovich, 1988.

- [123] L. D. Landau and E. M. Lifshitz, *Mechanics*, Butterworth-Heinemann, Butterworth-Heinemann, Oxford, 1976.
- [124] A. H. Nayfeh and D. T. Mook, *Nonlinear Oscillations*, Physics textbook, Wiley, 1995.
- [125] Encyclopedia of Mathematics, *Krylov-Bogolyubov method of averaging*, http://www.encyclopediaofmath.org/index.php?title=Krylov%E2%80%93Bogolyubov_method_of_averaging&oldid=22677.
- [126] M. I. Dykman, C. M. Maloney, V. N. Smelyanskiy, and M. Silverstein, *Fluctuational phase-flip transitions in parametrically driven oscillators*, Phys. Rev. E **57** (1998), 5202–5212.
- [127] A. Erbe, C. Weiss, W. Zwerger, and R. H. Blick, *Nanomechanical resonator shuttling single electrons at radio frequencies*, Phys. Rev. Lett. **87** (2001), 096106.
- [128] Hongkun Park, Jiwoong Park, Andrew K.L. Lim, Erik H. Anderson, A. Paul Alivisatos, and Paul L. McEuen, *Nanomechanical oscillations in a single-C60 transistor*, Nature **407** (2000), no. 6800, 57–60.
- [129] R. I. Shekhter, Yu. Galperin, L. Y. Gorelik, A. Isacsson, and M. Jonson, *Shuttling of electrons and Cooper pairs*, Journal of Physics: Condensed Matter **15** (2003), no. 12, R441.
- [130] Rudolf Bratschitsch and Alfred Leitenstorfer, *Quantum dots: Artificial atoms for quantum optics*, Nature Materials **5** (2006), no. 11, 855–856.
- [131] M. Ziese, *Extrinsic magnetotransport phenomena in ferromagnetic oxides*, Reports on Progress in Physics **65** (2002), no. 2, 143.
- [132] B. J. LeRoy, S. G. Lemay, J. Kong, and C. Dekker, *Electrical generation and absorption of phonons in carbon nanotubes*, Nature **432** (2004), 371–374.
- [133] H. K. Onnes, *Further experiments with liquid helium D - on the change of the electrical resistance of pure metals at very low temperatures, etc V the disappearance of the resistance of mercury*, Proceedings of the koninklijke akademie van wetenschappen te Amsterdam **14** (1911), 113–115.

- [134] H. K. Onnes, *The persistence of electric currents without electromotive force in superconductors*, Comptes rendus de l'Academie des sciences **159** (1914), 34–38.
- [135] R. Meissner, W. and Ochsenfeld, *Ein neuer Effekt bei Eintritt der Supraleitfähigkeit*, Naturwissenschaften **21** (1933), no. 44, 787–788.
- [136] F. London and H. London, *The electromagnetic equations of the superconductor*, Proceedings of the Royal Society of London A: Mathematical, Physical and Engineering Sciences **149** (1935), no. 866, 71–88.
- [137] V. L. Ginzburg and L. D. Landau, Zh. Eksp. Teor. Fiz. **20** (1950), 1064.
- [138] Emanuel Maxwell, *Isotope effect in the superconductivity of mercury*, Phys. Rev. **78** (1950), 477–477.
- [139] Charles Poole Jr, *Encyclopedic Dictionary of Condensed Matter Physics*, Academic Press, 2004.
- [140] Leon N. Cooper, *Bound electron pairs in a degenerate Fermi gas*, Phys. Rev. **104** (1956), 1189–1190.
- [141] J. Bardeen, L. N. Cooper, and J. R. Schrieffer, *Microscopic theory of superconductivity*, Phys. Rev. **106** (1957), 162–164.
- [142] L. P. Gor'kov, *A new method in the theory of superconductivity 1*, JETP **7** (1958), 41–46.
- [143] L. P. Gor'kov, *Microscopic derivation of the Ginzburg-Landau equations in the theory of superconductivity*, JETP **9** (1959), 1364–1367.
- [144] B.D. Josephson, *Possible new effects in superconductive tunnelling*, Physics Letters **1** (1962), no. 7, 251–253.
- [145] B. D. Josephson, *The discovery of tunnelling supercurrents*, Rev. Mod. Phys. **46** (1974), 251–254.
- [146] L. I. Glazman, F. W. J. Hekking, K. A. Matveev, and R. I. Shekhter, *Charge parity in Josephson tunneling through a superconducting grain*, Physica B: Condensed Matter **203** (1994), no. 3, 316–326.

- [147] Y. Nakamura, Yu.A. Pashkin, and J.S. Tsai, *Coherent control of macroscopic quantum states in a single-Cooper-pair box*, Nature **398** (1999), 786–788.
- [148] D. Vion, A. Aassime, A. Cottet, P. Joyez, H. Pothier, C. Urbina, D. Esteve, and M. H. Devoret, *Manipulating the quantum state of an electrical circuit*, Science **296** (2002), no. 5569, 886–889.
- [149] A. Buzdin, *Direct coupling between magnetism and superconducting current in the Josephson φ_0 junction*, Phys. Rev. Lett. **101** (2008), 107005.
- [150] Jun-Feng Liu and K. S. Chan, *Anomalous Josephson current through a ferromagnetic trilayer junction*, Phys. Rev. B **82** (2010), 184533.
- [151] Huan Zhang, Jun Wang, and Jun-Feng Liu, *Anomalous Josephson effect in noncentrosymmetric superconductors*, Applied Physics Letters **108** (2016), no. 10, 102601.
- [152] Fabrizio Dolcini, Manuel Houzet, and Julia S. Meyer, *Topological Josephson ϕ_0 junctions*, Phys. Rev. B **92** (2015), 035428.
- [153] Yukio Tanaka, Takehito Yokoyama, and Naoto Nagaosa, *Manipulation of the Majorana fermion, andreev reflection, and Josephson current on topological insulators*, Phys. Rev. Lett. **103** (2009), 107002.
- [154] A. Zazunov, R. Egger, T. Jonckheere, and T. Martin, *Anomalous Josephson current through a spin-orbit coupled quantum dot*, Phys. Rev. Lett. **103** (2009), 147004.
- [155] L. Dell’Anna, A. Zazunov, R. Egger, and T. Martin, *Josephson current through a quantum dot with spin-orbit coupling*, Phys. Rev. B **75** (2007), 085305.
- [156] C. Schrade, S. Hoffman, and D. Loss, *Detecting topological superconductivity with φ_0 Josephson junctions*, arXiv:1607.07794 (2016).
- [157] Fabrizio Dolcini and Francesco Giazotto, *Switching the sign of Josephson current through Aharonov-Bohm interferometry*, Phys. Rev. B **75** (2007), 140511.

- [158] Tomohiro Yokoyama, Mikio Eto, and Yuli V. Nazarov, *Anomalous Josephson effect induced by spin-orbit interaction and Zeeman effect in semiconductor nanowires*, Phys. Rev. B **89** (2014), 195407.
- [159] G. Campagnano, P. Lucignano, D. Giuliano, and A. Tagliacozzo, *Spinorbit coupling and anomalous Josephson effect in nanowires*, Journal of Physics: Condensed Matter **27** (2015), no. 20, 205301.
- [160] D. B. Szombati, S. Nadj-Perge, D. Car, S. R. Plissard, E. P. A. M. Bakkers, and L. P. Kouwenhoven, *Josephson ϕ_0 -junction in nanowire quantum dots*, Nat. Phys. **12** (2016), no. 6, 568–572.
- [161] Milton E. Peña-Aza, Alessandro Scorrano, and Leonid Y. Gorelik, *Parametric excitation of dc current in a single-dot shuttle system via spontaneous symmetry breaking*, Phys. Rev. B **88** (2013), 035412.
- [162] L. Y. Gorelik, A. Isacsson, Y. M. Galperin, R. I. Shekhter, and M. Jonson, *Coherent transfer of Cooper pairs by a movable grain*, Nature **411** (2001), no. 6836, 454–457.
- [163] A. Isacsson, L. Y. Gorelik, R. I. Shekhter, Y. M. Galperin, and M. Jonson, *Mechanical Cooper pair transportation as a source of long-distance superconducting phase coherence*, Phys. Rev. Lett. **89** (2002), 277002.